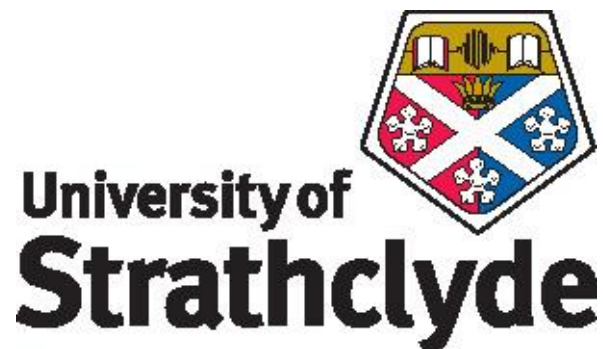


UNIVERSITY OF STRATHCLYDE
Institute of Photonics
Department of Physics

**Diamond processing for advanced photonic
devices**

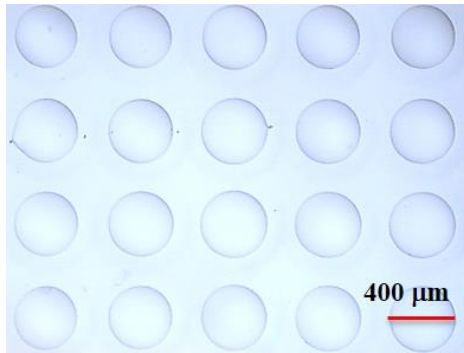
by
Hangyu Liu



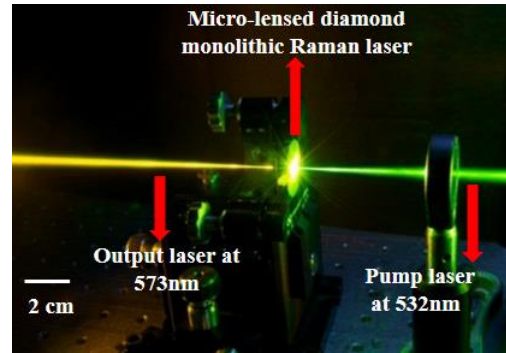
A thesis presented in fulfilment of the requirements for the degree of
Doctor of Philosophy in Physics at the University of Strathclyde in
Glasgow (UK)

2016

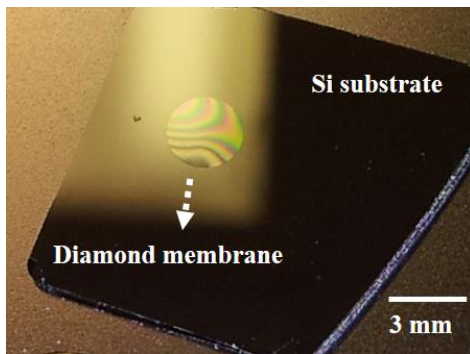
Frontispiece



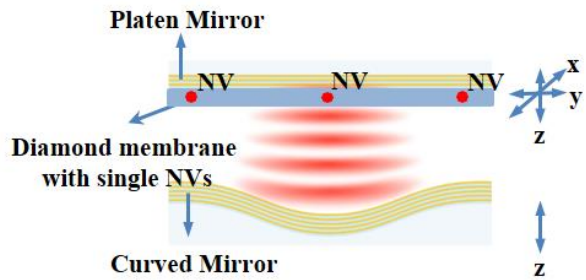
Plan view optical micrograph of an array of high quality single crystal diamond micro-lenses with large radii of curvature.



Compact monolithic diamond Raman laser converting a green laser beam to a yellow laser beam.



Large size high quality ultrathin diamond membrane on a Si substrate.



Schematic of optical cavity-coupled emission from the single NV centres in the diamond membrane.

Copyright Statement

This thesis is the result of the author's original research. It has been composed by the author and has not been previously submitted for examination which has led to the award of a degree.

The copyright of this thesis belongs to the author under the terms of the United Kingdom Copyright Acts as qualified by University of Strathclyde Regulation 3.50. Due acknowledgement must always be made of the use of any material contained in, or derived from, this thesis.

Signed:

Date:

Acknowledgement

I would like to express my great appreciation to my supervisor, Dr. Erdan Gu. Thanks for giving me this opportunity to study at the Institute of Photonics and for supervising and guiding me in the past four years. During my PhD, Erdan offered me invaluable suggestions, inspiration and encouragement using his wisdom, knowledge and patience. He always gave me strong support whenever I needed it. It is under his close supervision that I finally completed this thesis.

I would also like to thank Prof. Martin Dawson, Prof. Alan Kemp, Dr. Michael Strain, Dr. Nicolas Laurand, Dr. Antonio Hurtado, Dr. Ian Watson, Dr. Johannes Herrnsdorf and Dr. Enyuan Xie for their guidance and support through all these years. Special thanks also go to Dr. Johannes Herrnsdorf, Dr. Enyuan Xie, Dr. Benoit Guilhabert, Dr. Ross Leyman, Dr. Sean Reilly and Dr. Vasili Savitski with whom I worked closely. Thanks to Johannes Herrnsdorf, Enyuan Xie and Riccardo Ferreira for providing a lot of great ideas and suggestions to my work. Johannes was always there to help when I was stuck in problems. Thanks to Johannes and Sean for their assistance in acquiring experimental data in my PhD. Many thanks to Jim Sweeney, Lorraine Annand, Sharon Kelly and Lynda McLaughlin for their great support at the Institute. Also thanks to Dr. Pengfei Tian for his help when I first arrived here and for helping to settle down.

I am grateful to all my colleagues in the Institute of Photonics for being with me for the past four years. Thanks for them to bring me joy and help and robust friendships which will last forever.

Thanks to my close friends Shangtong Yang and Bo Xiao for being mentally supportive during my life here at Glasgow. Thanks to those who helped me when I needed it.

Special thanks to my parents, Shaolei Liu and Liqing Yu, for their endless love and the sacrifice that they made for me. A huge thanks to my girlfriend, Xiaxue Wang, who unconditionally supported me during the several critical months of my Thesis and my past two years.

Abstract

Diamond photonic devices are critical components for applications including diamond based optics, diamond Raman lasers and the building blocks of quantum information processing. In this thesis work, to achieve such novel diamond photonic devices, micro-fabrication techniques for diamond have been further developed.

For making diamond optical structures such as diamond micro-lenses, the fabrication involves the definition of photoresist (PR) masks on the surface of diamond by using photolithography and the pattern transfer by using inductively coupled plasma (ICP) etching. A detailed study of the PR thermal reflow process has been carried out to control the shape of PR masks and the resulting diamond structures with spherical or aspheric features after pattern transfer. By combining PR mask shape control with the optimisation of ICP diamond etching, novel micro-lenses on single crystal diamond have been realised. In particular, diamond micro-lenses with radii of curvature larger than 13 mm have been fabricated. Based on these diamond micro-lenses, novel monolithic diamond Raman lasers were achieved.

Furthermore, by using Ar/Cl₂ plasma etching, a large area ultra-thin single crystal diamond membrane with a thickness less than 250 nm has been produced. By coupling the diamond membrane within an open optical Fabry-Perot cavity, the enhanced emission from the nitrogen vacancy (NV) colour centre in diamond was investigated. This approach is attractive for the scalable development of quantum computing based on diamond NV centres.

Abbreviations

AFM	A tomic F orce M icroscope/ M icroscopy
BOE	B uffered O xide E tch
CCD	C harge- C oupled D evice
Cavity-QED	C avity Q uantum E lectro D ynamics
V	V olume
3D	3 D imension
DBR	D istributed B ragg R eflector
DI	D e I onized
FIB	F ocused I on B eam
FWHM	F ull- W idth- H alf- M aximum
HF	H ydro F luoric
LED	L ight E mitting D iode
MEMS	M icro- E lectric- M echanical- S ystem
NEMS	N ano- E lectric- M echanical- S ystem
NMR	N uclear M agnetic R esonance
NV	N itrogen V acancy
PTFE	P oly T etra F luoro E thylene
PL	P hoto L uminescence
PR	P hotoresist
Qubit	Q uantum b it
Q-factor	Q uality f actor
QIP	Q uantum I nformation P rocessing
ICP	I nductively C oupled P lasma
ROC	R adius of C urvature
RIE	R eactive I on E tching
SEM	S canning E lectron M icroscope
SIL	S olid I mmersion L ens
SRS	S timulated R aman S cattering
TIR	T otal I nternal R eflection
ZPL	Z ero P honon L ine

Content

Frontispiece	i	
Copyright Statement	ii	
Acknowledgement	iii	
Abstract	iv	
Abbreviations	v	
Content	vi	
List of Figures	ix	
List of Tables	xvii	
Chapter 1	Introduction	1
1.1	General background	1
1.2	Basic concepts of diamond	2
1.2.1	Diamond crystal structure	2
1.2.2	Diamond types	3
1.2.3	Diamond synthesis	5
1.3	Diamond properties	7
1.3.1	Optical properties	8
1.3.2	NV in diamond	12
1.4	Diamond processing	16
1.4.1	Cutting	16
1.4.2	Polishing	17
1.4.3	FIB milling	17
1.4.4	Dry etching	18
1.5	Diamond photonic devices	19
1.5.1	Diamond optics	19
1.5.2	Diamond Raman laser	22
1.5.3	Cavity-coupled diamond photonics	23
1.6	Outline of this thesis	26
	References	27
Chapter 2	Diamond device fabrication and characterisation	34
2.1	Fabrication of diamond devices	34
2.1.1	Formation and definition of photoresist patterns	35
2.1.2	Pattern transfer	41
2.2	Characterisation methods of diamond photonic devices	47
2.2.1	Profile characterisations	47
2.2.2	Optical characterisations	53

2.3	Conclusion.....	57
	References	58
Chapter 3	The shape evolution and control of photoresist masks by thermal reflow	60
3.1	Introduction	60
3.2	Formation and evolution of an edge bulge during the PR reflow .	62
3.2.1	Edge bulge observation and evolution.....	63
3.2.2	Bulge interaction and minimum thickness for micro-lens formation	66
3.2.3	Discussion on the PR bulge evolution during reflow	70
3.3	Applications of the controllable PR reflow process	71
3.3.1	Hemi-toroid on silicon	71
3.3.2	Micro-lenses with large ROCs.....	73
3.4	Outlook.....	75
3.5	Conclusions	76
	References	76
Chapter 4	Large radius of curvature diamond micro-lenses and monolithic diamond Raman lasers	79
4.1	Introduction	79
4.2	Diamond Raman laser	81
4.2.1	Diamond micro-lenses and micro-resonators	83
4.3	Design of the diamond micro-lenses	85
4.4	Fabrication of diamond micro-lenses with a large ROC.....	86
4.4.1	Fabrication of large ROC PR micro-lens mask	87
4.4.2	Fabrication of large ROC diamond micro-lenses	92
4.5	Results and discussion	93
4.5.1	Diamond micro-lens	93
4.5.2	Micro-lensed monolithic diamond Raman lasers	97
4.6	Conclusion.....	100
	References	100
Chapter 5	Diamond membranes and their applications to quantum information processing	104
5.1	Introduction.....	104
5.1.1	Cavity-coupled NV in diamond membrane	105
5.1.2	Review of diamond membrane fabrications	108
5.2	Fabrication of large size ultrathin diamond membranes	109

5.3	Characterisation of diamond membranes	115
5.3.1	Thickness of the diamond membrane	115
5.3.2	Surface quality of diamond membranes	118
5.4	Applications of diamond membranes in cavity-QED	119
5.4.1	Emission from the NV in free space	120
5.4.2	Cavity-enhanced emission	121
5.5	Conclusion.....	125
	References	126
Chapter 6	Summary and future work	130
6.1	Summary	130
6.2	Future work	131
6.3	Final remark	132
	Reference.....	133
	Appendix I: Table of diamond sample specifications	134
	Appendix II: Publication list	134
	Journal	135
	Conference	135

List of Figures

Figure 1-1: Schematic of a diamond unit cell. The small spheres represent the carbon atoms and the stick line represents the covalent bonds, with a_0 of 0.357 nm being the cubic length [6].	3
Figure 1-2: Diagram of a summary of the different types of diamonds.	5
Figure 1-3: Comparison of the diamond transparency window to other commonly used optical materials (sapphire, ZnSe and germanium) (reproduced from [22]). The transmission % shown represents external transmission.	8
Figure 1-4: Thermal conductivity of diamond compared to other selected materials, data extracted from [29].	10
Figure 1-5: Band structure of diamond [31]. The energy bands are reflected as colour lines and the band gap is represented as spaces in between the lines.	11
Figure 1-6: Diamond refractive index as a function of the wavelength, figure reproduced from [32].	12
Figure 1-7: Schematic of NV (a) crystal structure [37] and (b) electronic structures [38]. In (a), grey balls represent carbon atoms in the diamond lattice, the yellow ball labelled with letter “N” represents nitrogen and the dotted circle labelled with letter “V” represents the adjacent vacancy. In (b) the solid lines represent the energy levels, in which the 3A_2 represents the ground triplet state, 3E represents the excited triplet state, 1A_1 and 1E represent the singlet states, respectively and the $M_{s\pm 1}$ represent the split energy levels of the ground state due to the external microwave field as represented by “MW”. The green solid arrow represents the exciting green laser at 532 nm and the dotted red arrow represents the emission at 637 nm, the dotted grey arrows representing the non-radiative decay [38].	13
Figure 1-8: Emission spectra from NV at cryogenic (T=1.8 K) and room temperature (T=300 K), respectively [39].	14
Figure 1-9: Schematic of an SIL fabricated in a diamond sample, (a) shows the TIR inside a diamond; (b) shows the enhanced extraction efficiency using SIL structure and (c) shows a plot of the comparison between the collection efficiencies with a SIL and without a SIL. Figure sourced from [39].	21

Figure 1-10: Overview of optical micro-cavities with different Q factors and mode volumes (V). After [93].....	23
Figure 2-1: Side view schematic of the fabrication flow for diamond photonic devices.	35
Figure 2-2: Illustration of the photolithography and the different patterns generated using positive and negative photoresists.	36
Figure 2-3: The layer thickness of the coated SPR 220 4.5 and SPR 220 7.0 on wafer substrates corresponding to certain spin speeds, data extracted from Microchem Ltd [7]. 4.5 represents SPR 220 4.5 and 7.0 represents SPR 220 7.0 in the legend, inset is a photo of the spin coater used in this thesis work. The dashed line indicates 3000 rpm.....	37
Figure 2-4: Photo of a Karl Suss MA 6 Mask Aligner used for the work in this thesis.	38
Figure 2-5: Spectrum of the UV light source used for the exposure in this thesis, data extracted from [9].....	39
Figure 2-6: Side view schematic of the dry etching process, the exposed part that will be etched away is labelled with a black dashed-rectangle.	42
Figure 2-7: (a) Photo of the RIE facility and (b) the schematic of the RIE chamber.	42
Figure 2-8: (a) Photograph of the ICP system and (b) the schematic diagram of the ICP chamber indicated by a red rectangle in (a).	43
Figure 2-9: Schematics of the two basic plasma etching mechanisms: (a) physical ion bombardment and (b) chemical etching.	44
Figure 2-10: Photograph of the wet bench in our cleanroom.....	46
Figure 2-11: Photograph of the Dektak 3 surface profilometer used in this thesis....	48
Figure 2-12: A representative PR bulge profile measured by the Dektak 3 surface profilometer. Φ is the measured diameter.	49
Figure 2-13: (a) Photograph of the optical profiler and (b) the schematic diagram of this optical profiler [21]. The optical filter removes all but the red light from the white light of the halogen lamp.	50
Figure 2-14: Typical measurement result from the Optical Profiler using VSI mode demonstrating a 3D reconstructed topography of a diamond sample sitting on a Si substrate. The measurement is carried out on an ICP etched	

diamond platelet from Element Six with a thickness around 6 μm . The measured area is $640 \times 480 \mu\text{m}^2$	51
Figure 2-15: Photos of the AFM system used in this thesis work.	52
Figure 2-16: Schematic of the principle of the AFM measurement.....	52
Figure 2-17: (a) Schematic of the knife-edge technique used for the focal length measurement and (b) the converged propagation beam profile and (c) the Gaussian profile demonstrating the beam diameter D (green) and the clip width D_c (blue) at each Z position, the beam diameter being indicated with green arrow [24].	54
Figure 2-18: (a) Photograph of the home-build scanning confocal microscope setup used in this work and (b) the schematic diagram of the low-temperature cryostat. Image courtesy: Photonic Nanomaterials Group, University of Oxford.	56
Figure 2-19: Schematic of the scanning confocal microscope experimental setup. Image courtesy: Photonic Nanomaterials Group, University of Oxford.	57
Figure 3-1: Micrographs of PR patterns ($h_0 = 15 \mu\text{m}$) taken at different temperatures during reflow. a) Sample before reflow, $T = 70 \text{ }^\circ\text{C}$, which is below the PR glass transition temperature. (b)-(h) Evolution of the PR pattern while the temperature was gradually raised to $240 \text{ }^\circ\text{C}$	64
Figure 3-2: Derived profiles from the surface profiler measurements of the edge bulges during reflow in where the black curve represents a profile with an edge bulge and illustrates the key parameters d_{max} and D , and the red curve represents the profile of an eventually evolved convex lens, the arrows indicate the bulge propagation direction.	64
Figure 3-3: Schematic of the PR bulge evolution during reflow.	65
Figure 3-4: d_{max} as a function of $T - T_g$ with h_0 of 6.3, 11.6, 15 and 21 μm , respectively.	66
Figure 3-5: Propagation distance d_{max} as a function of the initial thickness h_0 of PR patterns with different diameters. The thick red dashed-dotted line represents Equation (3-1), and the vertical dashed-dotted lines indicate the minimum h_0 at each diameter. Inset: micrograph of PR patterns with an initial thickness of 9.15 μm before thermal reflow.	67

Figure 3-6: Minimum PR thickness needed to form a spherical lens shape with a given radius at a reflow temperature of 125 °C on silicon.....	68
Figure 3-7: (a) Normalised deviation from a spherical lens shape calculated by Equation (3-2) and (b) example traces of measurement and fit of data points (1) and (2) of D= 400 μm shown in (a), Trace (1) h ₀ =9.15 μm, Res= 0.054 and Trace (2) h ₀ =16.9 μm, Res=0.0015.	69
Figure 3-8: Schematic of the process steps for hemi-toroid fabrication on silicon. ..	71
Figure 3-9: Plan view optical image of the fabricated silicon hemi-toroids with D from 200 to 400 μm.	72
Figure 3-10: Measured profiles of a typical PR and silicon hemi-toroid with a diameter of 350 μm.	72
Figure 3-11: Measured and fit of the data of PR bulge propagation on the surface of diamond in which d _{max} is a function of T-T _g with h ₀ of 7.2 μm, 16.3 μm and 20.5 μm, respectively.	74
Figure 3-12: Comparison of profiles of formed PR patterns on diamond: (a) the profile with edge bulges formed using single PR layer and (b) the micro-lens formed by control the PR thickness at 11.5 μm and a reflow temperature over 135 °C (ROC=1.4 mm) using multiple PR layers.	75
Figure 4-1: Mechanism of Raman scattering in a diamond Raman laser, (a wavelength shift from 532 nm to 573 nm is used here for illustration).	81
Figure 4-2: (a) A conventional picosecond pulsed diamond Raman laser and (b) a schematic of this laser [24].....	82
Figure 4-3: (a) Demonstration of a monolithic diamond Raman laser based on the micro-lensed resonator using a pulsed 532 nm laser of 1.5 ns duration at a pump pulse energy of 1.5 μJ and (b) Schematic of the monolithic diamond Raman laser.	82
Figure 4-4: Schematic of the resonator based on a diamond micro-lens illustrating the key parameters of: beam radius on the planar surface w , mode area πw^2 , resonator length L , lens diameter Φ and lens height h . Specifications of mirror coatings are: HT 532 nm, high transmission at 532 nm; HR 532/573 nm, high reflectivity at 532/573 nm; 30% OC 573 nm, 30% output coupling at 573 nm.....	85

Figure 4-5: Schematic of the fabrication process of diamond micro-lenses.....	87
Figure 4-6: Schematic of the "edge bead effect": (a) PR bead formed at edge of the diamond sample after spin coating due to surface tension; (b) and (c) demonstrate the "edge bead effect" during lithography by comparing spin coated PR without and with "edge bead effect".....	88
Figure 4-7: Schematic of the fabrication process of the optical adhesive holder.	88
Figure 4-8: A plan view micrograph under the microscope demonstrating a uniform PR coating at the interface of the diamond and the holder.	89
Figure 4-9: Measured profiles of the spin coated PR on surface of two diamond samples with and without a holder, demonstrating the effective removal of the edge bead. Inset is a plan view photograph of the surfaces of the PR spin coated diamond samples.....	90
Figure 4-10: Achieved PR micro-lens array on the diamond surface with a high uniformity and pattern fidelity (stitched from multiple plan view images taken under the microscope with the same magnification).	91
Figure 4-11: Plan view images of etched PR micro-lenses on diamond with different etching methods and etching durations: (a) long time plasma etching after 25 mins and (b)-(f) five-step etching with 5 mins duration of each step, the scales of each image are the same as shown in (a) and the inset.	92
Figure 4-12: Optical images of fabricated diamond micro-lenses with large ROCs.	94
Figure 4-13: (a) Measured and fitted profiles of a column of fabricated diamond micro-lenses as shown in Figure 4-12 along the black dotted arrow and (b) focal length measurement of a representative diamond micro-lens fabricated with a height of 1.7 μm or less, distance being measured in reference to the place where diamond is located.	94
Figure 4-14: Characterisation of surface roughness of fabricated diamond micro-lenses: (a) image of the diamond micro-lens with AFM measured areas indicated by red, blue and green dashed squares, respectively; (b) measured RMS roughness at the top of the micro-lens, corresponding to the red-dashed square labelled area in (a); (c) measured RMS roughness at the bottom of the micro-lens, corresponding to the blue-dashed square labelled area in (a) and (d) measured RMS roughness at the gap between	

micro-lenses, corresponding to the green-dashed square labelled area in (a).	95
Figure 4-15: (a) RMS roughness of Ar/Cl ₂ plasma etched diamond surface as a function of etch durations and corresponding measured surfaces taken at (b) surface of the as-received diamond sample and (c) surface after plasma etching for 10 mins.....	96
Figure 4-16: Demonstration of the monolithic diamond Raman laser based on the micro-lens resonator using a pulsed laser of 1.5 ns duration at a pump pulse energy of 1.5 μJ.....	97
Figure 4-17: Typical generated Raman shift spectrum with 1 st and 2 nd Stokes wavelengths being presented.....	98
Figure 4-18: (a) Energy transfer characteristics for the 1st (green squares), 2nd (blue triangles), and 3rd Stokes orders (red circles) and the combined Raman output (inverted black triangles) of the micro-lensed monolithic diamond Raman laser and (b) the conversion efficiency from pump to combined Raman.....	98
Figure 4-19: 1 st Stokes pulses at 573nm (a) below threshold of 2 nd Stokes and (b) at maximum pump power with both 2 nd and 3 rd Stokes oscillating.	99
Figure 5-1: Schematic of cavity-quantum electrodynamics [25].....	106
Figure 5-2: (a) Schematic of the open-optical mirror cavity with coupled NV centres in the diamond membrane and (b) an SEM of the curved mirror cavity fabricated using focused ion beam (FIB) milling. Images courtesy: Photonic Nanomaterials Group, University of Oxford [30].....	108
Figure 5-3: Schematic of the fabrication flow for the diamond membrane.....	110
Figure 5-4: Thickness of the diamond platelet (a) before thinning and (b) after thinning. The insets are the corresponding optical images of the diamond sample taken under a microscope, the arrows indicated the scan-routines of the Dektak profiler.	112
Figure 5-5: (a) Schematic of the floated diamond membrane on a Si wafer using DI water and (b) a picture of the floated diamond membrane on a Si wafer.	113

Figure 5-6: Diamond membrane transfer process: (a) a picture demonstrating “pick-up” of the diamond sample using the corner of a cleanroom wipe and (b) a picture of the diamond membrane placed on a solvent-cleaned Si substrate. 114

Figure 5-7: Images of the fabricated diamond membrane: (a) A photograph of the fabricated natural diamond membrane. This diamond membrane was capillary bonded to a DBR mirror; (b) Optical image of the natural diamond membrane under a microscope, colour fringes can be observed at the top left corner which indicates the thickness variation there. 115

Figure 5-8: SEM images of the achieved thinned natural diamond membrane on a DBR mirror, where the images were taken at a tilted angle of 45°. (a) SEM image of the natural diamond membrane on DBR mirror demonstrating the uniformity of the achieved diamond membrane and (b) SEM image of the left corner indicated by the red dotted square in (a), demonstrating the well-bonded interface between the diamond membrane and the DBR mirror..... 116

Figure 5-9: AFM measurement results: (a) top view of a measured area of 20×20 μm² at the same corner indicated by the red-dotted-square shown in Figure 5-8 (a); (b) 3D perspective image of the measured corner of the diamond membrane. Thicknesses of the edges indicated by the green and red line shown in (a) were labelled with white letters, demonstrating thicknesses of the membrane ΔY₁ is 294.4 nm and ΔY₂ is 257.8 nm, respectively. 116

Figure 5-10: 3D image of the measured thickness variation using the optical profiler. The coloured bar indicates the corresponding thickness reflected in the 3D image, the measured area is 640×480 μm²..... 117

Figure 5-11: AFM measured RMS surface roughness results of: (a) As-received diamond surface, R_q is 0.83 nm (3×3 μm²); (b) Etched membrane surface, R_q is 0.25 nm (3×3 μm²)..... 118

Figure 5-12: Schematics of the experimental setup of the open optical cavity-coupled diamond membrane: (a) schematic of the sample stage, (b) schematic of the independently tunable mirrors and (c) schematic of the piezo actuators. 119

Figure 5-13: PL images at the membrane edge: (a) PL image of the overall scan at an area of $140 \times 140 \mu\text{m}^2$, some fringes can be observed at the edge which represent uneven thicknesses due to the wedge; (b) Zoom-in of the PL image which presents a bright single feature as labelled with Feature 1. 120

Figure 5-14: (a) Emission spectrum from Feature 1 under 1mW excitation power, a sharp line at 573 nm represents the 1st Raman peak. (b) Measured result of the power saturation of Feature 1 and the fit, signal refers to the count from the NV, noise refers to the count from the background noise and P_{sat} fit refers to the saturation fit of the power used at 1.8 mW, 0.396 mW/cm^2 using the method as reported in [54]. 121

Figure 5-15: (a) Side-view schematic of the cavity-coupled diamond membrane at the edge and (b) an image of the open optical cavity-coupled diamond membrane under a microscope. 122

Figure 5-16: Spectrum of cavity-enhanced emission from the diamond membrane, cavity length $2.11 \mu\text{m}$ 123

Figure 5-17: (a) Side-view schematic of cavity-coupled diamond membrane and (b) an image of the open optical cavity-coupled diamond membrane under a microscope. 124

Figure 5-18: Spectrum of cavity-enhanced emission from the diamond membrane, cavity length $3.39 \mu\text{m}$ 124

List of Tables

Table 1-1: Comparison of competitive materials for use as Raman laser material, data extracted from [2].	9
Table 1-2: Values of the Raman gain in diamond at different pump wavelengths [28].	10
Table 2-1: Wavelengths of light sources for optical lithography and the corresponding resolution R and DOF. $k_1=0.3$ and $k_3=1$ for R and DOF calculations. Assuming $NA=0.9$ for all wavelengths except extreme ultraviolet (EUV), for which $NA=0.25$ [11].	40
Table 2-2: Ar/Cl ₂ ICP etching recipe for diamond photonic device fabrication.	45
Table 2-3: Ar/O ₂ ICP etching recipe for diamond photonic device fabrication.	45
Table 2-4: Comparison of the profile measurement tools.	52

Chapter 1 Introduction

This chapter first gives a general background of this thesis work on diamond photonic devices. Then, Section 1.2 introduces some basic concepts about diamonds that will be used in this thesis work. These basic concepts include the diamond crystal structure, types and synthesis. Section 1.3 gives a general introduction to the properties of diamond and Section 1.4 gives a review of diamond processing methods. Section 1.5 gives a brief overview of recent research on diamond photonic devices. Section 1.6 introduces the outline of this thesis.

1.1 General background

Photonic devices, which are components for creating, manipulating or detecting light [1], require the identification and adoption of suitable materials with outstanding characteristics. Of such materials, diamond, especially single crystal diamond, is a particularly good example, as highlighted by its attractive properties such as a wide transparency spectral window, a high Raman gain coefficient, a high thermal conductivity and colour centres with excellent quantum properties such as the nitrogen vacancy [2].

By applying the extraordinary properties of diamond, novel diamond photonic devices have been developed in recent years including diamond based optics, diamond Raman lasers, diamond-based single photon sources and the building blocks of quantum information processing (QIP) [2, 3]. In these devices, the light propagation behaviour and light-matter interaction are modified by diamond micro/nano-structures such as micro-lenses, micro-cavities and cavity-coupled membranes.

In this thesis, we describe the design and development of novel diamond micro/nano-structures to achieve photonic components with special functions. Over the course of these studies, diamond micro/nano-fabrication techniques have been developed for controllable fabrication of novel diamond microstructures and devices such as micro-toroids and micro-cavities. In particular, diamond micro-lenses with a state-of-the-art large radius of curvature (ROC) of more than 13 μm and ultra-thin diamond membranes with a thickness less than 250 nm have been realised.

The diamond micro/nano-structures developed in this work here enabled high-performance novel diamond photonic devices including micro-lensed monolithic diamond Raman lasers and cavity enhanced diamond defect emissions. The functionalities of these diamond photonic devices are described and fully characterised. These research results are leading to the advance of high-efficiency compact light sources and to scalable QIP, as will be discussed.

With the applications of diamond photonic devices in mind, a basic understanding of diamond, such as its structure and type, properties and the methods for diamond synthesis and processing, is crucial for designing and achieving the novel diamond photonic devices. These factors are therefore described below.

1.2 Basic characteristics of diamond

In this section, the diamond crystal structure, the different types of diamond and the synthesis of diamond are introduced.

1.2.1 Diamond crystal structure

Diamond consists of two interpenetrating face-centred cubic (fcc) lattices of carbon atoms, displaced by one-quarter along the cube diagonal. The diamond unit cell contains eight atoms. Within the diamond crystal, each carbon atom is symmetrically bonded to four neighbouring carbon atoms. These carbon atoms are situated at the corners of a surrounding tetrahedron and are connected via covalent sp^3 bonds. In sp^3 hybridisation, one 's' and three 'p' orbitals of almost equal energy intermix to give four identical and degenerate hybrid orbitals, oriented in tetrahedral symmetry with $109^\circ 28'$ angle between them. A unit cell of the diamond crystal structure is shown in Figure 1-1. In this Figure, small spheres represent the carbon atoms at the corners, the face centre and four sides of the tetrahedroid inside. The stick lines joining them represent the covalent bonds [4] with a cubic length, a_0 , of 0.357 nm at room temperature [5]. The bonds between the carbon atoms (bond energy of 1087 kJ/mol) are, for example, much stronger than those in silicon (bond energy of 787 kJ/mol) and germanium (bond energy of 762 kJ/mol). It is this strong bonding that makes diamond mechanically hard and chemically stable [6].

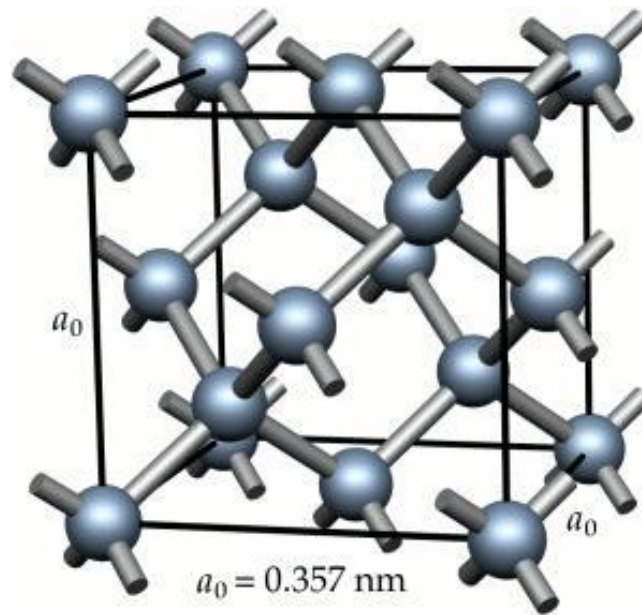


Figure 1-1: Schematic of a diamond unit cell. The small spheres represent the carbon atoms and the stick line represents the covalent bonds, with a_0 of 0.357 nm being the cubic length [6].

1.2.2 Diamond types

According to the level and kind of the chemical impurities, diamonds are scientifically classified into four types: Type Ia, Type Ib, Type IIa, and Type IIb [7]. The level of the impurities is measured at the atomic level within the crystal lattice of carbon atoms [8].

Type I diamonds, which includes Type Ia and Ib diamonds, contain nitrogen impurities with concentrations from 20 up to 3000 ppm (parts-per-million) as their main impurities. Type I diamonds absorb light in both the UV and infrared regions. They also have a characteristic fluorescence and visible absorption spectrum [9]. Natural diamonds are often mixes of Type Ia and Ib, which can be determined by their infrared absorption spectrum [10].

Type Ia diamonds contribute to about 98% of all natural diamonds. The nitrogen impurities, up to 0.3% (3000 ppm), are clustered within the carbon lattice and are relatively widespread. The absorption spectrum of the nitrogen clusters in diamond results in the absorption of the blue light, making the diamond appear almost colourless or pale yellow. Most Ia diamonds are a mixture of Type IaA and Type IaB material. Type IaA, where the nitrogen atoms are in pairs, normally appear to be colourless.

Type IaB, where the nitrogen atoms are in large even-numbered aggregates, appear to be yellow or have a brown tint.

Type Ib diamonds contribute to about 0.1% of all natural diamonds. The nitrogen impurity level here is up to 0.05% (500 ppm) but the impurities are more diffused in this type of diamond. Type Ib diamonds absorb green light in addition to blue and have an intense yellow or occasionally brown tint. The visible absorption spectrum of this type of diamond is broad-featured without sharp absorption bands [11]. Almost all high-pressure-high-temperature (HPHT) synthetic diamonds, the synthesis of which is described below, are of Type Ib [12].

Type II diamonds, which includes Type IIa and Type IIb diamonds, have no measurable nitrogen impurities. Unlike Type I diamonds, type II diamonds absorb in a different region of the infrared and transmit in the UV below 225 nm. They also have different fluorescence characteristics, but no discernible visible absorption spectrum. The shapes of these crystals are found to be large and irregular. Type II diamonds were formed under extremely high pressure for long time periods.

Type IIa diamonds contribute to 1-2% of all natural diamonds (1.8% of gem diamonds). These diamonds, being almost or entirely devoid of impurities, are usually colourless. Occasionally, while Type IIa diamonds are being extruded towards the surface of the Earth, the pressure and tension can cause structural anomalies arising through plastic deformation during the growth of the crystal structure. These structural anomalies lead to imperfections in the diamonds that may confer a yellow, brown, orange, pink, red, or purple colour to the gem. Type IIa diamonds can have their structural deformations "repaired" via an HPHT process, removing much or all of the diamond's colour [13]. Synthetic diamonds grown using the chemical vapour deposition (CVD) process (see below) typically belong to this type.

Type IIb diamonds contribute to only about 0.1% of all natural diamonds, making them one of the rarest natural diamonds and very valuable [14]. In addition to having very low levels of nitrogen impurities comparable to Type IIa diamonds, Type IIb diamonds contain significant boron impurities. The absorption from boron causes these gems appear to be light blue or grey [15]. These diamonds are also p-type semiconductors due to uncompensated holes (holes being electron vacancies in the valence band that functioned as positive charge carriers) and as little as 1 ppm of boron

in diamond is enough to produce an electronic effect. Type IIb diamonds show a distinctive infrared absorption spectrum and show gradually increasing absorption towards red region of the visible spectrum. Figure 1-2 summarises the types of diamonds discussed in this section.

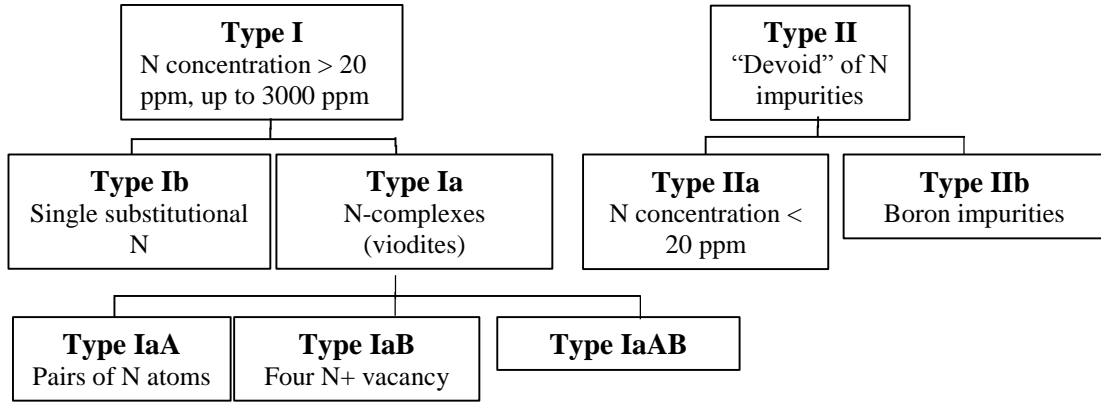


Figure 1-2: Diagram of a summary of the different types of diamonds.

1.2.3 Synthesis of diamond

Driven by the desire to make cheaper and more readily available diamonds, researchers started to develop techniques to create artificial diamonds. Such research, named diamond synthesis, has been well developed since around 1955 [16-18]. Using the HPHT and CVD methods, synthetic diamonds have now become widely available with a cheaper price and higher quality [19]. Due to this reason, the research based on diamond has been accelerated and many outcomes have been fulfilled. Diamond is thus truly becoming “a scientist’s best friend” [20].

Currently, three main processes are widely used for the diamond synthesis, namely HPHT, CVD and detonation. Each method is described in detail as follows.

High pressure high temperature (HPHT)

Synthesis of an artificial diamond via the HPHT process was historically the first to be developed [17]. The method mimics the formation of a natural diamond via the geological processes. This technique involves subjecting a carbon-containing material, i.e. graphite, to a high temperature (>1500°C) and high pressure (> 5 Gpa), which induces the phase transition of graphite to diamond.

The required high-pressure and high-temperature are achieved by using different press systems, including belt systems [17], cubic systems [21] and bar systems [22]. All HPHT press technologies employ a core reaction cell. This cell mainly contains a

carbon source and some seed crystals to facilitate the growth of diamonds. A metal flux, typically iron (Fe), nickel (Ni), or a mixture of the two, is used as a solvent to transport the carbon source (graphite) to the seeds during the process. The use of a flux, which allows diamond to be synthesised at much lower temperatures and pressures, is necessary for a direct conversion of graphite into diamond.

The main advantages of the HPHT method for growing diamonds are its relatively low cost and high throughput. Thus, the HPHT process is suitable for industrial production.

Chemical vapour deposition (CVD)

An alternative method of diamond synthesis is CVD. In this process, the diamond, sourced from a hydrocarbon gas mixture, is grown on a substrate inside a chamber. The growth temperature and pressure can be fully controlled in the chamber.

The basic principle of CVD diamond growth is as follows: a substrate, typically single-crystal diamond, silicon, quartz, sapphire, or some particular type of metal (i.e. iridium [2]), is chosen and placed inside a growth chamber. During the growth, a mixture of hydrocarbon gas, typically methane and hydrogen, is injected into the chamber. This mixture source is heated using either a microwave beam, a hot filament, an arc discharge, a welding torch, a laser or an electron beam. At temperatures above 800 °C, the mixture is ionized into chemically active radicals. These active radicals form the plasma which then reacts and begins to form diamond crystals on the substrate.

Depending on the choice of growth substrate, single crystal diamond or polycrystalline diamond can be grown. Single crystal diamonds, which consist of a single, continuous crystal, are grown on single crystal diamond substrates. Polycrystalline diamonds, which consist of numerous small grains in intimate contact, are grown on extrinsic substrates other than single crystal diamonds. For polycrystalline diamonds, small diamond crystals nucleate randomly but, as the growth proceeds, the crystals become larger and eventually coalesce to form a continuous polycrystalline film.

CVD-grown single crystal diamond generally has better optical performance compared to polycrystalline diamond due to the higher quality and lower optical scattering of the diamond. The advantages of CVD diamond growth include the ability

to grow diamond over large areas and on various substrates, and the fine control over the chemical impurities and thus properties of the diamond produced [23, 24]. Some of the diamonds used in this thesis work are CVD grown single crystal diamonds supplied by Element Six Ltd. [25].

Detonation

Diamond nanocrystals, typically a few nanometres in size, have been shown to originate from the detonation of carbon-containing explosives e.g. trinitrotoluene (TNT) and cyclotrimethylenetrinitramine (RDX or T4) in a metal chamber and are commonly referred to as detonation nanodiamonds (DNDs).

The correct conditions of high-pressure ($\sim 20\text{-}30$ GPa) and high-temperature ($\sim 3000\text{-}4000$ K) for the thermodynamic stability of diamond are achieved at the shock front of the explosion. Under such conditions, the carbon atoms contained in the explosives themselves assemble to form diamonds. The chamber must be rapidly cooled after the detonation during the process. This is to suppress the tendency of forming graphite from carbon.

Detonation nanodiamonds are consequently very small (i.e. 5 nm) and tend to have an extremely narrow distribution in size. This is because the time during which the pressure and temperature are suitable for carbon atoms to form diamond is limited (fractions of microseconds). Generally, commercial detonation nanodiamond powders contain up to 98% diamond crystals in the range of 2 to 10 nm.

The synthesis of artificial diamonds by detonation has taken a decisive upturn during the past few years [2]. Notably, although the greatly reduced size of detonation diamonds means that they are less attractive than HPHT or CVD diamonds for industrial purposes, they are regarded as highly promising for a variety of applications in the emerging field of nanotechnology [3].

1.3 Diamond properties

Diamond has a number of very attractive material properties making it promising for high-performance photonic devices. These properties include a wide transparency window, a large Raman gain coefficient, a high thermal conductivity, and extreme mechanical hardness and chemical inertness. Additionally, nitrogen vacancy (NV)

centres in the diamond are of interest for applications in quantum photonics [3]. This section will introduce the above-mentioned properties of the diamond.

1.3.1 Optical properties

Transparency

With a wide indirect bandgap of 5.47 eV, diamond transmits almost all wavelengths from 225 nm in the deep UV to the far infrared [2] as shown in Figure 1-3. For the far infrared, the 3 to 6 μm region shows absorption due to the higher-order multi-phonon processes [9].

The broad transparency of diamond highlights its capabilities as an optical window material [26]. This broad transparency of diamond also benefits Raman laser application and single photon emissions with different wavelengths for use in quantum technology. In Figure 1-3 (reproduced from [22]), the diamond transparency window is compared to other commonly used optical materials, namely sapphire, zinc selenide (ZnSe) and germanium. As shown in Figure 1-3, diamond has the broadest transparency window of these materials.

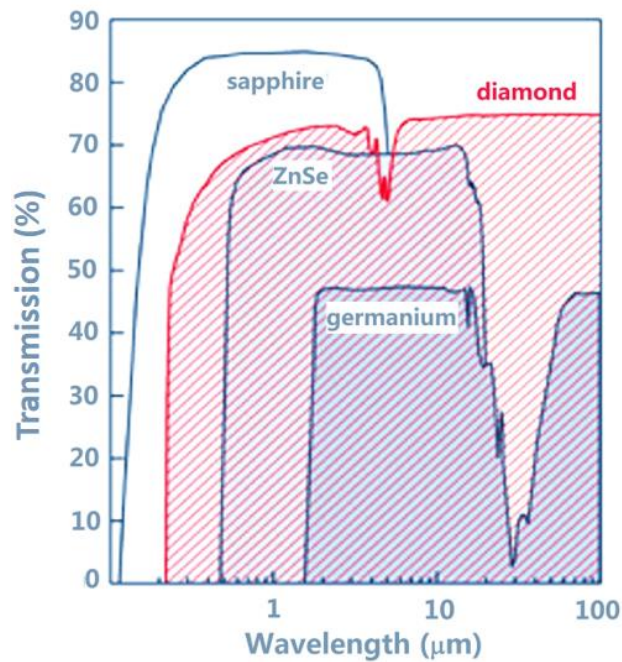


Figure 1-3: Comparison of the single crystal diamond transparency window to other commonly used optical materials (sapphire, ZnSe and germanium) (reproduced from [22]). The transmission % shown represents external transmission.

Raman gain coefficient

A Raman laser uses frequency conversion in an optical gain medium to extend the laser's wavelength of operation. The frequency conversion occurs via stimulated Raman scattering (SRS) and a Raman gain coefficient is associated with the optical gain arising from SRS [27] (see more discussions on page 81). The Raman gain coefficient of diamond is the highest among the most useful solid-state Raman materials; being 4 times that of potassium gadolinium tungstate (KGW), 3 times that of yttrium orthovanadate (YVO₄) and 2 times that of barium nitrate (Ba(NO₃)₂) [2]. The high Raman gain coefficient in diamond is an advantage for Raman laser design. It provides lower thresholds, relaxed constraints on the performance of optical coating and a greater freedom to use shorter crystal lengths. This combined with diamond's high thermal conductivity and wide transparency highlights diamond to be an ideal material for developing compact monolithic diamond Raman lasers (as will be presented in Chapter 4).

The Raman gain coefficient and the available crystal length of diamond, KGW, YVO₄ and Ba(NO₃)₂ are listed in Table 1-1.

Table 1-1: Comparison of competitive materials for use as Raman laser material, data extracted from [2].

Material	Diamond	KGW	YVO ₄	Ba(NO ₃) ₂
g (cm/GW), at 1064 nm and room temperature	~17	~4	~5	~11
Crystal length L (mm)	6	25	25	25

* g =Raman gain coefficient and L =typical crystal length needed for the Raman laser.

The Raman gain coefficient in diamond is directly relevant to the study of SRS in solid-state media in general and to Raman laser engineering in particular. The variation of this quantity with wavelength will determine the spectral range within which diamond Raman lasers will operate efficiently. A systematic study of the dependence of the steady-state Raman gain coefficient in single-crystal CVD diamond on pump wavelength is carried out by Vasili et al. [28]. The measured wavelength

dependence Raman gain coefficient of diamond is summarised in Table 1-2. The measurements indicate that the gain coefficient increases from 7.6 ± 0.8 cm/GW at 1280 nm to 78 ± 8 cm/GW at 355 nm with a $1/\lambda$ dependence. The measurements were taken with the pump polarisation along the $\langle 111 \rangle$ direction in the diamond. These measurements, will assist with the design of future diamond Raman lasers.

Table 1-2: Values of the Raman gain in diamond at different pump wavelengths, data from [28].

Pump wavelength, nm	Raman gain, cm/GW
355	78 ± 8
532	42 ± 4
670	41 ± 4
800	26 ± 3
1064	17 ± 2
1280	7.6 ± 0.8

Thermal conductivity

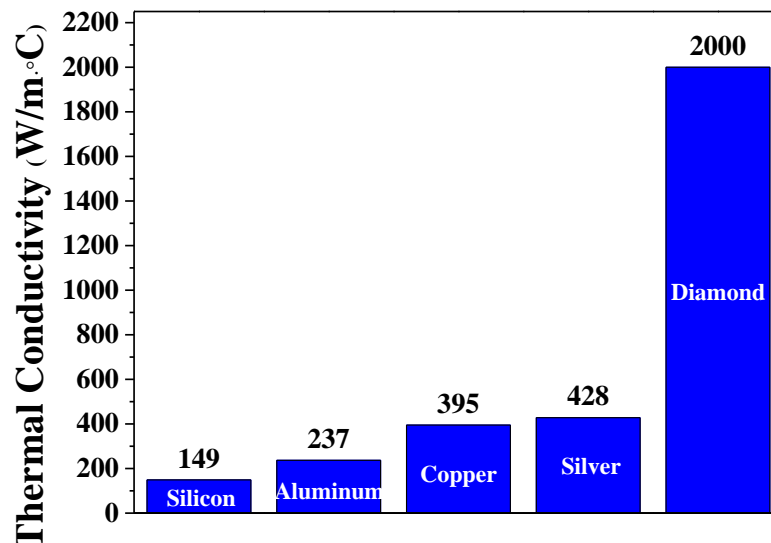


Figure 1-4: Thermal conductivity of diamond compared to other selected materials, data extracted from [29].

Thermal conductivity (often denoted as k) characterises the property of a material to conduct heat. Diamond is a very good conductor of heat because of the strong covalent bonding and low phonon scattering [30]. The thermal conductivity coefficient

of diamond is as large as 2000 (W/m²·°C), almost five times larger than that of silver and copper, ten times larger than that of aluminium, and more than thirteen times larger than that of silicon, as shown in Figure 1-4.

The effective management of heat is often the biggest hurdle to increasing the output power and efficiency of semiconductor devices such as light-emitting diodes (LEDs) and laser diodes. Here, detrimental effects such as increased nonradiative recombination, reduced peak optical gain, beam distortions, and crystal strain or cracking, are typically temperature-dependant. Since diamond has such a high thermal conductivity, it is widely used in semiconductor devices as a heat spreader or heatsink to minimise these and other heating effects [2,9, 14].

Band structure

Band structure of a solid describes the range of energies that an electron within the solid may have (called energy bands) and ranges of energy that it may not have (called band gaps). Diamond has similar band structures of other semiconductor materials such as silicon. However, the band gap of diamond (5.47 eV) is much larger than silicon (1.09 eV) [2]. Figure 1-5 shows the band structure of diamond where the energy bands are reflected as colour lines and the band gap is represented as spaces in between the lines. Γ is the centre point of the first Brillouin zone for the face centred cubic lattice, which possesses the highest symmetry. U,K, L, and X represent the points in the zone; Λ , Δ , and Σ represent the lines of high symmetry.

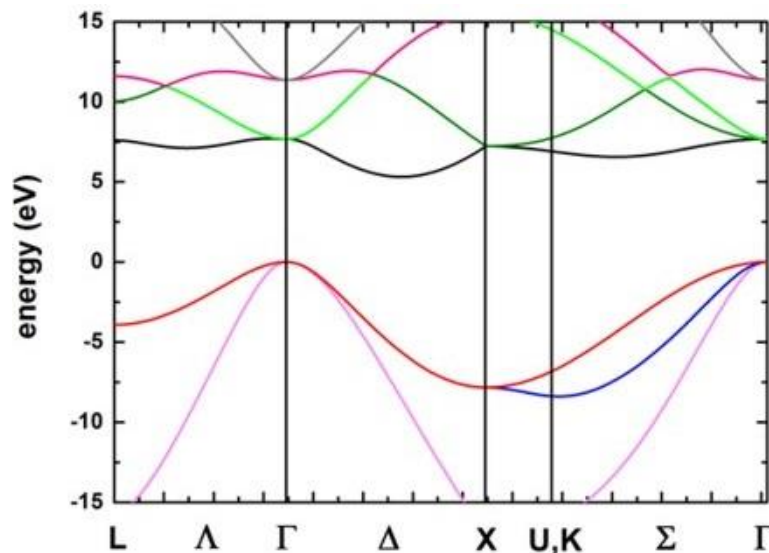


Figure 1-5: Band structure of diamond [31]. The energy bands are reflected as colour lines and the band gap is represented as spaces in between the lines.

Refractive index

The light refracts at the interface of materials that have different refractive indices. The propagating of the refracted beam follows the Snell's law:

$$n_1 \sin \theta_1 = n_2 \sin \theta_2 \quad (1-1)$$

where n_1 refers to the refractive index of the upper medium and n_2 refers to the refractive index of the lower medium, and θ_1 and θ_2 are the reflected angle at the interface of two media, respectively. Diamond has an average refractive index of ~ 2.4 at the visible spectrum region. The refractive indices of diamond change with wavelengths. Figure 1-6 shows the diamond refractive index as a function of the wavelength. The index value can be used as a reference in design of the optical components such as diamond waveguides and diamond resonators [49,97].

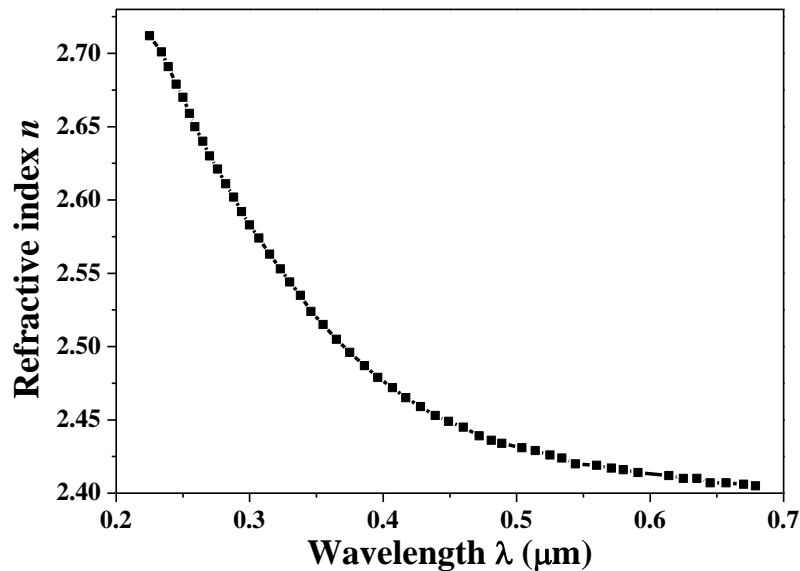


Figure 1-6: Diamond refractive index as a function of the wavelength, figure reproduced from [32].

1.3.2 NV centres in diamond

The NV centre in diamond is attracting much attention as a promising candidate to provide solid-state quantum bits (qubits) for QIP [33]. QIP is the engineering technique used to manipulate information that is held in the state of a quantum system [3]. There are more than 500 different defects already discovered in diamond, among which the NV is the most studied [34]. The NV centre is a defect that consists of a substitutional nitrogen atom and an adjacent vacancy within the carbon lattice as depicted in Figure 1-7 (a). These NV centres, especially the negatively charged NV

centres (for which an extra electron is located at the vacancy site forming a spin $S=1$ pair with one of the vacancy electrons), have a spontaneous emission under optical excitation that generates photons with a wavelength of 637 nm, as shown in Figure 1-7 (b). The NV centre refers to the negatively charged NV in this thesis hereafter. The purely electronic transition generated by the NV centre is named the zero phonon line (ZPL). This ZPL emission exhibits a narrow linewidth. Having a ZPL emission at 637 nm and a lifetime of approximately 12 ns, the NV centre is found to be a promising photo-stable single photon emitter at room temperature. Having energies of the bound electronic states smaller than the 5.47 eV bandgap of diamond, these NV centres can be considered as “trapped atoms” in the diamond lattice. The diamond lattice can provide protection of the NV centre against the decohering influence of the solid-state environment. Due to this protection, the coherence time of NV centres can be longer than 1.8 ms even at room temperature, which is necessary for QIP [34].

The NV centre presents unique possibilities for QIP even at room temperature. Firstly, the NV centre can be optically initialised to quantum spin states [35]. Secondly, the quantum state of this centre can be manipulated in the ground states of $m_s=\pm 1$ as shown in Figure 1-7 (b) via electric, magnetic and elastic fields and microwave pulses [33]. Furthermore, the spin states of these NV centres can be subsequently read out through the photons emitted from these NV centres at the ZPL and inter-connected to form quantum networks [36].

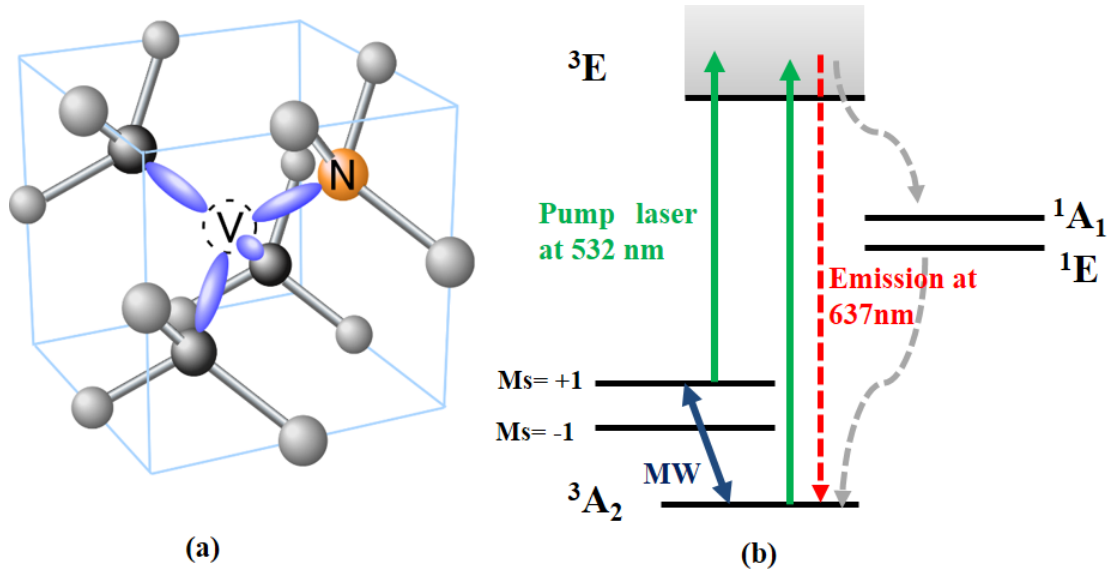


Figure 1-7: Schematic of NV (a) crystal structure [37] and (b) electronic structures [38]. In (a), grey balls represent carbon atoms in the diamond lattice, the yellow ball labelled with letter

“N” represents nitrogen and the dotted circle labelled with letter “V” represents the adjacent vacancy. In (b) the solid lines represent the energy levels, in which the 3A_2 represents the ground triplet state, 3E represents the excited triplet state, 1A_1 and 1E represent the singlet states, respectively and the $M_s=\pm 1$ represent the split energy levels of the ground state due to the external microwave field as represented by “MW”. The green solid arrow represents the exciting green laser at 532 nm and the dotted red arrow represents the emission at 637 nm, the dotted grey arrows representing the non-radiative decay [38].

However, issues still remain for effectively utilising such defects in practice. On one hand, the interaction of the NV centre with the emitted photon is weak in free space. On the other hand, the emission at zero phonon line of the NV is only 4% of the total emissions, with the rest coming from broad sidebands [3]. The measured emission spectra from the NV centre at cryogenic ($T=1.8$ K) and room temperature ($T=300$ K) are shown in Figure 1-8. As shown, the sharp ZPL emission at 637nm is only a small portion of the broad total emission spectrum, which ranges from 630 nm to 800 nm. This makes the efficiency of using the desired NV emission at ZPL relatively low. Thus, a method of enhancing the emission from the ZPL of the NV is necessary.

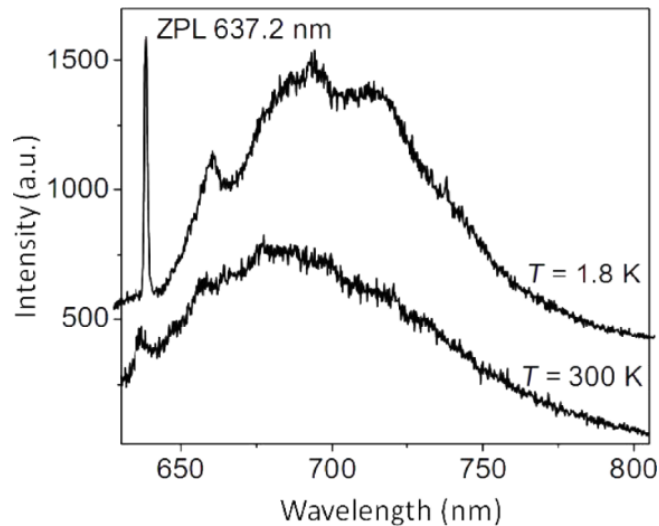


Figure 1-8: Emission spectra from NV at cryogenic ($T=1.8$ K) and room temperature ($T=300$ K), respectively [39].

Another technological problem to be addressed is the positioning of single NV centres. A sufficient positioning accuracy is necessary to guarantee an interaction between adjacent NV spins. Although regular arrays of single NV centres have been created, the positioning accuracy achieved has not been sufficient to realise actual applications [40] with a state-of-the-art spatial resolution ~ 2 nm [41].

Furthermore, some applications based on NV centres in diamond have specific material requirements. For example, a diamond must be of ultra-high purity for

quantum technologies where the spin coherence is critical. The diamond crystal size and the optical stability of the hosted NV centres are also crucial for high-resolution magnetometer use and biomedical imaging [3]. Moreover, it has been shown that for many applications, the NV centre needs to be created as close as possible (< 5 nm) to the diamond surface [42]. To overcome these challenges, advanced fabrication techniques have to be developed. Some of these techniques will be described later in this thesis.

Applications of diamond NV centres

Over the past decade, diamond NV centres have been investigated extensively for applications in QIP. Some of these investigations aimed to enhance the collection efficiency of photons emitted from NV centres in the diamond substrate. Other investigations have focused on the modification of the spectral emission of the NV centre towards the ZPL. These include using diamond photonic devices such as solid immersion lenses (SILs) to increase the collection efficiency [43] or alternatively coupling the radiating NV centre to a localised mode of a high-Q cavity e.g. microspheres [44], micro-discs [45] or photonic crystal cavities [46]. Different cavity schemes using hybrid methods have also been proposed. These hybrid approaches aimed to exploit the coupling of the NV centre with localised surface plasmons. This coupling helps to achieve an enhanced emission from the NV centre [47].

In addition to being a building block for applications in QIP, the diamond NV centre is also a promising platform for sensing applications. In particular, the NV defect has strong sensitivity to magnetic field [48], electric field [49], strain [50], pressure [51] and its emission is temperature dependent [52]. The expression below shows how the Hamiltonian of the NV centre is related to these parameters.

$$H = D \cdot S_z^2 + \mathbf{E} \cdot (S_x^2 - S_y^2) - \gamma_e \mathbf{B} \cdot \mathbf{S} + \mathbf{S} \cdot \sum_i \mathbf{A}_i \cdot \mathbf{I}_i$$

Temperature
sensing

Electric/strain
field sensing

Magnetic
field

Electronic
spin

Hamiltonian of NV centres for different sensing fields [53]. $D = 2.87$ GHz is the zero-field splitting, \mathbf{B} is the applied magnetic field, and \mathbf{S} is the electron spin operator, S_x, S_y, S_z are the spins in x,y,z directions, respectively. \mathbf{E} is the vector electric field, γ_e is the electron gyromagnetic ratio, $\gamma_e \mathbf{B}$ is the Zeeman splitting, $\mathbf{S} \sum_i \mathbf{A}_i \cdot \mathbf{I}_i$ is the hyperfine term.

1.4 Diamond processing

As described above, the outstanding properties of diamond make it a highly desirable material for many applications. However, due to its mechanical hardness and chemical inertness, processing diamond is a challenge. To date, several techniques have been developed for this purpose and each has its own advantages and limitations. These techniques include cutting, polishing, laser machining, focused ion beam (FIB) milling and dry etching. This section will give an overview of these techniques.

1.4.1 Cutting

Cutting is an important mechanical process which cuts a diamond to a desired size. Diamond cutting begins with examining and marking the diamond. The diamond can be cut by cleaving, mechanical sawing or laser cutting techniques.

a) Cleaving

Diamond cleavage occurs predominantly along a set of crystalline planes. For diamond, the easiest cleavage plane is (111) [54]. When cleaving, a diamond is set in a holder called a “dop”. A scratch groove is made first by using another diamond. Then, a steel knife is set into the groove and is tapped with a wooden mallet. If the scratch groove was made accurately along the crystalline plane, the diamond will cleave easily. However, if the scratch is misaligned, the mallet tap may shatter the diamond.

b) Mechanical sawing

For diamond sawing, the diamond sample is set into a “dop” (a small cup or collet) and is then clamped into an arm above a saw. The saw revolves at a high speed. Traditionally, a special diamond saw is used for cutting the diamond [2].

c) Laser cutting

Diamond can be cut by using a pulsed laser beam. Diamond is prone to crack during laser processing. The crack is due to the phase transition from diamond to graphite. In order to achieve successful cutting, the pulse duration of the laser beam should be adjusted carefully according to the type of diamond. The cutting surfaces are normally poor (up to μm scale root-mean-square roughness [2]) and a further polishing process is required in order to improve the surface quality. A pulsed laser

used for laser cutting typically has a wavelength of 1064 nm and power around 50 W with a duration of 0.2 ns.

1.4.2 Polishing

Diamond polishing is an important process to obtain a highly smooth surface finish. There are two main types of diamond polishing method: scaife polishing and resin-bonded polishing [55].

a) Scaife polishing

A scaife is a metal wheel. The wheel can be made of different materials such as cast iron or bronze. It is typically "dressed" by impregnating the surface of the wheel with diamond grit or powder prior to polishing. The diamond sample is clamped in a hand-held metal holder and diamond polishing is carried out on the rotating 'scaife' wheel, which is about 0.3 m in diameter and 20 mm thick. During polishing, the wheel spins with a speed of about 3000 revolutions per minute (RPM), giving a linear velocity at the outer radius of 50 m/s [56]. Diamond polished using this method typically has groove features parallel to the polishing directions. The achieved diamond surface normally has a surface roughness of around 5 nm. The resulted surface roughness is mainly dependent on the grits and the polish directions that are used.

b) Resin-bonded polishing

The resin-bonded polishing method involves polishing diamond with a wheel similar to scaife polishing. The wheel is typically made of organic resin on which diamond grit was pre-embedded. The use of the resin-bonded polishing avoids the interruption and skilled labour necessary in keeping a cast-iron scaife fully charged with diamond powder. This is important in production in automatic production lines. Unlike scaife polishing, the diamond can be polished in more difficult directions such as the $\langle 110 \rangle$ direction on (100) and (110) planes of diamond and is of particular use for polishing polycrystalline diamonds. The polished diamond surface usually has a roughness around 2-3 nm.

1.4.3 Focused ion beam milling

Diamond focused ion beam (FIB) milling is a process of sputtering the diamond surface with non-reactive ion beams [57]. FIB milling is a technique that has been

widely used in the semiconductor industry, materials science and increasingly in the biological field, for material micromachining, microstructure fabrication, site-specific analysis and deposition.

FIB milling offers accessibility to processing diamond on the micro/nano-scale with high precision and allows processing of complex shapes by simply varying the incidence angle of the ion source. However, we note that the FIB milling method is very time-consuming due to the slow FIB process. Additionally, the structure fabrication by using FIB milling is fundamentally limited by ion beam resolution, pattern reproducibility and writing size. For example, to mill a structure in a 330 nm layer, a 30 keV gallium beam at 100 pA can be used. The milling process takes a few minutes with a diamond etch rates of around 100 nm/min. When milling times exceed 10 min, beam drift can also become a problem. Consequently, larger structures must be written faster at higher currents, which leads to a fall in feature resolution. At higher currents, beam divergence and sputtering effects lead to the rounding of cuts and features [58]. Due to above limitations, FIB milling is suited to prototype devices rather than to industrial fabrication. The FIB is able to fabricate structures down to 10 nm in size, a processing resolution the laser processing cannot reach [2].

1.4.4 Dry etching

Dry etching is a method to remove the material from the surface of a specimen by exposing the surface to plasma or etchant gases. The plasma and etchant gases are generated in an etching chamber.

Dry etching is an industrial-scale process [59]. Compared to the other diamond process methods, dry etching has the following advantages: isotropic or anisotropic etching controllability; directional etching of materials independent of crystal orientation; faithful transfer of lithographically-defined photoresist (PR) patterns into underlying layers; high resolution and cleanliness; less undercutting; no unintentional prolongation of etching; better process control; ease of automation (e.g., cassette loading) and capability of defining small feature size (< 100 nm) [60]. Among all the dry etching methods, inductively coupled plasma (ICP) etching gives the most controllable etching process, lowest surface roughness and a relatively high etching rate.

Importantly, ICP etching processes are capable of producing optical quality surfaces that exhibit a low degree of roughness. The optical quality surface is critical to micro-optical and photonic devices. Materials used to mask diamond for dry etching include metal (e.g. Cr) [61] and dielectric and resist films (SiO_2 , PR, hydrogen silsesquioxane (HSQ)) [62] and also nanoparticles (Au, SiO_2 , Al_2O_3) [63]. To allow fabrication of high-aspect ratio diamond structures, an appropriate etching selectivity of the mask versus the diamond is necessary [64].

For the above reasons, ICP etching is the most suitable method for diamond processing on a large scale and so it is the main method used for the diamond processing in this thesis work. The detail of this method will be introduced in Chapter 2.

1.5 Diamond photonic devices

A large number of diamond photonic devices have been developed in recent years for various applications. A selection of these diamond photonic devices which are directly relevant to this thesis work will be briefly reviewed in this section.

1.5.1 Diamond optics

With the advance of diamond synthesis and fabrication techniques, different diamond optical structures have been developed in recent years. Due to its high refractive index and large transparency window, diamond has been applied, for example, as an X-ray window material [64] and in lenses for spectroscopy [65]. In this section, optical devices fabricated on bulk diamonds are introduced. These devices include diamond lenses (optical lenses and SILs) as well as diamond nanopillars and diamond gratings.

Diamond lenses

a) Common optical lenses

Given their universal use in the world of optics, it is natural that lenses have been among the first components to be considered for diamond optics. Diamond lens fabrication has a long history. In 1842, A. Pritchard, an optician, ground and polished the first diamond lens [66]. These early diamond lenses were used for microscopy [65].

With the advance of CVD techniques, which can be used to deposit high-quality diamond onto flat or structured wafers, it is now possible to produce the diamond lenses in a cheaper manner. The applications of diamond lenses have thus expanded considerably. For example, using the high thermal conductivity of diamond, diamond lenses have been developed for applications in high power lasers and LEDs. Diamond lenses developed for such purposes have been reported by several groups worldwide such as Woerner *et al.*[67], M. Karlsson *et al.* [68], W. G. M. Nelissen *et al.* [69] and Gu *et al.*[70-73].

Miniature diamond lenses (micro or nano scale) for applications in monolithic laser resonators as well as in quantum photonic cavities has attracted much attention in recent years. However, to achieve such micro/nano-diamond lenses with a high surface quality is difficult by using conventional fabrication techniques such as polishing or laser machining.

Diamond micro-lenses with a high surface quality can be achieved by combining the thermal reflow of PR with the dry etching method which transfers the PR micro-lens geometry into diamond. By using these combined techniques, various diamond lenses have been fabricated. However, the controllability of the PR lens formation process on the diamond surface is low and the PR reflow mechanism is still not fully clear. For such reasons, a detailed study of the PR thermal reflow process was carried out in this work as will be introduced in Chapter 3. Based on this study, diamond micro-lenses with a state-of-the-art large radius of curvature (ROC) of over 13 mm have been achieved [74]. The development of these large ROC diamond micro-lenses has enabled the monolithic diamond Raman lasers [75].

b) Diamond solid immersion lenses

An solid immersion lens (SIL) is a hemispherical lens made of a high-refractive-index solid material. If a point light source such as a NV emitter is located at the centre of an SIL, the SIL will reduce the emission light losses due to total internal reflections (TIRs) at the diamond-air interface (shown in Figure 1-9 (a) and (b)). It also offers higher magnification and higher numerical aperture than common lenses. The development of such SIL structures on diamond thus helps to enhance the collection efficiency of the single photon emission from such centres as NV's.

Diamond SILs were first reported in 2006 [76]. Due to the high aspect ratio of SILs, their fabrication at the micron scale normally involves FIB milling. J. P. Hadden *et al.* achieved diamond SILs using FIB milling, however concentric ring structures were observed on these SIL surfaces [77]. Alignment of SILs to the individual colour centres has been achieved by registering a confocal fluorescence microscopy image to an FIB-written ruler. These markers are used as references when milling the SIL [78]. By using SILs, an eightfold increase in the collection efficiency was demonstrated as shown in Figure 1-9 (c). Similar SILs have been exploited to provide a higher count rate from two distinct NV emitters by Ronald Hanson's group [79], allowing for quantum interference measurements between two photons and high-fidelity projective read-out of a solid-state spin quantum register [80]. P. Siyushev *et al.* also reported one order of magnitude increase in the efficiency for the detection of single photon emission by adding a diamond SIL [81]. At present, both hemispherical and super-hemispherical diamond SILs are commercially available, and may find future application in diamond-based quantum optical systems or in optical data storage involving UV lasers [81].

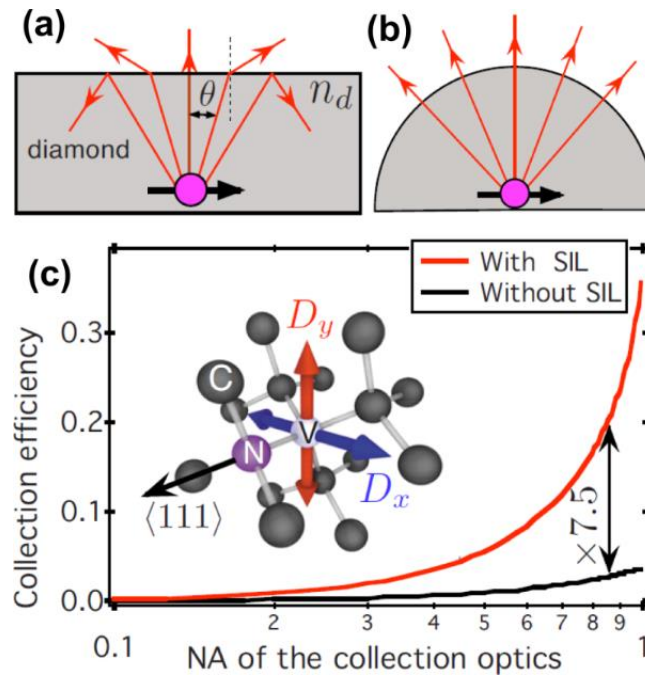


Figure 1-9: Schematic of an SIL fabricated in a diamond sample, (a) shows the TIR inside a diamond; (b) shows the enhanced extraction efficiency using SIL structure and (c) shows a plot of the comparison between the collection efficiencies with a SIL and without a SIL.

Figure sourced from [39].

Diamond nanopillars and diamond gratings

It is worth noting that some other micro/nano-diamond photonic structures offering the same function as the SILs have been demonstrated. These devices include diamond nanopillars as reported in [82] and diamond “bullseye” gratings as reported in [83].

Arrays of uniform diamond nanopillars are reported in [82], in which ~ 200 nm-diameter, $2\ \mu\text{m}$ -high nanopillars were achieved in a Type Ib diamond. With these nanopillars, a maximum tenfold increase in photon flux was observed compared to the representative NV emissions in bulk diamond.

A diamond “bullseye” grating consists of concentric slits that are fully etched into a diamond membrane [83]. The grating period a satisfies the second-order Bragg condition, $a = \lambda/n_{\text{eff}}$, where $\lambda = 680$ nm approximates the mean of the NV emission wavelength and n_{eff} is the membrane’s effective index when placed on glass. Light guided in the membrane scatters with equal phases at the slits, leading to constructive interference in the vertical direction.

1.5.2 Diamond Raman laser

The frequency of the incident light can be changed via stimulated Raman scattering (SRS) when using diamond as the gain medium. Owing to the high thermal conductivity and the high Raman gain coefficient, diamond has attracted much attention for application in Raman lasers. The high thermal conductivity means an efficient thermal management within the Raman lasers which is important as SRS implicitly generates heat. The high Raman gain coefficient means a short length of laser crystal is needed and thus a compact laser configuration can be achieved.

The diamond Raman lasers can be used to provide access to wavelengths that are hard to reach otherwise. For example, compact and robust diamond Raman lasers that convert widely available pulsed green lasers to the yellow-orange spectral region (a region safe for phototherapies) are highly desired for biomedical applications [84].

Diamond Raman lasers are usually composed of a pump laser source, a diamond as the Raman gain medium and external mirrors used to form a laser resonator [85]. Diamond Raman lasers with output power of $1.6\ \text{W}$ [86] to over $100\ \text{W}$ [87] in continuous wave (CW) operation [88] have been reported.

However, a novel compact and robust monolithic diamond Raman laser can be achieved. The monolithic diamond Raman laser needs minimal alignments of the experimental setup and has no further requirements of external mirrors [75]. The detail of the development of this monolithic diamond Raman laser will be reported in Chapter 4.

1.5.3 Cavity-coupled diamond photonics

To tackle the issue of the NV centre's broad sideband-emission as mentioned in Section 1.3.2, it is necessary to enhance the NV emission at the ZPL. Coupling the NV emission to an optical cavity is a promising solution to this issue [89]. An optical cavity is a resonant structure that reinforces a narrow spectral emission band e.g. the NV emission at the ZPL. For diamond NV emissions, the reinforcement is realised by coupling the NV centre emission in resonance to a certain cavity mode that overlaps the emission spectrum. The principle of this reinforcement is described as cavity-quantum electrodynamics (cavity-QED), as will be introduced in Chapter 5. Several examples of such cavities include the photonic crystal cavity [90], the whispering gallery mode cavity [91] and the Fabry-Perot cavity [92]. Figure 1-10 shows an overview of these cavity designs with their cavity parameters: the cavity quality factor Q (representing the frequency to bandwidth ratio, $\omega_r/\Delta\omega$) and the cavity mode volume V . These parameters can directly influence the enhancement of the cavity-coupled emission.

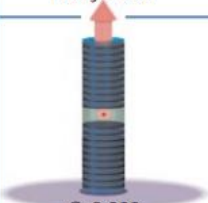
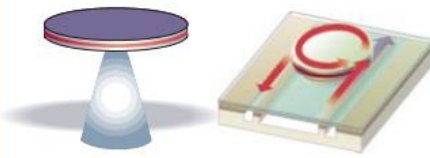

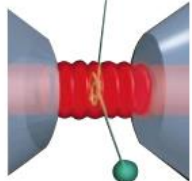
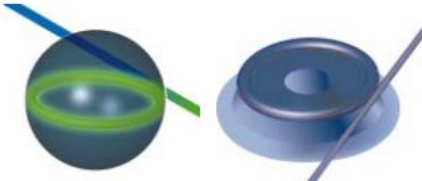
	Fabry-Perot	Whispering gallery	Photonic crystal
High Q	 $Q: 2,000$ $V: 5 (\lambda/n)^3$	 $Q: 12,000$ $V: 6 (\lambda/n)^3$ $Q_{III-V}: 7,000$ $Q_{Poly}: 1.3 \times 10^5$	 $Q: 13,000$ $V: 1.2 (\lambda/n)^3$
Ultrahigh Q	 $F: 4.8 \times 10^5$ $V: 1,690 \mu\text{m}^3$	 $Q: 8 \times 10^9$ $V: 3,000 \mu\text{m}^3$ $Q: 10^8$	

Figure 1-10: Overview of optical micro-cavities with different Q factors and mode volumes (V). After [93].

The cavity-coupling of the diamond NV centre emission has been extensively studied in recent years [94] and two approaches have been mainly used. The first is to fabricate photonic cavities directly in a bulk diamond around pre-selected NV centres. This approach is normally classified as ‘monolithic diamond cavities’ [46,95,96]. The diamond photonic crystal cavity is one of the examples of such an approach. Alternatively, another approach is the hybrid method, which involves the integration of diamond NV centres to a photonic cavity formed in conventional photonic media. Examples of this approach include the hybrid whispering gallery mode cavities [44] and the Fabry-Perot cavity-coupled NV centres in diamond [92].

Monolithic diamond photonic crystal

A diamond photonic crystal (PhC) cavity is a periodic dielectric structure that can prohibit the propagation of light for all directions within a frequency range. These photonic crystal cavities allow one to modify the spontaneous emission. During the past decade, photonic crystal cavities have become the benchmark for high-Q, low-V optical cavities, via their ability to confine light efficiently in-plane [90]. Diamond photonic crystal cavities have been fabricated both in two-dimensional planes and one-dimensional nano-beams [95], by now with over 70 times emission enhancement reported with an acceptable tunability of the cavity-mode [96]. The coupling of NV centres in the resonance of such photonic crystal cavities has been demonstrated recently with a strong enhancement of the ZPL emission [97].

Hybrid systems

For the hybrid system, the obvious advantage is to combine diamond NV centres with more mature semiconductor fabrication techniques and conventional semiconductor materials. GaP is an example of such a material for cavity applications due to its transparency in the visible, high refractive index (~3.25) and a range of available machining techniques. These advantages allow the efficient coupling of light and the use of advanced fabrication methods. For such reasons, cavity-coupling of diamond NV emission to GaP waveguides [98] and GaP micro-disks [99] has been demonstrated.

However, the drawbacks of the hybrid method are the high coupling loss at the interface. Moreover, the relatively inflexible tuning of the cavity mode limits the

capability of the cavity mode to overlap the ZPL emission. The NV centre in diamond thus needs to be characterised with high accuracy and its position and orientation needs to be optimised so as to be coupled to the cavity mode [100].

The above-mentioned systems promise intimate coupling between the emitters and the cavity mode with potentially the smallest achievable mode volumes. However, the tuning of the cavity mode is difficult. An alternative approach is to use the external Fabry-Perot cavities to couple the NV emission, which has the advantage of great flexibility in terms of alignment and spectral tuning [101].

The Fabry-Perot cavity-coupled NV in nanodiamond has been reported in [102]. The reported cavity has a mode volume of $4.7 \lambda^3$, where $\lambda = 637$ nm is the wavelength of the ZPL emission from the NV centre, and a cavity $Q > 3000$. These combined parameters are good enough to enhance the spontaneous emission rate of an NV in diamond. Moreover, all of the steps in this reported work are scalable and tunable, which means that it is possible to make multiple coupled NV cavities to realise networked QIP. The relatively large cavity design also enables the integration of the cavity structure with microwave lines which can control the NV spins in the ground states. However, both emission and ground state lifetime of NV centres in nanodiamonds are significantly worse than those from large single-crystal diamonds due to the inhomogeneous broadening of the spectrum emission of NV centres in nanodiamonds [92]. Additionally, the alignment of the nanodiamond, and hence the orientation of the NV with respect to the cavity mode, is difficult. The development of high quality single crystal diamond membranes will remove these problems. A diamond membrane containing the NV centres is a versatile platform for QIP instead of nanodiamonds. Cavity-coupling the single NV emission in a diamond membrane has advantages in both flexibility and tunability.

Diamond membranes have been fabricated using “bottom-up” methods and “top-down” methods. The “bottom-up” methods used homoepitaxial growth of diamond on top of a single crystal diamond substrate [103]. The “top-down” method thins down a thicker diamond platelet (e.g. 20 μm) to a thinner membrane. The methods used for diamond thinning included ion implantation [104], FIB milling [105], laser cutting [106] and template polishing [107].

Using ICP etching to thin down diamond platelet is an effective method. ICP etching gives the least damage to the diamond sample and thus has the least detrimental influence on the colour centres [108]. However, large size (> 2 mm) freestanding diamond membranes with thickness below $1\ \mu\text{m}$ without cracking or damage have not yet been reported prior to our work.

In this thesis work, the fabrication method of large size ultrathin diamond membranes was developed. A diamond membrane with size as large as 3 mm in diameter and thicknesses ranged from 250 nm to $1\ \mu\text{m}$ has been achieved. This diamond membrane was coupled to an open Fabry-Perot cavity for the first time to demonstrate the cavity enhanced emission. The detail of this work will be reported in Chapter 5.

1.6 Outline of this thesis

Recent breakthroughs in the synthesis of diamond have resulted in availability of diamond materials with improved optical quality, high purity and relatively low cost. These improvements have significantly stimulated the development of novel technologies for new applications. In this chapter, diamond properties, synthesis, processing and diamond photonic devices were briefly reviewed.

In Chapter 2, the experimental facilities used in this thesis work will be introduced, including the tools used for fabrication and equipments used for characterisation. To control the shape of resulting diamond structures with spherical or aspheric features, a detailed study of PR thermal reflow process is carried out in Chapter 3. Combining this study with the optimization of ICP diamond etching, novel diamond micro-lenses with a large radius of curvature (ROC) on bulk single crystal diamond have been realised. These diamond lenses have enabled novel monolithic diamond Raman lasers. The detail of the development of such monolithic diamond Raman lasers will be introduced in Chapter 4. Large size single crystal diamond membranes that host NV centres pave the way of diamond photonic devices for applications in QIP. The detail of the development of such large size diamond membranes will be introduced in Chapter 5. Diamond membranes with wavelength-scale thicknesses (< 250 nm) were developed. By coupling with an open optical Fabry-Perot cavity, enhanced emission is realised. This result has a high impact on the scalable construction of quantum computing based

on diamond NV centres. A summary of the work discussed in this thesis and further work for the future will be presented in Chapter 6.

References

- [1] B.E.A. Saleh, M.C. Teich, *Fundamentals of photonics*, Wiley, (1991).
- [2] R. Mildren, J. Rabeau, *Optical Engineering of Diamond*, Wiley, (2013).
- [3] S. Praver, I. Aharonovich, *Quantum Information Processing with Diamond: Principles and Applications*, Elsevier, (2014).
- [4] K.H.J. Buschow, *Encyclopedia of Materials: Science and Technology*, Elsevier, (2001).
- [5] F. Fizzotti, A. Lo Giudice, C. Manfredotti, C. Manfredotti, M. Castellino, E. Vittone, *Diamond surface conductivity after exposure to molecular hydrogen*, *Diamond and Related Materials*, **16**, 836 (2007).
- [6] S.J. Sque, *A first-principles study on bulk and transfer doping of diamond*, University of Exeter, (2005).
- [7] B.L. Jones, *Properties of natural and synthetic diamond*. *Advanced Materials*, **5(9)**, 681 (1993).
- [8] E.S.D. Sa, G. Davies, *Uniaxial Stress Studies of the 2.498 eV (H4), 2.417 eV and 2.536 eV Vibronic Bands in Diamond*. *Proceedings of the Royal Society of London A: Mathematical, Physical and Engineering Sciences*, **357**, 231 (1977).
- [9] A.M. Zaitsev, *Optical Properties of Diamond: A Data Handbook*, Springer Berlin Heidelberg, (2010).
- [10] R. Abbaschian, H. Zhu, C. Clarke, *High pressure–high temperature growth of diamond crystals using split sphere apparatus*, *Diamond and Related Materials*, **14**, 1916 (2005).
- [11] S.A. Solin, *Photoluminescence of natural type I and type IIb diamonds*, *Physics Letters A*, **38**, 101 (1972).
- [12] "Diamond–Molecule of the Month":
<http://www.bris.ac.uk/Depts/Chemistry/MOTM/diamond/diamond.htm>.
- [13] A.T. Collins, A. Connor, C.-H. Ly, A. Shareef, P.M. Spear, *High-temperature annealing of optical centres in type-I diamond*, *Journal of Applied Physics*, **97**, 083517 (2005).
- [14] A.T. Collins, *The Optical and Electronic Properties of Semiconducting Diamond*, *Philosophical Transactions of the Royal Society of London A: Mathematical, Physical and Engineering Sciences*, **342**, 233 (1993).
- [15] J. Walker, *Optical absorption and luminescence in diamond*, *Reports on Progress in Physics*, **42**, 1605 (1979).
- [16] H.P. Bovenkerk, F.P. Bundy, R.M. Chrenko, P.J. Codella, H.M. Strong, R.H. Wentorf, *Errors in diamond synthesis*, *Nature*, **365**, 19 (1993).
- [17] F.P. Bundy, H.T. Hall, H.M. Strong, R.H. Wentorf, *Man-Made Diamonds*, *Nature*, **176**, 51 (1955).
- [18] H.T. Hall, *Ultra-High-Pressure, High-Temperature Apparatus: the "Belt"*, *Review of Scientific Instruments*, **31**, 125 (1960).

- [19] Synthetic diamond manufacturers:
https://en.wikipedia.org/wiki/List_of_synthetic_diamond_manufacturers
- [20] "Diamonds Are A Scientist's Best Friend":
<https://www.sciencedaily.com/releases/2005/08/050808064656.htm>
- [21] H.T. Hall, Some High-Pressure, High-Temperature Apparatus Design Considerations: Equipment for Use at 100,000 Atmospheres and 3000°C, *Review of Scientific Instruments*, **29**, 267 (1958).
- [22] N. Pal'yanov, A.G. Sokol, M. Borzdov, A.F. Khokhryakov, Fluid-bearing alkaline carbonate melts as the medium for the formation of diamonds in the Earth's mantle: an experimental study, *Lithos*, **60**, 145 (2002).
- [23] M. Werner, R. Locher, Growth and application of undoped and doped diamond films, *Reports on Progress in Physics*, **61**, 1665 (1998).
- [24] S. Koizumi, C. Nebel, M. Nesladek, *Physics and Applications of CVD Diamond*, Wiley, (2008).
- [25] Element Six Ltd. http://www.e6.com/wps/wcm/connect/e6_content_en/home
- [26] Diamond window: http://www.diamond-materials.com/EN/products/optical_windows/overview.htm
- [27] Raman gain: https://www.rp-photonics.com/raman_gain.html
- [28] V.G. Savitski, S. Reilly, A.J. Kemp, Steady-State Raman Gain in Diamond as a Function of Pump Wavelength, *IEEE Journal of Quantum Electronics*, **49**, 218 (2013).
- [29] Diamond thermal conductivity data:
https://www.reliabilityanalysislab.com/tl_cw_0309_ThermalManagement.html
- [30] H.D. Young, R.A. Freedman, R. Bhathal, *University Physics: Australian edition*, Pearson Higher Education AU, (2010).
- [31] L.S. Pan, D.R. Kania, *Diamond: Electronic Properties and Applications: Electronic Properties and Applications*, Springer US, (1994).
- [32] D.F. Edwards, E. Ochoa, Infrared refractive index of diamond, *Journal of the Optical Society of America*, **71**, 607 (1981).
- [33] V.V. Dobrovitski, G.D. Fuchs, A.L. Falk, C. Santori, D.D. Awschalom, Quantum Control over Single Spins in Diamond, *Annual Review of Condensed Matter Physics*, **4**, 23 (2013).
- [34] M.W. Doherty, N.B. Manson, P. Delaney, F. Jelezko, J. Wrachtrup, L.C.L. Hollenberg, The nitrogen-vacancy colour centre in diamond, *Physics Reports*, **528**, 1 (2013).
- [35] G. Balasubramanian, P. Neumann, D. Twitchen, M. Markham, R. Kolesov, N. Mizuochi, J. Isoya, J. Achard, J. Beck, J. Tissler, V. Jacques, P.R. Hemmer, F. Jelezko, J. Wrachtrup, Ultralong spin coherence time in isotopically engineered diamond, *Nature Materials*, **8**, 383 (2009).
- [36] I. Aharonovich, S. Castelletto, D.A. Simpson, C.H. Su, A.D. Greentree, S. Praver, Diamond-based single-photon emitters, *Reports on Progress in Physics*, **74**, 076501 (2011).
- [37] F. Takahiro, D. Yuki, M. Takehide, M. Yoshiyuki, K. Hiromitsu, M. Tsubasa, M. Toshiharu, Y. Satoshi, M. Ryusuke, T. Norio, H. Mutsuko, S. Yuki, M. Hiroki, T. Toshiyuki, M. Shinji, S.

- Yoshishige, M. Norikazu, Perfect selective alignment of nitrogen-vacancy centers in diamond, *Applied Physics Express*, **7**, 055201 (2014).
- [38] S. Arroyo-Camejo, A. Lazarev, S.W. Hell, G. Balasubramanian, Room temperature high-fidelity holonomic single-qubit gate on a solid-state spin, *Nature Communications*, **5**, 1 (2014).
- [39] K. Beha, H. Fedder, M. Wolfer, M.C. Becker, P. Siyushev, M. Jamali, A. Batalov, C. Hinz, J. Hees, L. Kirste, H. Obloh, E. Gheeraert, B. Naydenov, I. Jakobi, F. Dolde, S. Pezzagna, D. Twittchen, M. Markham, D. Dregely, H. Giessen, J. Meijer, F. Jelezko, C.E. Nebel, R. Bratschitsch, A. Leitenstorfer, J. Wrachtrup, *Diamond nanophotonics*, *Beilstein Journal of Nanotechnology*, **3**, 895 (2012).
- [40] J. Meijer, B. Burchard, M. Domhan, C. Wittmann, T. Gaebel, I. Popa, F. Jelezko, J. Wrachtrup, Generation of single color centers by focused nitrogen implantation, *Applied Physics Letters*, **87**, 261909 (2005).
- [41] Lesik, M., Raatz, N., Tallaire, A., Spinicelli, P., John, R., Achard, J., Gicquel, A., Jacques, V., Roch, J.-F., Meijer, J. and Pezzagna, S., Production of bulk NV centre arrays by shallow implantation and diamond CVD overgrowth, *Physica Status Solidi*, **213**, 2788 (2016).
- [42] L.M. Pham, S.J. DeVience, F. Casola, I. Lovchinsky, A.O. Sushkov, E. Bersin, J. Lee, E. Urbach, P. Cappellaro, H. Park, A. Yacoby, M. Lukin, R.L. Walsworth, NMR technique for determining the depth of shallow nitrogen-vacancy centers in diamond, *Physical Review B*, **93**, 045425 (2016).
- [43] S. Tim, G. Friedemann, B. Moritz Julian, B. Oliver, Ultrabright and efficient single-photon generation based on nitrogen-vacancy centres in nanodiamonds on a solid immersion lens, *New Journal of Physics*, **13**, 055017 (2011).
- [44] S. Stefan, B. Oliver, Coupling single NV-centres to high- Q whispering gallery modes of a preselected frequency-matched microresonator, *Journal of Physics B: Atomic, Molecular and Optical Physics*, **42**, 114001 (2009).
- [45] C. Santori, P.E. Barclay, K.M.C. Fu, R.G. Beausoleil, S. Spillane, M. Fisch, Nanophotonics for quantum optics using nitrogen-vacancy centers in diamond, *Nanotechnology*, **21**, 274008 (2010).
- [46] T. van der Sar, J. Hagemeyer, W. Pfaff, E.C. Heeres, S.M. Thon, H. Kim, P.M. Petroff, T.H. Oosterkamp, D. Bouwmeester, R. Hanson, Deterministic nanoassembly of a coupled quantum emitter–photonic crystal cavity system, *Applied Physics Letters*, **98**, 193103 (2011).
- [47] S. Schietinger, M. Barth, T. Aichele, O. Benson, Plasmon-Enhanced Single Photon Emission from a Nanoassembled Metal–Diamond Hybrid Structure at Room Temperature, *Nano Letters*, **9**, 1694 (2009).
- [48] S. Hong, M.S. Grinolds, L.M. Pham, D. Le Sage, L. Luan, R.L. Walsworth, A. Yacoby, Nanoscale magnetometry with NV centers in diamond, *MRS Bulletin*, **38**, 155 (2013).
- [49] F. Dolde, H. Fedder, M.W. Doherty, T. Nobauer, F. Rempp, G. Balasubramanian, T. Wolf, F. Reinhard, L.C.L. Hollenberg, F. Jelezko, J. Wrachtrup, Electric-field sensing using single diamond spins, *Nature Physics*, **7**, 459 (2011).
- [50] P. Ouartchaiyapong, K.W. Lee, B.A. Myers, A.C.B. Jayich, Dynamic strain-mediated coupling of a single diamond spin to a mechanical resonator, *Nature Communications*, **5**, 1 (2014).

- [51] J. Cai, F. Jelezko, M.B. Plenio, Hybrid sensors based on colour centres in diamond and piezoactive layers, *Nature Communications*, **5**, 1 (2014).
- [52] P. Neumann, I. Jakobi, F. Dolde, C. Burk, R. Reuter, G. Waldherr, J. Honert, T. Wolf, A. Brunner, J.H. Shim, D. Suter, H. Sumiya, J. Isoya, J. Wrachtrup, High-Precision Nanoscale Temperature Sensing Using Single Defects in Diamond, *Nano Letters*, **13**, 2738 (2013).
- [53] J.-W. Zhou, P.-F. Wang, F.-Z. Shi, P. Huang, X. Kong, X.-K. Xu, Q. Zhang, Z.-X. Wang, X. Rong, J.-F. Du, Quantum information processing and metrology with color centers in diamonds, *Frontiers of Physics*, **9**, 587 (2014).
- [54] R.H. Telling, C.J. Pickard, M.C. Payne, J.E. Field, Theoretical Strength and Cleavage of Diamond, *Physical Review Letters*, **84**, 5160 (2000).
- [55] J.R. Hird, J.E. Field, Diamond polishing, *Proceedings of the Royal Society of London A: Mathematical, Physical and Engineering Sciences*, **460**, 3547 (2004).
- [56] Y. Chen, L. Zhang, *Polishing of Diamond Materials: Mechanisms, Modeling and Implementation*, Springer London, (2013).
- [57] T. Zhao, D.F. Grogan, B.G. Bovard, H.A. Macleod, Diamond Optics III, *International Society for Optics and Photonics*, **142**, 1 (1990).
- [58] T.M. Babinec, J.T. Choy, K.J.M. Smith, M. Khan, M. Lončar, Design and focused ion beam fabrication of single crystal diamond nanobeam cavities, *Journal of Vacuum Science & Technology B*, **29**, 010601 (2011).
- [59] S. Kiyohara, K. Mori, I. Miyamoto, J. Taniguchi, Oxygen ion beam assisted etching of single crystal diamond chips using reactive oxygen gas, *Journal of Materials Science: Materials in Electronics*, **12**, 477 (2001).
- [60] H. Xiao, *Introduction to Semiconductor Manufacturing Technology*, Prentice Hall PTR, (2001).
- [61] J.W. Baldwin, M. Zalalutdinov, T. Feygelson, J.E. Butler, B.H. Houston, Fabrication of short-wavelength photonic crystals in wide-band-gap nanocrystalline diamond films, *Journal of Vacuum Science & Technology B*, **24**, 50 (2006).
- [62] B.J.M. Hausmann, M. Khan, Y. Zhang, T.M. Babinec, K. Martinick, M. McCutcheon, P.R. Hemmer, M. Lončar, Fabrication of diamond nanowires for quantum information processing applications, *Diamond and Related Materials*, **19**, 621 (2010).
- [63] D.T. Tran, C. Fansler, T.A. Grotjohn, D.K. Reinhard, J. Asmussen, Investigation of mask selectivities and diamond etching using microwave plasma-assisted etching, *Diamond and Related Materials*, **19**, 778 (2010).
- [64] X. Ying, J. Luo, P. Wang, M. Cui, Y. Zhao, G. Li, P. Zhu, Ultra-thin freestanding diamond window for soft X-ray optics, *Diamond and Related Materials*, **12**, 719 (2003).
- [65] A. Pritchard, *The Microscopic Cabinet of Select Animated Objects: With a Description of the Jewel and Doublet Microscope*, Whittaker, Treacher, and Arnot, (1832).
- [66] D. Brewster, *A Treatise, New Philosophical Instruments, for Various Purposes in the Arts and Sciences: With Experiments on Light and Colours*, J. Murray, London; and W. Blackwood, (1813).

- [67] E. Woerner, C. Wild, W. Mueller-Sebert, P. Koidl, CVD-diamond optical lenses, *Diamond and Related Materials*, **10**, 557 (2001).
- [68] M. Karlsson, F. Nikolajeff, Diamond micro-optics: microlenses and antireflection structured 7surfaces for the infrared spectral region, *Optics Express*, **11**, 502 (2003).
- [69] W.G.M. Nelissen, H.P. Godfried, E.P. Houwman, P.A.C. Kriele, J.C. Lamers, G.J. Pels, B.M. Van Oerle, P.G.H.M. Spaay, M.R. McClymont, C.J.H. Wort, Google Patents, (2008).
- [70] E. Gu, H.W. Choi, C. Liu, C. Griffin, J.M. Girkin, I.M. Watson, M.D. Dawson, G. McConnell, A.M. Gurney, Reflection/transmission confocal microscopy characterization of single-crystal diamond microlens arrays, *Applied Physics Letters*, **84**, 2754 (2004).
- [71] C.L. Lee, H.W. Choi, E. Gu, M.D. Dawson, H. Murphy, Fabrication and characterization of diamond micro-optics, *Diamond and Related Materials*, **15**, 725 (2006).
- [72] C.L. Lee, E. Gu, M.D. Dawson, I. Friel, G.A. Scarsbrook, Etching and micro-optics fabrication in diamond using chlorine-based inductively-coupled plasma, *Diamond and Related Materials*, **17**, 1292 (2008).
- [73] Y. Zhang, *Diamond and GaN Waveguides and Microstructures for Integrated Quantum Photonics*, PhD thesis, University of Strathclyde, (2012).
- [74] H. Liu, S. Reilly, J. Herrnsdorf, E. Xie, V.G. Savitski, A.J. Kemp, E. Gu, M.D. Dawson, Large radius of curvature micro-lenses on single crystal diamond for application in monolithic diamond Raman lasers, *Diamond and Related Materials*, **65**, 37 (2016).
- [75] S. Reilly, V.G. Savitski, H. Liu, E. Gu, M.D. Dawson, A.J. Kemp, Monolithic diamond Raman laser, *Optics Letters*, **40**, 930 (2015).
- [76] S. Masataka, S. Kimihiro, K. Takao, N. Ariyoshi, F. Motohiro, T. Minoru, Y. Masanobu, J.S. Thomas, M.v.O. Bart, P.G. Herman, A.C.K. Paul, P.H. Evert, H.M.N. Wim, J.P. Gert, G.M.S. Paul, High-Density Near-Field Readout Using Diamond Solid Immersion Lens, *Japanese Journal of Applied Physics*, **45**, 1311 (2006).
- [77] J.P. Hadden, J.P. Harrison, A.C. Stanley-Clarke, L. Marseglia, Y.-L.D. Ho, B.R. Patton, J.L. O'Brien, J.G. Rarity, Strongly enhanced photon collection from diamond defect centers under microfabricated integrated solid immersion lenses, *Applied Physics Letters*, **97**, 241901 (2010).
- [78] L. Marseglia, J.P. Hadden, A.C. Stanley-Clarke, J.P. Harrison, B. Patton, Y.-L.D. Ho, B. Naydenov, F. Jelezko, J. Meijer, P.R. Dolan, J.M. Smith, J.G. Rarity, J.L. O'Brien, Nanofabricated solid immersion lenses registered to single emitters in diamond, *Applied Physics Letters*, **98**, 133107 (2011).
- [79] H. Bernien, L. Childress, L. Robledo, M. Markham, D. Twitchen, R. Hanson, Two-Photon Quantum Interference from Separate Nitrogen Vacancy Centers in Diamond, *Physical Review Letters*, **108**, 043604 (2012).
- [80] L. Robledo, L. Childress, H. Bernien, B. Hensen, P.F.A. Alkemade, R. Hanson, High-fidelity projective read-out of a solid-state spin quantum register, *Nature*, **477**, 574 (2011).

-
- [81] P. Siyushev, F. Kaiser, V. Jacques, I. Gerhardt, S. Bischof, H. Fedder, J. Dodson, M. Markham, D. Twitchen, F. Jelezko, J. Wrachtrup, Monolithic diamond optics for single photon detection, *Applied Physics Letters*, **97**, 241902 (2010).
- [82] T.M. Babinec, J.M. Hausmann, Birgit, M. Khan, Y. Zhang, J.R. Maze, P.R. Hemmer, M. Loncar, A diamond nanowire single-photon source, *Nature Nanotechnology*, **5**, 195 (2010).
- [83] S. Ates, L. Sapienza, M. Davanco, A. Badolato, K. Srinivasan, Bright Single-Photon Emission From a Quantum Dot in a Circular Bragg Grating Microcavity, *IEEE Journal of Selected Topics in Quantum Electronics*, **18**, 1711 (2012).
- [84] A.D. Greentree, S. Prawer, Yellow lasers: A little diamond goes a long way, *Nature Photonics*, **4** (2010) 202.
- [85] R.P. Mildren, J.E. Butler, J.R. Rabeau, CVD-diamond external cavity Raman laser at 573 nm, *Optics Express*, **16**, 18950 (2008).
- [86] W. Lubeigt, V.G. Savitski, G.M. Bonner, S.L. Geoghegan, I. Friel, J.E. Hastie, M.D. Dawson, D. Burns, A.J. Kemp, 1.6 W continuous-wave Raman laser using low-loss synthetic diamond, *Optics Express*, **19**, 6938 (2011).
- [87] R.J. Williams, O. Kitzler, A. McKay, R.P. Mildren, Investigating diamond Raman lasers at the 100W level using quasi-continuous-wave pumping, *Optics Letters*, **39**, 4152 (2014).
- [88] O. Kitzler, A. McKay, R.P. Mildren, Continuous-wave wavelength conversion for high-power applications using an external cavity diamond Raman laser, *Optics Letters*, **37**, 2790 (2012).
- [89] H. Mabuchi, M. Armen, B. Lev, M. Loncar, J. Vuckovic, H.J. Kimble, J. Preskill, M. Roukes, A. Scherer, S.J. Van Enk, Quantum networks based on cavity QED. *Quantum Information and Computation*, **1**, 7 (2001).
- [90] M. Maldovan, E.L. Thomas, Diamond-structured photonic crystals, *Nature Materials*, **3**, 593 (2004).
- [91] M. Mitchell, B. Khanaliloo, D.P. Lake, T. Masuda, J.P. Hadden, P. Barclay, Conference on Lasers and Electro-Optics, Optical Society of America, San Jose, California, (2016).
- [92] E. Janitz, M. Ruf, M. Dimock, A. Bourassa, J. Sankey, L. Childress, Fabry-Perot microcavity for diamond-based photonics, *Physical Review A*, **92**, 043844 (2015).
- [93] K.J. Vahala, Optical microcavities, *Nature*, **424**, 839 (2003).
- [94] T. Schröder, S.L. Mouradian, J. Zheng, M.E. Trusheim, M. Walsh, E.H. Chen, L. Li, I. Bayn, D. Englund, Quantum nanophotonics in diamond [Invited], *Journal of the Optical Society of America B*, **33**, B65 (2016).
- [95] L. Li, T. Schröder, E.H. Chen, H. Bakhru, D. Englund, One-dimensional photonic crystal cavities in single-crystal diamond, *Photonics and Nanostructures-Fundamentals and Applications*, **15**, 130 (2015).
- [96] A. Faraon, C. Santori, Z. Huang, V.M. Acosta, R.G. Beausoleil, Coupling of Nitrogen-Vacancy Centers to Photonic Crystal Cavities in Monocrystalline Diamond, *Physical Review Letters*, **109**, 033604 (2012).

- [97] L. Li, T. Schröder, E.H. Chen, M. Walsh, I. Bayn, J. Goldstein, O. Gaathon, M.E. Trusheim, M. Lu, J. Mower, M. Cotlet, M.L. Markham, D.J. Twitchen, D. Englund, Coherent spin control of a nanocavity-enhanced qubit in diamond, *Nature Communications*, **6**, 1 (2015).
- [98] K.-M.C. Fu, C. Santori, P.E. Barclay, I. Aharonovich, S. Praver, N. Meyer, A.M. Holm, R.G. Beausoleil, Coupling of nitrogen-vacancy centers in diamond to a GaP waveguide, *Applied Physics Letters*, **93**, 234107 (2008).
- [99] P.E. Barclay, K.-M.C. Fu, C. Santori, R.G. Beausoleil, Chip-based microcavities coupled to nitrogen-vacancy centers in single crystal diamond, *Applied Physics Letters*, **95**, 191115 (2009).
- [100] A. Faraon, P.E. Barclay, C. Santori, K.-M.C. Fu, R.G. Beausoleil, Resonant enhancement of the zero-phonon emission from a colour centre in a diamond cavity, *Nature Photonics*, **5**, 301 (2011).
- [101] D.G. Andrew, Nanodiamonds in Fabry-Perot cavities: a route to scalable quantum computing, *New Journal of Physics*, **18**, 021002 (2016).
- [102] S. Johnson, P.R. Dolan, T. Grange, A.A.P. Trichet, G. Hornecker, Y.C. Chen, L. Weng, G.M. Hughes, A.A.R. Watt, A. Auffèves, J.M. Smith, Tunable cavity coupling of the zero phonon line of a nitrogen-vacancy defect in diamond, *New Journal of Physics*, **17**, 122003 (2015).
- [103] I. Aharonovich, J.C. Lee, A.P. Magyar, B.B. Buckley, C.G. Yale, D.D. Awschalom, E.L. Hu, Homoepitaxial Growth of Single Crystal Diamond Membranes for Quantum Information Processing, *Advanced Materials*, **24**, OP54 (2012).
- [104] J.C. Lee, A.P. Magyar, D.O. Bracher, I. Aharonovich, E.L. Hu, Fabrication of thin diamond membranes for photonic applications, *Diamond and Related Materials*, **33**, 45 (2013).
- [105] A.A. Martin, S. Randolph, A. Botman, M. Toth, I. Aharonovich, Maskless milling of diamond by a focused oxygen ion beam, *Scientific Reports*, **5**, 8958 (2015).
- [106] Delaware Diamond Knives, Inc. <http://www.ddk.com/cvd-diamond.php>
- [107] Y. Tao, C. Degen, Facile Fabrication of Single-Crystal-Diamond Nanostructures with Ultrahigh Aspect Ratio, *Advanced Materials*, **25**, 3962 (2013).
- [108] L. Li, M. Trusheim, O. Gaathon, K. Kisslinger, C.-J. Cheng, M. Lu, D. Su, X. Yao, H.-C. Huang, I. Bayn, A. Wolcott, R.M. Osgood, D. Englund, Reactive ion etching: Optimized diamond membrane fabrication for transmission electron microscopy, *Journal of Vacuum Science & Technology B*, **31**, 06FF01 (2013).

Chapter 2 Diamond device fabrication and characterisation

In order to develop diamond-based devices with specific functions that are oriented to different applications, effective methods of fabrication and characterisation for micro/nano diamond devices are needed. This chapter introduces these techniques. The main fabrication techniques developed in this work are presented in the first section. Then the methods for characterising the resulting diamond photonic devices are introduced in the second section.

2.1 Fabrication of diamond devices

The performance of diamond photonic devices for various applications is highly dependent on how these photonic devices are fabricated. In particular, the geometry of the devices, such as the radius of curvature of a diamond lens, are critical factors. In this section, we will introduce the basic processes and techniques used to achieve geometrical control in diamond photonic device fabrication.

The diamond samples used for device developments in this thesis are commercially available single crystal CVD diamond from Element Six Ltd [1]. A detailed introduction to the properties of the single crystal diamond can be found in Chapter 1. A list of the diamond sample specifications can be found in Appendix I.

A typical planar fabrication process for a diamond photonic device is shown schematically in Figure 2-1. The main steps include pattern definition via photolithography and pattern transfer via plasma dry etching. However, due to the variation of diamond device structures, additional fabrication processes and techniques are required for different devices and these will be introduced in each chapter individually. In the following sub-sections, the main techniques commonly used for the fabrication of diamond devices are overviewed.

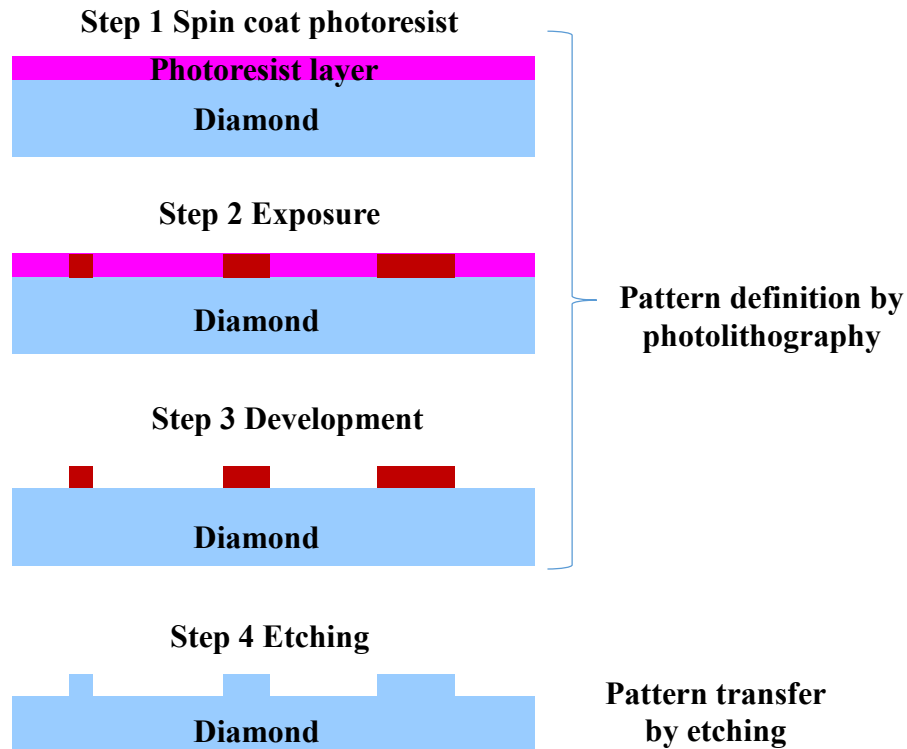


Figure 2-1: Side view schematic of the fabrication flow for diamond photonic devices.

2.1.1 Formation and definition of photoresist patterns

As illustrated in Figure 2-1, to fabricate a diamond photonic device, a proper transferrable pattern is necessary. Therefore, the pattern formation is an essential initial step. In micro-fabrication, a common and widely used technique for the pattern formation is photolithography, which has advanced greatly with the evolution of the modern semiconductor industry [2]. The photolithography technique has achieved a great success in the fabrication of large-scale integrated circuits. In the following section, photolithography is introduced, as it is the main fabrication method used in this thesis work.

2.1.1.1 Photolithography

Photolithography is a process that transfers patterns with custom-designed geometric shapes from a photomask to a thin photo-sensitive layer on a substrate [3]. In photolithography technology, a UV light beam and a photomask that has some non-transparent chrome patterns on one side of a transparent glass plate are used [4]. The light beam shines through gaps between the chrome patterns of the photomask onto a layer of a special photo-sensitive organic compound, which is named photoresist (PR),

coated on the surface of a substrate [5]. The light causes chemical reactions in the PR layer in a step named ‘exposure’. The basic process of the photolithography is shown in Figure 2-2. After exposure, the sample is dipped into a developer to remove the unwanted part of the PR and keep the desired PR patterns on the sample surface. Depending on the properties of the PR, the developed resist pattern will be either a replica of the photomask (positive resist) or a complementary pattern to the photomask (negative resist). Thus, the photolithography process contains three main steps: PR spin coating, exposure and development.

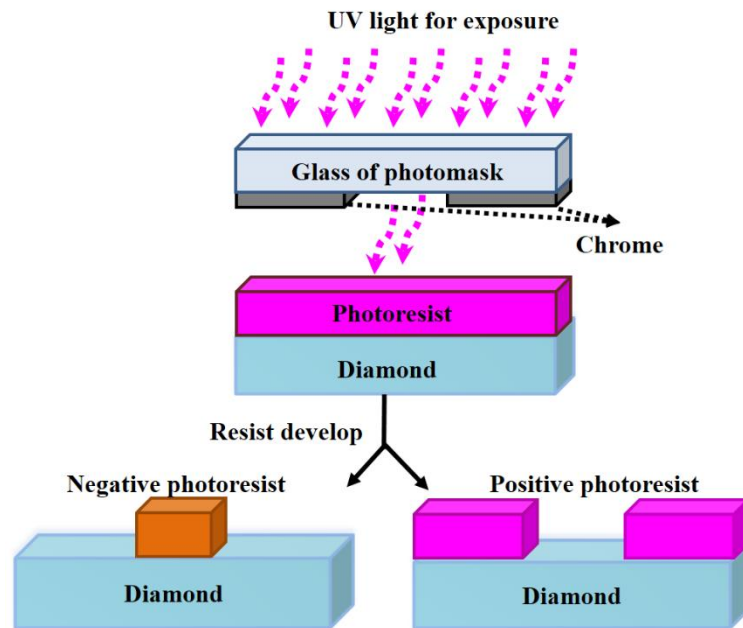


Figure 2-2: Illustration of the photolithography and the different patterns generated using positive and negative photoresists.

PR spin coating

The diamond samples are first cleaned ultrasonically in a sequence of baths of acetone, methanol and de-ionized (DI) water, each for 3 mins. After full cleaning and blow drying with a nitrogen gun, the first step of the photolithography is to spin coat a layer or layers of PR onto the surface of the sample. The PR in a liquid phase is drop-casted on the sample surface and then the sample is spun up to a certain speed to generate a spin-coated thin-layer of PR with an even thickness on the sample surface.

In this work, we use SPR 220 4.5 and SPR 220 7.0 positive PR (MEGAPOSIT® SPR 220 Series [6]) to make PR patterns. The last two digits of a PR name represent the layer thickness of that particular PR under a standard spin speed (3000 rpm), i.e.

SPR 220 7.0 means the PR layer thickness is $7.0\ \mu\text{m}$ under a standard spin speed. The inset of Figure 2-3 shows how PR was spun coated onto a diamond substrate using a spin coater. The PR spin coating is critical for forming PR patterns with a suitable thickness for further processing.

To achieve a PR layer on a substrate with a suitable thickness, different spin speeds and/or multiple PR layer method are used. The thicknesses of a single PR layer coated at different spin speeds are shown in Figure 2-3.

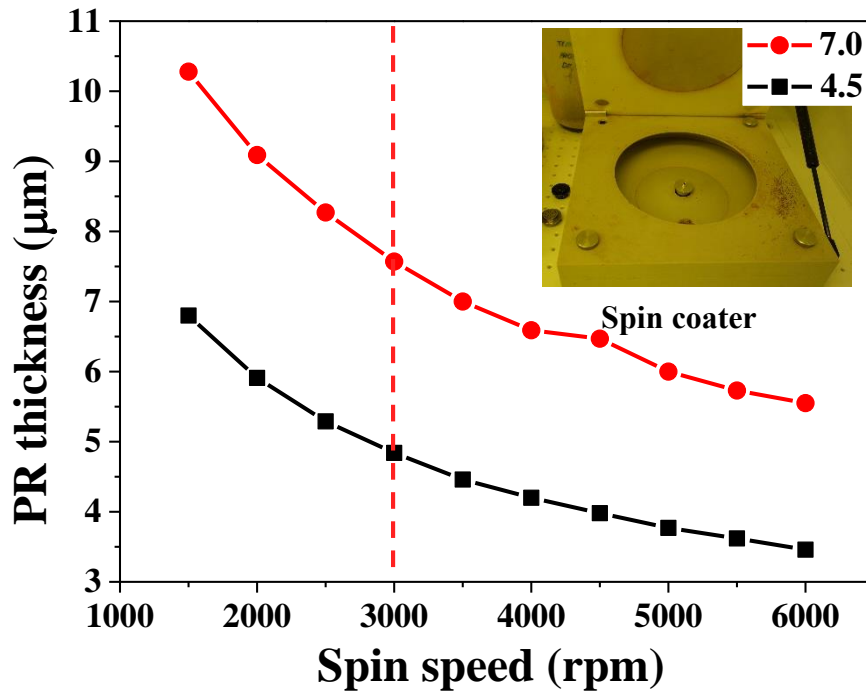


Figure 2-3: The layer thickness of the coated SPR 220 4.5 and SPR 220 7.0 on wafer substrates corresponding to certain spin speeds, data extracted from Microchem Ltd [7]. 4.5 represents SPR 220 4.5 and 7.0 represents SPR 220 7.0 in the legend, inset is a photo of the spin coater used in this thesis work. The dashed line indicates 3000 rpm.

Exposure

After spin coating to achieve a suitable PR thickness, the sample is placed on a hotplate at $90\ ^\circ\text{C}$ for 1 min to evaporate the residual solvent from the PR. This process, named soft bake, helps to increase the adhesion of the PR on the surface and prevents the PR pattern from deformation in the following steps.

The coated PR layer is then exposed to UV light through a photomask. In this work, a Karl Suss MA6 Mask Aligner is used for the exposure process. A photograph of the machine used in our lab is shown in Figure 2-4. A typical mask aligner consists of three main parts: lamp housing, microscope and alignment stage. The lamp housing,

which accommodates the exposure light source, consists of a high-pressure mercury arc lamp and the corresponding electrical circuit. It is worth noting that, in the exposure process, the sample needs to be properly aligned to locate the targeted patterns at the required position on the sample surface through the microscope. The microscope indicated in Figure 2-4 is mainly used for monitoring the alignments before the exposure. During the alignment, there is a certain gap (i.e. 50 μm , depending on individual setups) between the photomask and the sample surface, allowing the x-y and angle adjustments from the alignment stage. The wafer chuck, which holds the sample by vacuum sucking and the mask holder that holds the photomask, are also shown in the same figure.

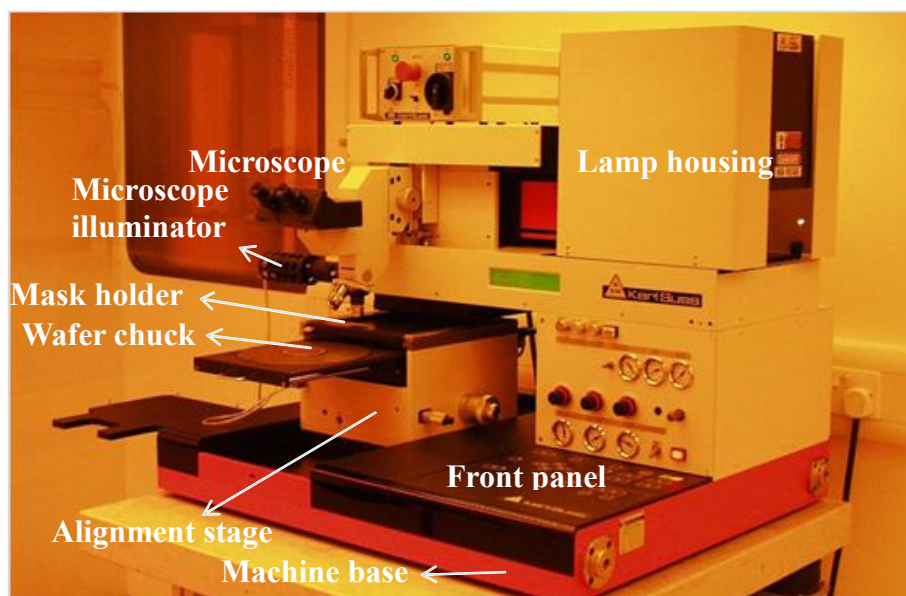


Figure 2-4: Photo of a Karl Suss MA 6 Mask Aligner used for the work in this thesis.

An important parameter for the exposure process is the contact method between mask and wafer. In the MA6 Mask Aligner, there are four modes of operation during the exposure process: the proximity exposure, the soft contact, the hard contact and the vacuum contact exposure. For the proximity exposure, a distance, the exposure gap, is left between the mask and wafer. The gap value is adjustable using the EDIT PARAMETER key at the front panel shown in Figure 2-4. The proximity exposure reduces the risk of mask damage to a minimum but the structural resolution achieved is not as high as with any contact exposure. For the soft contact exposure, mask and wafer are brought into contact. The structural resolution is better than in proximity

exposure. The vacuum securing of the wafer onto the chuck is maintained during exposure. Hard contact mode is similar to soft contact mode. After the wafer has moved into contact the vacuum underneath the wafer is switched off and nitrogen is purged under the wafer instead. So a closer contact between wafer and mask is guaranteed, even with large wafers. Vacuum contact mode achieves the highest resolution levels. After the alignment, the wafer is brought into contact with the mask. The rubber seal of a vacuum chuck creates a mini-chamber between mask and wafer. This chamber is evacuated in steps. A pre-vacuum gently pulls gas out of the mini-chamber to enable a smooth contact between mask and wafer, which helps to prevent gas bubbles being trapped in between. Full vacuum is then applied as the next step. The wafer is loaded in the closest contact position and the best contact between mask and wafer is achieved. After the exposure, nitrogen is purged into the mini-chamber to break the vacuum. The larger the wafer, the longer the vacuum and purge times. In this thesis work, the hard contact mode is used as a trade-off between the risk of mask damage and achieving high resolution [8].

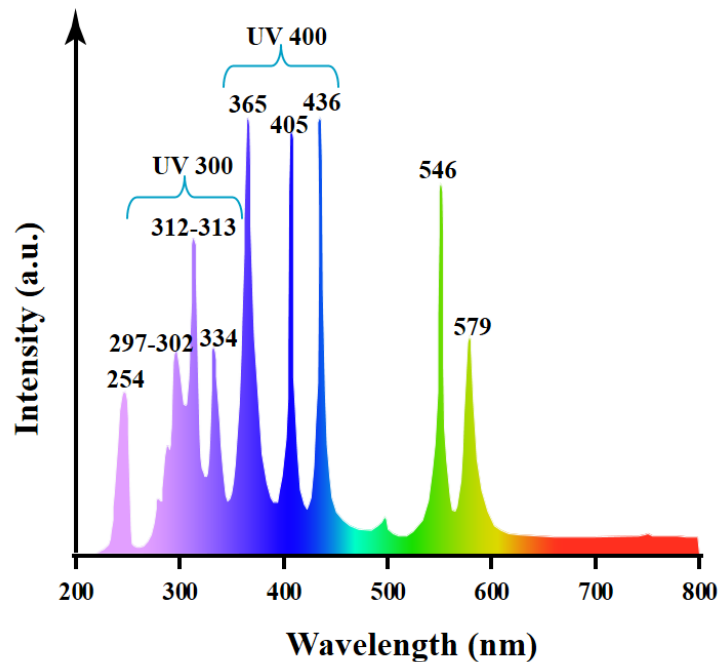


Figure 2-5: Spectrum of the UV light source used for the exposure in this thesis, data extracted from [9].

The lamp housing model used in our MA6 mask aligner is UV400, which consists of an HBO[®] 350 W/S high-pressure short-arc mercury lamp. HBO is a short name resulting from a Germany system of nomenclature, where ‘H’ represents ‘Hg

(Mercury)', 'B' represents 'quartz short-arc' and 'O' means 'optical projection'. The emission wavelengths of this lamp are mainly in the range between 350 nm and 450 nm. Figure 2-5 is a typical emission spectrum of this high-pressure short-arc mercury lamp.

The photolithography pattern resolution is determined by the wavelength of the exposure light source and the numerical aperture of the optical system. Generally, the ideal resolution (R) and depth of focus (DOF) of an optical system with a numerical aperture (NA) are determined by the Rayleigh criterion as [10]:

$$R = k_1 \frac{\lambda}{NA} \quad (2-1)$$

$$DOF = k_2 \frac{\lambda}{(NA)^2} \quad (2-2)$$

When the NA is high enough (> 0.8), DOF can be calculated as [11]:

$$DOF = k_3 \frac{\lambda}{2(1-\sqrt{1-(NA)^2})} \quad (2-3)$$

where the numerical aperture $NA = n \sin \theta$ and the factors k_1 (a dimensionless scaling parameter), k_2 and k_3 (dimensionless factors of order unity which depends on the imaging details) are process-dependent constants. In order to decrease the feature size and thus increase the pattern resolution, we need to reduce the wavelength and increase the numerical aperture as can be seen from the above equations. Table 2-1 shows the wavelengths of some light sources for optical lithography and the corresponding pattern resolution and DOF calculated using Equation (2-1) to (2-3).

Table 2-1: Wavelengths of light sources for optical lithography and the corresponding resolution (R) and depth of focus (DOF). $k_1=0.3$ and $k_3=1$ for R and DOF calculations. Assuming $NA=0.9$ for all wavelengths except extreme ultraviolet (EUV), for which $NA=0.25$ [11].

Light source	$\lambda(nm)$	R (nm)	DOF (nm)
Hg arc lamp (g-line)	436	145	386
Hg arc lamp (i-line)	365	122	324
KrF	248.3	83	220
ArF	193.4	64	171
F ₂	157.6	53	140
EUV	13.5	16	213

The light sources used for high-resolution optical lithography have evolved from the Hg arc lamp (typical wavelengths: 436 and 365 nm) to an excimer laser (typical wavelength 193 nm) [12]. From the above, with our system, we can expect R of ~150 nm and DOF of ~350 nm.

Pattern development

After exposure, the sample is placed into the developer solution for a required time. The developer reacts with the exposed PR and dissolves the unwanted parts of the PR layer. The developer for all positive resists used in this thesis work is the same (MicroDev from Microchem [13]). When fully developed, the sample is rinsed under running DI water and then a nitrogen gun is used to blow dry the sample. The sample is then inspected under a microscope.

2.1.2 Pattern transfer

In microfabrication, the patterns are normally made in PR first. These PR patterns can be transferred to the sample substrates by different techniques. To transfer the PR pattern to diamonds to make diamond structures, plasma dry etching is used due to the extreme hardness and the chemical inertness of diamond. The dry etching technique is introduced in detail as follows.

2.1.2.1 Dry etching

As briefly introduced in Chapter 1, dry etching uses reactive gaseous etchants and plasma to remove parts of the material from the exposed surface of the sample. This is schematically shown in Figure 2-6. The plasma, which is an ionised gas produced by applying RF excitation to neutral gas under specific conditions, generates an equal number of free positive and negative ions with high chemical activities [14]. These ions can react with the etched material at the sample surface, hence achieving chemical etching. In addition, plasma etching includes physical ion bombardment at the sample surface, which may change the chemical properties of the material and accelerate the overall etching process accordingly. Dry etching normally produces anisotropic etching profiles to form structures with small features that require high etching accuracy. There are two main categories of dry etching tools used for this work: reactive ion etching (RIE) and inductively coupled plasma (ICP) etching systems.

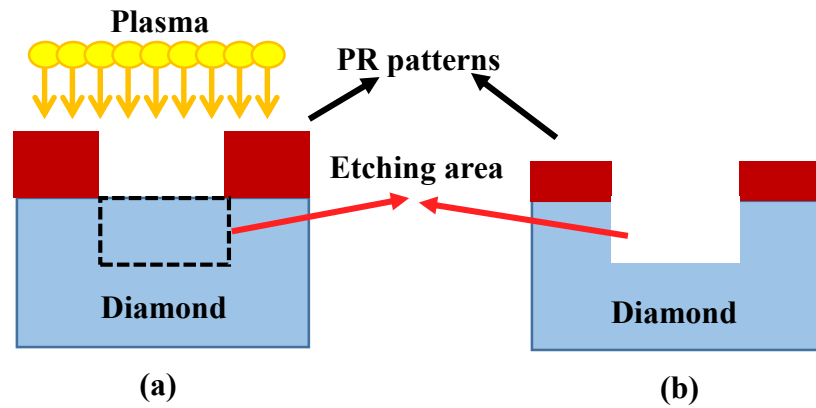


Figure 2-6: Side view schematic of the dry etching process, the exposed part that will be etched away is labelled with a black dashed-rectangle.

Plasma etching tools

a) Reactive ion etching (RIE)

An Oxford PlasmaLab 80 Plus RIE System [15] is used for RIE etching in this work. Figure 2-7 (a) shows this RIE facility and Figure 2-7 (b) shows a schematic diagram of the RIE chamber. In the RIE system, the etching parameters including the gas flows, the gas pressure and the radio frequency (RF) power can be adjusted for different etching processes. The etching is performed with plasma induced by an RF source at 13.56 MHz. The applicable RF power ranges from 30 to 1000 W. The typical process gas pressure in the chamber is between 5 and 150 mtorr and plasma density is about $1-5 \times 10^9/\text{cm}^3$. During the process, a DC bias is generated between the electrodes. The DC bias and the gas pressure determine the generated the energy of ions at the surface of the sample, which further determines the etching rate (a quantitative evaluation of the etching speed).

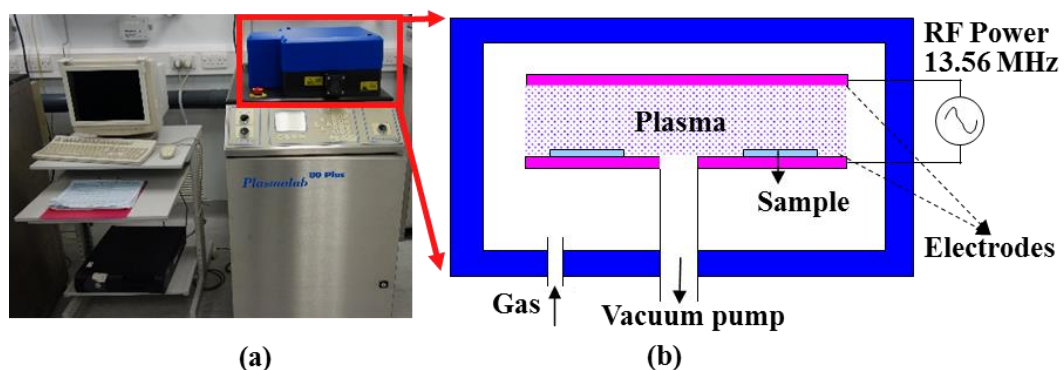


Figure 2-7: (a) Photo of the RIE facility and (b) the schematic of the RIE chamber.

b) Inductively coupled plasma (ICP) etching

In this work, the fabrication of the diamond devices was carried out by using a multiplex ICP etch tool (Surface Technology Systems, now SPTS [14]). A photograph and a schematic of this ICP etching tool are shown in Figure 2-8 (a) and (b), respectively. An ICP is similar to an RIE but with an additional inductive coil to enhance the plasma density. Compared to the plasma generated in an RIE system, the plasma density in ICP is therefore much higher, which increases the etching rate significantly. In ICP, the plasma density is controlled by the coil power, while the ion energy is determined by platen power.

For the diamond device fabrication, Ar/O₂ or Ar/Cl₂ plasmas are commonly used. During the process, a typical ICP gas pressure is between 1 to 100 mtorr with a plasma density about $5 \times 10^{11}/\text{cm}^3$. The ICP etching parameters such as the gas flow, the gas pressure, the coil power and the platen powers can be adjusted separately for different ICP etching processes. The detail of the parameters used will be introduced in the later subsection.

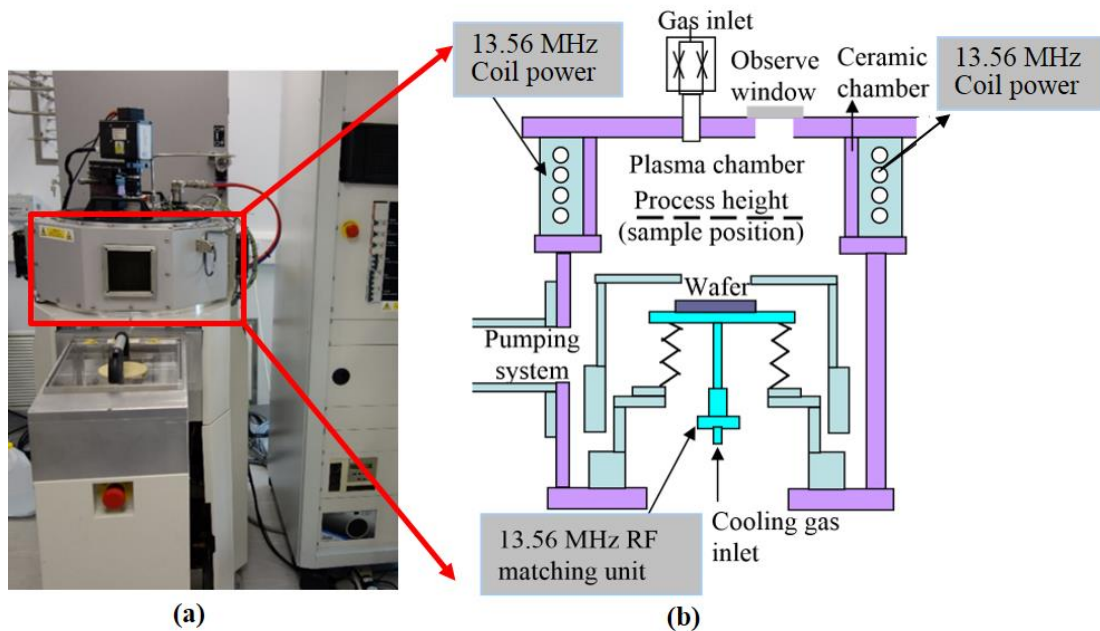


Figure 2-8: (a) Photograph of the ICP system and (b) the schematic diagram of the ICP chamber indicated by a red rectangle in (a).

General plasma etching mechanisms

As mentioned above, there are two main mechanisms in plasma dry etching, namely, the physical ion bombardment and the pure chemical etching. The physical

ion bombardment, as shown in Figure 2-9 (a), uses high-energy ions to remove the material from the sample surface directly. The etching rate is highly dependent on the flux and energy of the applied ions.

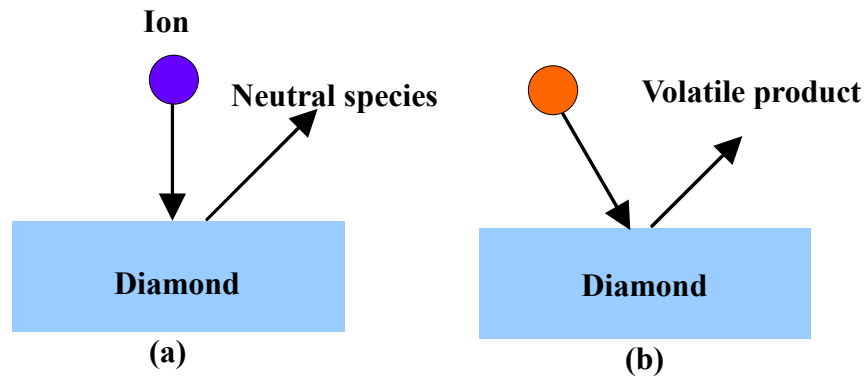


Figure 2-9: Schematics of the two basic plasma etching mechanisms: (a) physical ion bombardment and (b) chemical etching.

Chemical etching uses gaseous etchants to form easily-removable volatile by-products on the sample surface through chemical reactions. The etching rate of pure chemical etching is highly correlated with the particular chemical reaction that occurs on the exposed sample surface between the gaseous etchants and the etched material. It is essential that the etching products are volatile otherwise non-volatile products would coat the sample surface and no further etching would then be possible. It is worth noting that pure chemical etching is usually isotropic.

Plasma etching parameters

A plasma is usually characterised by a set of fundamental parameters such as the electron number density and the electron temperature. However, these parameters are not generally useful in the semiconductor industry for many reasons [16]. The commonly used instrumental parameters include the reactor pressure, the RF frequency and power, the sample process temperature, the gas flow rate, the feed gas composition, the reactor geometry and materials. These parameters are measurable and thus are used to define the plasma etching process.

In ICP, the main adjustable parameters are the coil power and the platen power. The coil power controls the plasma density. The platen power determines the ion energy, which accelerates the ions towards the etching surface. If the platen power is too high, undesirable surface damage and mask erosions can occur.

The unit of gas flow rate is standard cubic centimetres per minute (sccm). The gas flow should be large enough to feed in enough etchant species.

Diamond dry etch recipes

Two etch recipes were used for diamond etching in this thesis work: Ar/Cl₂ and Ar/O₂. The chemical etching mechanism of the diamond with Ar/Cl₂ plasma is [17]:



For the physical etching, Ar ions bombard diamond and dislodge the carbon atoms out of the diamond surface. This process also enhances the chemical reaction between the chlorine and carbon ions to form the etch products of CCl_x. The volatile etch product, CCl_x, is then pumped out from ICP chamber. The Ar/Cl₂ etching recipe normally gives a smooth etched surface [9] and is used for fabricating high quality diamond photonic devices. This recipe is also used when a low selectivity (etch rate of diamond/ etch rate of photoresist) is needed.

The Ar/O₂ etching process is similar [18]. The ion-enhanced chemical etching mechanism is:



The optimised etching recipes for diamond of these two processes are shown in Table 2-2 and Table 2-3, respectively. The Ar/O₂ is normally used to pursue a higher etch rate where the surface roughness is less concerned.

Table 2-2: Ar/Cl₂ ICP etching recipe for diamond photonic device fabrication.

Pressure	Ar flow	Cl ₂ flow	Platen power	Coil power	Photoresist etching rate	diamond etching rate	Selectivity
5 mTorr	25 sccm	40 sccm	300W	400W	750nm/min	75nm/min	0.1

Table 2-3: Ar/O₂ ICP etching recipe for diamond photonic device fabrication.

Pressure	Ar flow	O ₂ flow	Platen power	Coil power	Photoresist etching rate	diamond etching rate	Selectivity

5 mTorr	15 sccm	40 sccm	300W	800W	1375nm/min	220nm/min	0.16
---------	------------	------------	------	------	------------	-----------	------

2.1.2.2 Wet etching

Wet etching is a process used to remove material from a substrate chemically. It usually occurs at a liquid-solid interface through chemical reaction universally or selectively. There are several wet etching processes used in this work, such as immersion etching of PR in acetone and SiO₂ etching in buffered oxide etch (BOE). All wet etching works are carried out in a wet bench as shown in Figure 2-10.



Figure 2-10: Photograph of the wet bench in our cleanroom.

Resist removal

It is quite often necessary to remove PR from the substrate for the subsequent process or to restart the process. This can be done by immersing the sample in a glass beaker containing acetone. Non-crosslinked PR is usually quite easily removed. However, acetone has a high vapour pressure which can cause re-deposition of stripped PR onto the substrate because of its fast drying. So a methanol rinse is normally used after acetone immersion to produce a residue-free surface. Alternatively, an acid etching using Piranha mixture (as will be introduced in Chapter 5) can be used to remove stubborn organic residues.

SiO₂ etching

SiO₂ has regularly been used as a hard mask for diamond etching due to the higher etching selectivity it offers (defined as the ratio between the etch rates in the diamond and the PR). Such a SiO₂ hard mask can be removed by wet chemical etching and

almost all wet etching of SiO₂ is done with hydrofluoric (HF) acid solution. The etching chemistry can be described by the following chemical reaction:



The SiO₂ etching rate is very high using pure HF solution. In our laboratory, SiO₂ etching is done by BOE which is a buffered HF solution with mixed ammonium fluoride (NH₄F) (HF: NH₄F= 1:7). Using BOE has the advantage of a controllable etching rate which is about 100 nm/min for plasma-enhanced chemical vapour deposition (PECVD) SiO₂. As HF reacts with SiO₂ which is the main ingredient of glass, a plastic beaker is used for BOE or any HF solution.

2.2 Characterisation methods for diamond photonic devices

In order to characterise the diamond photonic structures and devices developed, some advanced characterisation techniques are required. These techniques provide information including profiles, surface roughnesses and optical performance of the diamond devices. In this work, a stylus surface profilometer and an optical profiler are used for the profile measurements (Chapter 3), and an atomic force microscope (AFM) is used for both local topography measurement and surface roughness measurement (Chapter 4, 5). Their relative resolutions are shown in Table 2-4. A knife-edge technique is used to measure the focal length of the diamond lenses developed for diamond Raman lasers (Chapter 4) and a scanning confocal microscope is used to measure the photoluminescence (PL) of the emission from the defect centres in the diamond membrane (Chapter 5). These techniques used are introduced in the following subsections.

2.2.1 Profile characterisation

For a fabricated structure, its geometry is usually the first thing one wants to know. For geometry measurements, the facilities used in this work include: a Dektak 3 surface profilometer, a Wyko NT1100 optical profiler and an AFM.

2.2.1.1 Dektak surface profilometer

A Dektak 3 surface profilometer, a measuring instrument used to measure a surface's profile, was used for pattern profile measurements. In this tool, a diamond stylus is moved vertically in contact with a sample and then moved laterally across the

sample for a specified distance and specified contact force. This profilometer can measure small surface variations in vertical stylus displacement as a function of position. The height position of the diamond stylus generates an analog signal which is converted into a digital signal, stored, analysed, and displayed [19].

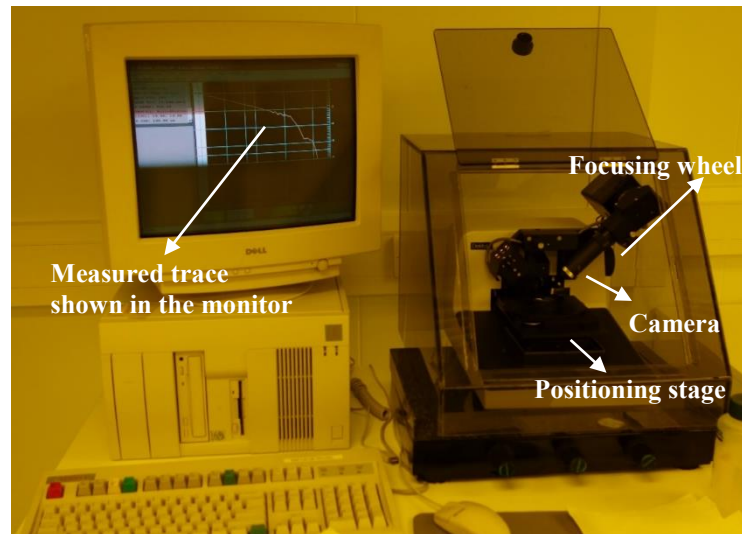


Figure 2-11: Photograph of the Dektak 3 surface profilometer used in this thesis.

Before the measurement, the sample is placed on an adjustable stage. After focusing, the stylus position is aligned to a cross hair shown on the screen. This cross hair can be used to indicate the start point of the measurement. The sample can be adjusted to be right below the stylus by using the positioning stage as shown in Figure 2-11. After the alignment, the stylus tower is lowered to approach the sample surface. By moving the sample along a line toward one direction and recording the height at each lateral point, a line profile can be obtained. During the measurement, the occurring measured trace is displayed on the monitor as shown in Figure 2-11. The measured 2D profile data can be exported for further analysis.

Our Dektak 3 profilometer can measure lateral lengths ranging from 50 μm to 50 mm and vertical heights from 10 nm to 131 μm with a preset measurement length each time. The resolutions of the lateral and vertical measurements are 2.5 μm and 1 nm, respectively. The resolutions are limited by the radius of the stylus and the scan speed each time. This tool is critical for the measurements of the formed PR bulge profiles reported in Chapter 3. Such a PR bulge profile measured by the Dektak surface profilometer is shown in Figure 2-12.

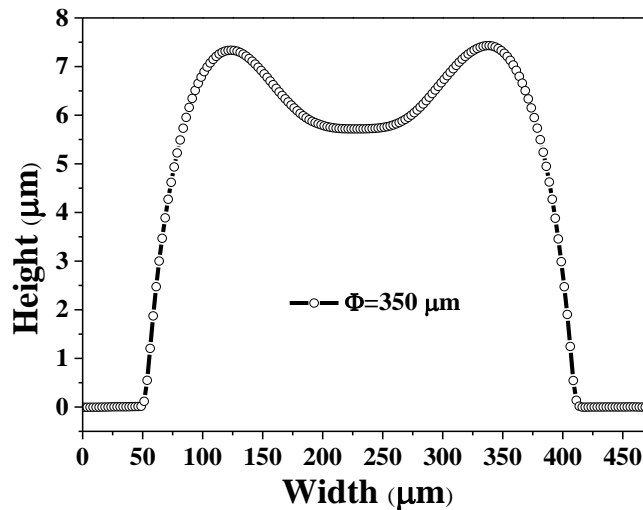


Figure 2-12: A representative PR bulge profile measured by the Dektak 3 surface profilometer. Φ is the measured diameter.

2.2.1.2 Optical profiler

An interferometer (a Mirau Interferometer here for example [20]) is a system where a beam of light is split and one beam is reflected from the object under test and the other is reflected from a reference mirror [20]. The beams are then recombined to create bright and dark bands called “fringes” that make up an interferogram. Fringes, like lines on a topographic map, represent the topography of the object. In an optical profiler, a CCD detector is used to register the interferogram and forward it to a computer for processing using interferometric phase-mapping programs. The detail of the principle of this optical profiling approach can be found in [20].

For characterising ultrathin diamond membranes which will be reported in Chapter 5, noncontact measurements are critically important for avoiding possible damage. In this work, a noncontact Veeco Optical Profiling System (Wyko NT 1100, Veeco Ltd., now Bruker Ltd.) was used to characterise the ultrathin diamond membranes. A photograph of this system is shown in Figure 2-13 (a). A schematic of this optical profiler is shown in Figure 2-13 (b). Detailed descriptions of this setup can be found in [21].

This optical profiler can provide accurate surface topography, sub-nanometre vertical resolution, ability to stitch large area measurements using a motorised stage and a complete modelling of the surface profiles in 3D using the analysis software.

There are two modes available in this setup: vertical scanning interferometry (VSI) and phase shift interferometry (PSI). In general, the VSI is used for measuring the

surface with feature size larger than one-quarter of the source wavelength (~ 150 nm) or samples with a rough surface. The PSI is used for measuring the smooth surface and small vertical thickness. In our measurements, the VSI mode is used to measure the thickness of the diamond membranes. The lateral resolution of an interferometer is determined by its optical system and the wavelength of the light source. The lateral resolution of this Wyko NT1100 optical profiler is smaller than 300 nm.

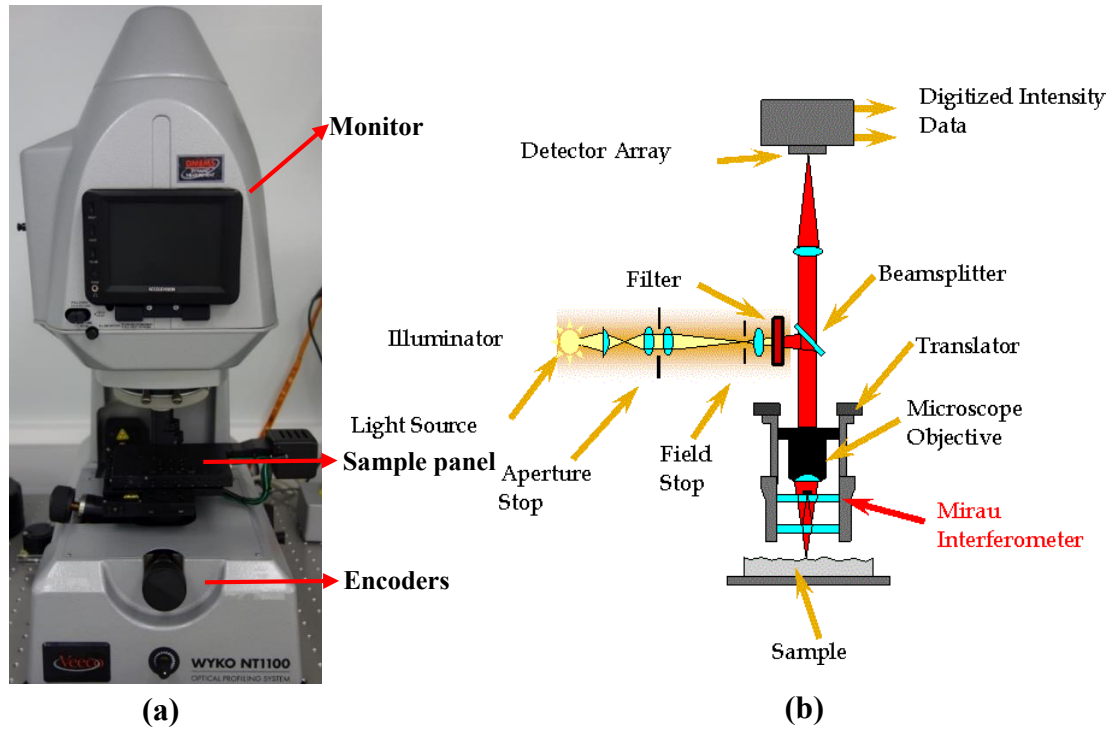


Figure 2-13: (a) Photograph of the optical profiler and (b) the schematic diagram of this optical profiler [21]. The optical filter removes all but the red light from the white light of the halogen lamp.

A typical result measured using the optical profiler is shown in Figure 2-14, which demonstrates the topography (red area indicated as diamond platelet) and 3D reconstruction of the diamond sample sitting on the Si substrate (blue) for an overall area of $640 \times 480 \mu\text{m}^2$. The surface information of the diamond sample: the surface roughness (shown as R_a and R_q at the left of the 3D image) and the thickness of the diamond platelet is reflected in the image. The colour bar (as shown at the right side of the 3D image) represents the thickness information which gives a direct information of the thickness variation across the sample surface in reference to the Si substrate.

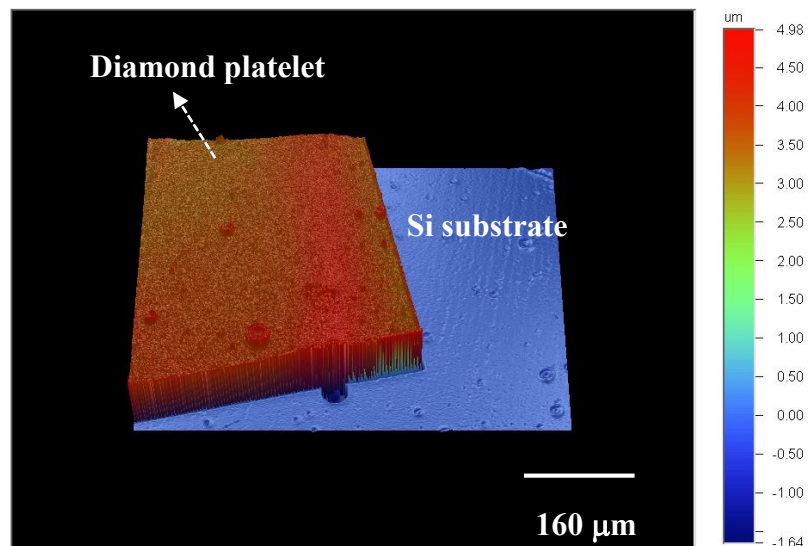


Figure 2-14: Typical measurement result from the Optical Profiler using VSI mode demonstrating a 3D reconstructed topography of a diamond sample sitting on a Si substrate. The measurement is carried out on an ICP etched diamond platelet from Element Six with a thickness around $6\ \mu\text{m}$. The measured area is $640 \times 480\ \mu\text{m}^2$.

2.2.1.3 Atomic force microscopy

The AFM is used in this work for high accuracy surface topography measurements including surface roughness characterisation. For optical applications, a smooth surface of an optical component with root-mean-square roughnesses below $1\ \text{nm}$ may be required which is beneficial for reducing the scattering loss at the surface. AFM is a powerful tool for providing such high accuracy information.

In this work, a non-contact mode AFM (Park system Ltd., XE100 [22]) as shown in Figure 2-15, was used. AFM is based on the atomic force between atoms from a sharp tip (normally $12\ \text{nm}$ in radius) on a cantilever and the surface of the sample. An AFM images the topography of a sample surface by scanning the cantilever over a region of interest. In non-contact mode AFM, a piezoelectric modulator deliberately vibrates a cantilever with very small amplitude at a fixed frequency. This frequency is near the intrinsic resonance of the cantilever. As the tip approaches a sample, the van der Waals attractive force between the tip and the sample acts upon the cantilever and causes changes. The changes caused by the raised and lowered features on the sample surface influence both the amplitude and the phase of the cantilever vibration. These vibration changes are monitored by using a laser beam reflected to the position-sensitive photo diodes (PSPDs). By using a Z-Servo system feedback loop to control the height of the tip above the surface, thus maintaining constant laser position, the

AFM can generate an accurate topographic map of the surface features [23]. An ultimate resolution of atomic lattice is achievable and the spatial resolutions is limited by the radius of the AFM tip (typically 2~5 nm) [22]. The measurement principle of the AFM is schematically shown in Figure 2-16.

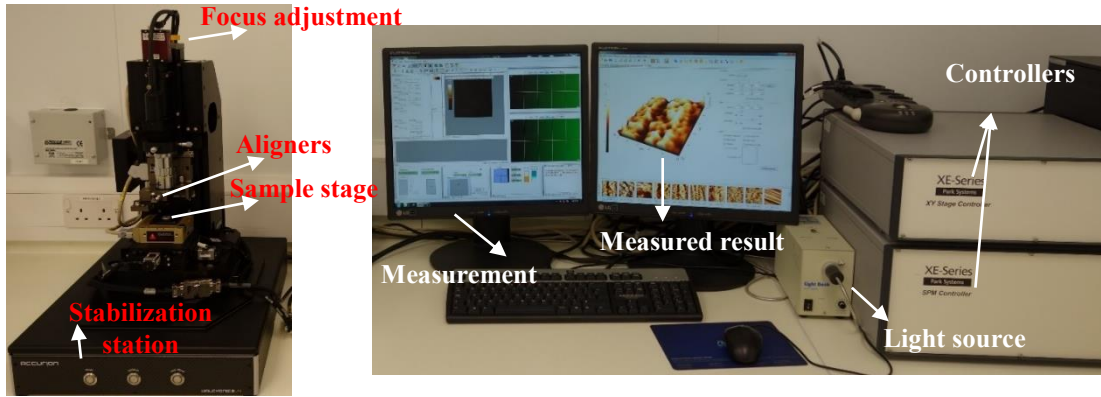


Figure 2-15: Photos of the AFM system used in this thesis work.

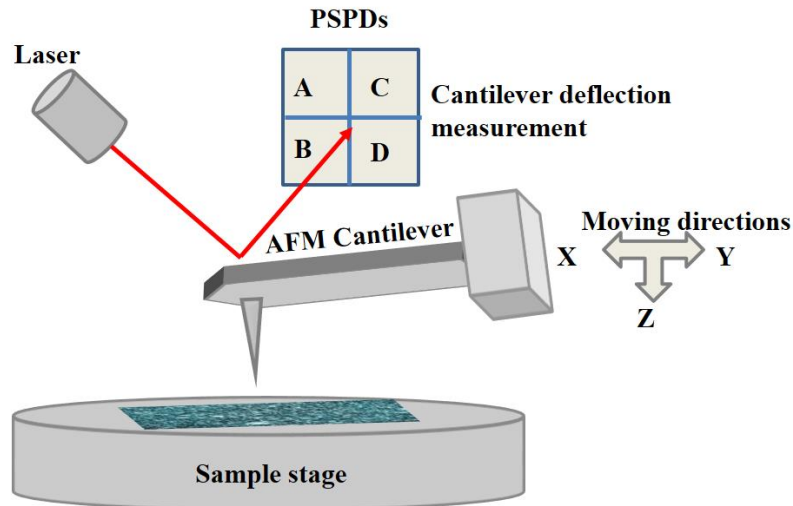


Figure 2-16: Schematic of the principle of the AFM measurement.

A comparison of the above profile measurement tool is summarised in Table 2-4.

Table 2-4: Comparison of the profile measurement tools.

Equipment	Resolutions and determined factors	Comments
Dektak profiler	The resolutions of the lateral and vertical measurements are 2.5 μm	Measure range: lateral lengths ranged from 50 μm to 50 mm and vertical

	and 1 nm, respectively. The resolutions are limited by the radius of the stylus and the scan speed (scan length/collected data points) each time.	heights from 10 nm to 131 μm . Used for measurements of large sized patterns (mm scale).
Optical profiler (Wyko NT1100)	The lateral resolution of this optical profiler is smaller than 300 nm, limited by the wavelength of the laser beam source.	Measure range: Vertical: 0.1nm to 1mm, Lateral: 0.08 to 13.1 μm . Used for measuring the transparent samples such as the diamond membrane.
AFM	Resolutions: 0.76 \AA (lateral) and 0.25 \AA (vertical), limited by the Set point and intrinsically the tip radius (2-5 nm).	Measure range: lateral up to 50 μm , vertical: up to 3 μm . Used to measure local area of sample surface with high precision, e.g. the edge thickness of the diamond membrane.

2.2.2 Optical characterisation

To fully characterise the performance of the diamond photonic devices, further optical measurements are needed. In this work, two optical characterisation methods are used: the focal length measurement of the diamond micro-lenses developed and introduced in Chapter 4 and the PL characterisation of the NV centres in the diamond membranes developed and presented in Chapter 5.

2.2.2.1 Focal length measurements

The focal length of an optical lens is an important parameter for its application. In this work, the focal length of convex diamond micro-lenses is measured by using a knife-edge technique. A schematic of this technique is shown in Figure 2-17 (a).

In this measurement, a collimated beam from a He-Ne laser passes through the diamond micro-lens as shown in Figure 2-17 (a). The propagation beam profile after the micro-lens is schematically shown in Figure 2-17 (b). As can be seen, the propagation beam has a minimum beam diameter at the focal point. The beam diameter varies at different Z position along the direction of propagation. At each Z position, the beam has a 2D Gaussian profile as shown in Figure 2-17 (c). During the experiment, the beam intensity is recorded as a knife-edge is translated through the beam using a calibrated translation stage. A fixed CCD photodetector records the integral of the Gaussian beam between $-\infty$ and the position of the knife. The measured beam intensity along the Y position of each Gaussian profile is fitted to a theoretical Gaussian beam function. Based on the fitted results, the beam diameters of these Gaussian profiles can be calculated.

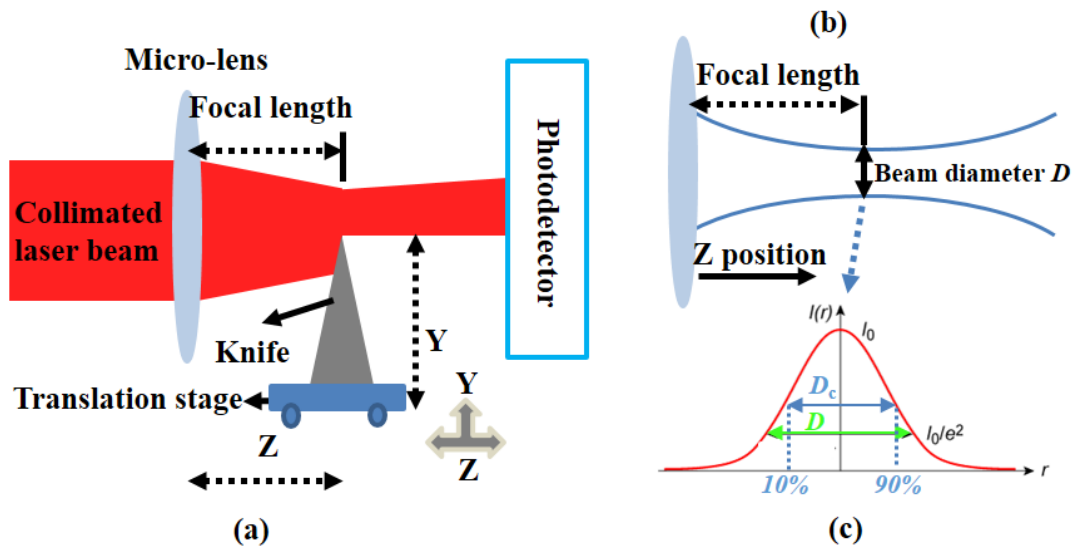


Figure 2-17: (a) Schematic of the knife-edge technique used for the focal length measurement and (b) the converged propagation beam profile and (c) the Gaussian profile demonstrating the beam diameter D (green) and the clip width D_c (blue) at each Z position, the beam diameter being indicated with green arrow [24].

Taking a full set of knife-edge measurements and fitting as above can be tedious and time consuming. It is quicker to use the 10%-90% method outlined below. Firstly, the fully exposed intensity of the beam is measured. Then, the knife-edge is translated across the beam. The distance between the Y positions at which the beam intensity is 10% and 90% of the full value, respectively, is recorded [25]. The distance between the two recorded Y positions, the clip width D_c , is used to evaluate the beam diameters

as shown in Figure 2-17 (c). The beam diameter can be calculated using the following equation [26]:

$$D = \frac{4 \times D_c}{2.56} = 1.561 D_c \quad (2-7)$$

where D denotes the beam diameter at each Z position, and D_c denotes the measured clip width recorded using the clip level of 10-90%. By measuring D at each Z position, the beam diameter as a function of the distance to the micro-lens can be fitted. The propagation beam as shown in Figure 2-17 (b) can be obtained based on the fitted result. The focal length of the measured micro-lens is the distance at which D reaches the minimum. The measured results of the diamond micro-lenses using this knife-edge technique will be reported in Chapter 4.

2.2.2.2 Photoluminescence

Photoluminescence (PL) is a form of luminescence in which photons are emitted from a luminescent material excited by an external light source. PL may provide useful information on such as crystal vibrations and radiative transitions and is also a common technique used to measure the purity and crystal quality of semiconductors. In this work, PL is used to characterise the spontaneous emission from defect centres, in particular NV centres in diamond membranes.

There are many variations of PL systems used to measure different properties of materials. In this work, a home-built scanning confocal microscope, as shown in Figure 2-18 (a), was used to measure the PL of defect centres [27]. This scanning confocal microscope was built by the Photonic Nanomaterials Group, Department of Materials, University of Oxford. In this confocal microscope, a laser source at 532 nm is used to excite a diamond sample and then the PL emissions, from the defect centres, are measured. In this setup, the sample temperature can be cooled down to 15 K by using a liquid nitrogen bath cryostat. This low-temperature cryostat is used to suppress the background noise. Figure 2-18 (b) shows the schematic of the experimental setup.

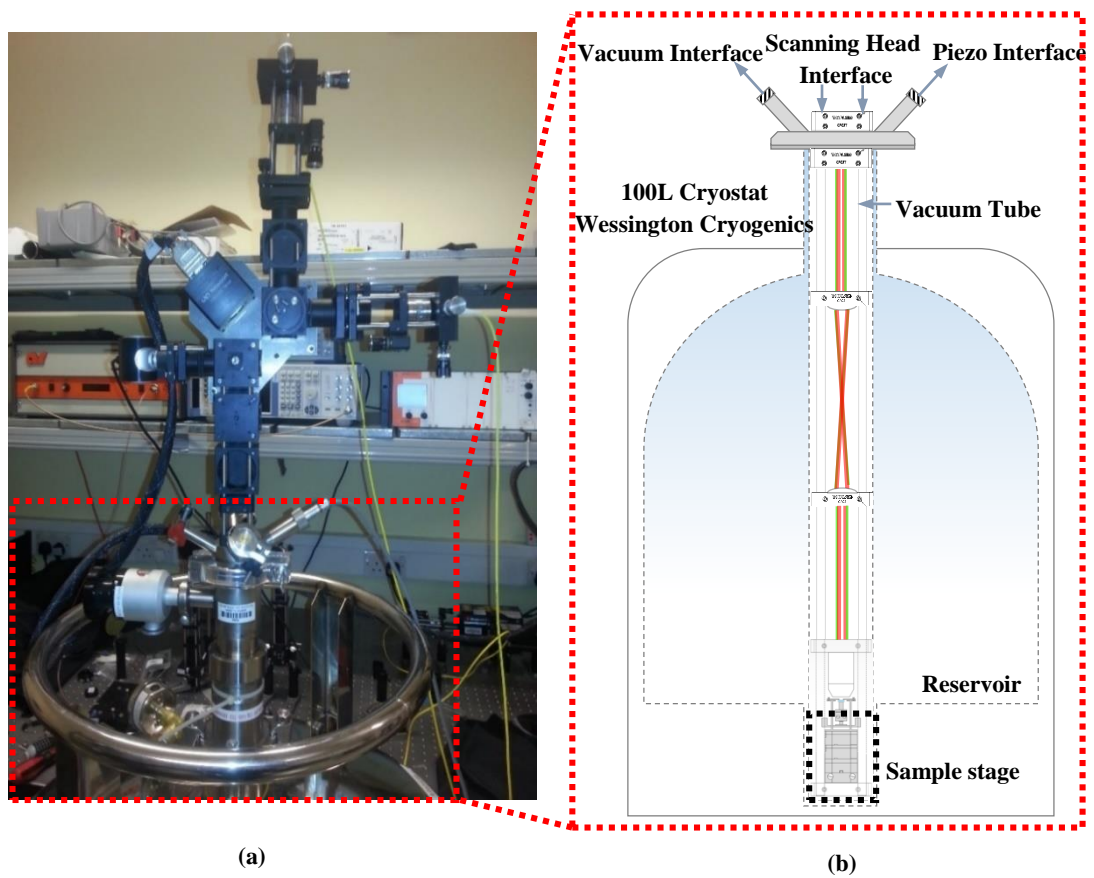


Figure 2-18: (a) Photograph of the home-built scanning confocal microscope setup used in this work and (b) the schematic diagram of the low-temperature cryostat. Image courtesy: Photonic Nanomaterials Group, University of Oxford.

A more detailed schematic of the scanning confocal microscope is shown in Figure 2-19. Excitation light (a 532 nm green laser) is reflected by a dichroic beam splitter scanned with a fast steering mirror (Newport FSM300), which provides 10 rad pointing precision in tip and tilt within a single compact unit. The excitation light was then focused on the sample using a low-magnification objective lens (20 \times , NA = 0.45). The PL from the sample was collected by the same objective lens and guided to a spectrometer (Acton SP500i) with a liquid nitrogen-cooled CCD detector (Princeton Spec10). There is a long pass filter in front of the spectrometer to prevent the excitation light being detected by the CCD, which is used to image the sample with the purpose of controlling the excitation position at the sample surface. The long pass filter is an optical component with nearly 100% transparency for a specific long-wavelength (compared with the wavelength of the excitation light) range. Two telecentric lenses are situated in the vacuum tube so that the light is collimated when it passes through the tube window. The diameters of these telecentric lenses determine the field of view.

The two telecentric lenses in this setup provide approximately 50 mrad of range in the beam angle at the objective. Both excitation (green line) and collection (red line) are fibre coupled using the single mode fibre (yellow), with the collimated paths coinciding at a beam-splitter.

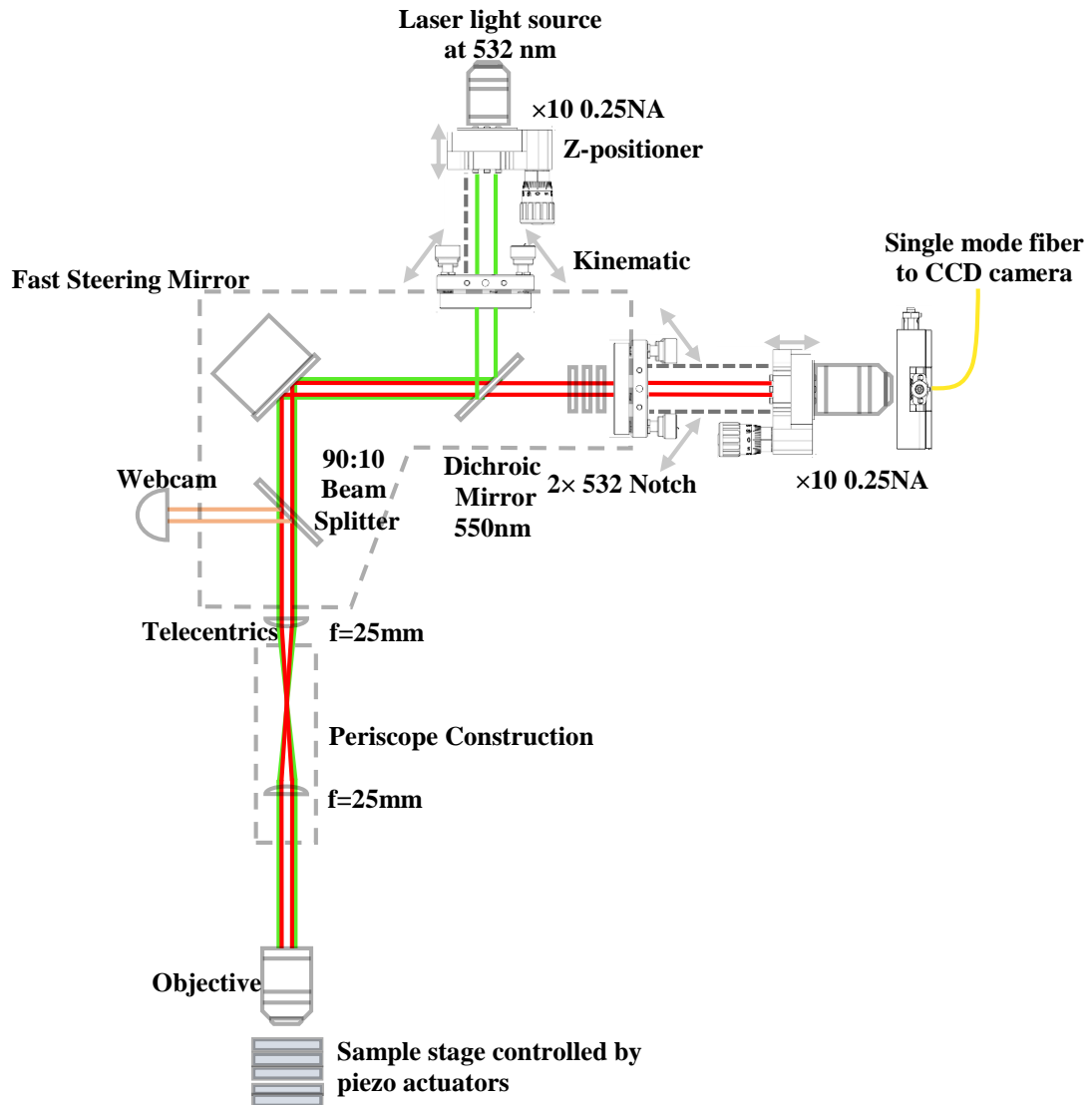


Figure 2-19: Schematic of the scanning confocal microscope experimental setup. Image courtesy: Photonic Nanomaterials Group, University of Oxford.

2.3 Conclusion

In this chapter, the general micro-fabrication facilities, their principles and fabrication processes including photolithography and plasma dry etching have been introduced. The characterisation methods for the photonic devices developed based on these fabrication techniques were also described. These fabrication techniques and

characterisation methods will be applied to fabricate and characterise the diamond photonic devices as described in the later chapters.

References

- [1] Element Six Ltd. http://www.e6.com/wps/wcm/connect/e6_content_en/home
- [2] K.A. Jackson, W. Schröter, Handbook of Semiconductor Technology: Processing of semiconductors, Wiley-VCH, (2000).
- [3] S.M. Sze, M.K. Lee, Semiconductor Devices: Physics and Technology, 3rd Edition: Physics and Technology, John Wiley & Sons, (2012).
- [4] S. Rizvi, Handbook of Photomask Manufacturing Technology, CRC Press, (2005).
- [5] C. Mack, Fundamental Principles of Optical Lithography: The Science of Microfabrication, Wiley, (2008).
- [6] MEGAPOSIT® SPR 220 Series:
<http://micromaterialstech.com/products/gi-line-broadband-photoresists/dow-spr220-series-photoresists/>
- [7] MEGAPOSIT® SPR photoresist data:
http://www.microchem.com/PDFs_Dow/SPR%20220%20DATA%20SHEET%20R%26H.pdf
- [8] MA6 Mask Aligner: <https://www.suss.com/en/products-solutions/products/mask-aligner/maba6/details.html>
- [9] Y. Zhang, Diamond and GaN Waveguides and Microstructures for Integrated Quantum Photonics, PhD thesis, University of Strathclyde, (2012).
- [10] M.J. Madou, Manufacturing Techniques for Microfabrication and Nanotechnology, CRC Press, (2011).
- [11] T.A. Brunner, Why optical lithography will live forever, Journal of Vacuum Science & Technology B, **21**, 2632 (2003).
- [12] P. Naulleau, C.N. Anderson, L.-M. Baclea-An, P. Denham, S. George, K.A. Goldberg, G. Jones, B. McClinton, R. Miyakawa, I. Mochi, 27th European Mask and Lithography Conference, International Society for Optics and Photonics, 798509 (2011).
- [13] MicroDev from Microchem: <http://www.microchem.com/>
- [14] H. Conrads, M. Schmidt, Plasma generation and plasma sources, Plasma Sources Science and Technology, **9**, 441 (2000).
- [15] Oxford PlasmaLab 80 Plus RIE System: <http://www.oxford-instruments.com/products>
- [16] S.J. Moss, A. Ledwith, Chemistry of the Semiconductor Industry, Springer Netherlands, (1989).
- [17] L. Jiang, N.O.V. Plank, M.A. Blauw, R. Cheung, E.v.d. Drift, Dry etching of SiC in inductively coupled Cl₂/Ar plasma, Journal of Physics D: Applied Physics, **37**, 1809 (2004).
- [18] P.W. Leech, G.K. Reeves, A. Holland, Reactive ion etching of diamond in CF₄, O₂, O₂ and Ar-based mixtures, Journal of Materials Science, **36**, 3453 (2001).
- [19] B. Bhushan, Modern Tribology Handbook, Two Volume Set, CRC Press, (2000).

- [20] M. Bass, O.S.o. America, Handbook of optics, McGraw-Hill, (2001).
- [21] Bruker Ltd. https://cmi.epfl.ch/metrology/Wyko_NT1100.php
- [22] Park system XE100 user manual:
<http://utw10193.utweb.utexas.edu/InstrumentManuals/XE100UserManual.pdf>
- [23] AFM principle: <http://www.parkafm.com/index.php/medias/nano-academy/how-afm-works>
- [24] Geometric of Gaussian beam profile: http://openspim.org/SPIM_Optics_101/Theoretical_basics
- [25] M.A. de Araújo, R. Silva, E. de Lima, D.P. Pereira, P.C. de Oliveira, Measurement of Gaussian laser beam radius using the knife-edge technique: improvement on data analysis, Applied Optics, **48**, 393 (2009).
- [26] A.E. Siegman, M.W. Sasnett, T.F. Johnston, Choice of clip levels for beam width measurements using knife-edge techniques, IEEE Journal of Quantum Electronics, **27**, 1098 (1991).
- [27] A. Gruber, A. Dräbenstedt, C. Tietz, L. Fleury, J. Wrachtrup, C. Von Borczyskowski, Scanning confocal optical microscopy and magnetic resonance on single defect centres, Science, **276**, 2012 (1997).

Chapter 3 Control of photoresist masks by thermal reflow

Photonic devices with specially designed three dimensional (3D) structures are desired to enable new functionality. To fabricate 3D structures in optical materials such as gallium nitride (GaN), silicon, sapphire and diamond by using the lithography method, 3D masks patterning is needed. In particular, controllably fabricating photoresist (PR) micro-masks with specially curved structures on the sample surface is desired.

In this chapter, the controllable fabrication of such PR masks by using photolithography and thermal reflow methods is investigated. A study of profile evolution of the lithographically-defined PR patterns during thermal reflow is presented in Section 3.2. The findings are applied to the controllable fabrication of hemi-toroids in silicon as will be demonstrated in Section 3.3. In particular, PR micro-lenses with a large radius of curvature (ROC) have been fabricated on a diamond surface. These micro-lenses can be applied in a micro-lensed, monolithic Raman laser as will be discussed in section 3.4 and in Chapter 4.

3.1 Introduction

Materials such as GaN, silicon, sapphire and diamond, have great potential for use in optical and photonic devices due to their particular physical properties. To take full advantage of these properties, efficient engineering methods are needed to fabricate photonic devices with special functionalities. In particular, methods of fabricating structures with specially curved surface profiles such as micro-rings or micro-lenses are desired for applications in optoelectronics and laser optics [1-4].

Thermal reflow is a way to create PR patterns by heating the PR to a temperature above its glass transition. During reflow, the PR patterns form spherical surface profiles due to surface tension [5]. Thermal reflow is a commonly used technique to fabricate features with curved surface profiles such as micro-rings [6] or micro-lenses in the PR [1, 5]. The PR micro-lenses can then be transferred into other materials by etching to form convex lenses [7] or by moulding to form concave lenses [8, 9] on different substrates.

Thermal reflow of lithographically-defined PR patterns to form PR micro-lens mask, followed by inductively coupled plasma (ICP) etching to transfer the PR micro-lenses to substrates is a well-established method for lens fabrication. This approach is attractive due to its simplicity, high reproducibility and the high surface quality of the resulting micro-lenses [7, 10]. The engineering aspects of this particular method have been studied and reported in the recent past [11-13]. However, even though the PR reflow step plays a crucial role in determining the profiles of the reflowed PR patterns and eventually the shape of the resulting micro-lenses after pattern transfer, little is known about the detailed processes and mechanisms that determine the exact shape of the reflowed PR. A controllable way of fabricating PR micro-lens patterns with different dimensions and ROCs has not yet been reported. The thermal reflowed PR shapes in relation to the reflow conditions such as the PR thicknesses and reflow temperatures have also not been studied in depth.

In this chapter, a detailed study of the profile evolution of lithographically-defined PR patterns during thermal reflow is presented and then the mechanisms that govern the shape of the reflowed PR is investigated. The PR reflow examination carried out in this work is applicable to fabricate curved profile 3D masks such as micro-toroids and micro-lenses in materials such as silicon and diamond.

Importantly, in this study, the formation and evolution of a bulge at the edge of lithographically-defined PR patterns upon thermal reflow is observed. It is found that during PR reflow, this bulge forms at the edge of the PR pattern and propagates inwards as the temperature and/or PR thickness are increased. This is referred to here as the “edge bulge effect”. To our knowledge, this effect has not been investigated in depth before. There are a couple of known bulge formations that at first may appear similar, namely the “coffee stain effect” in liquid droplets upon solvent evaporation [14, 15], the “edge bead effect” in spin coating [16] and the bulges associated with moving contact lines [17] during PR deposition. However, the edge bulge effect reported here is distinctly different from these known effects. The evolution of the edge bulge is examined as a function of the reflow temperature and the initial thickness of the PR patterns. An empirical relationship for this evolution is derived and discussed in this chapter. Based on this examination, controlled fabrication of PR patterns is realised via the reflow method.

Furthermore, a previously unreported minimum thickness at a certain reflow temperature for the formation of a convex reflowed micro-lens shape on PR patterns is observed and characterised. It is further shown that the PR micro-lens formed at this minimum initial thickness has the largest ROC at its diameter. Based on the study, controllable fabrication of 3D PR masks, namely hemi-toroids and micro-lenses, has been realised as reported in Section 3.3. Moreover, a PR micro-lens pattern with the largest reported ROC of 1.4 mm at a diameter of 400 μm is achieved. By using these PR patterns and ICP etching with a low etching selectivity, silicon hemi-toroid 3D structures have been realised. The process developed in this work enables the realisation of high-quality diamond micro-lenses with ROCs > 10 mm (as will be reported in Chapter 4), which have not been achieved before [4, 18-20]. Part of the work here has been reported in [21].

3.2 Formation and evolution of an edge bulge during the PR reflow

Firstly, an in-depth investigation of the PR edge bulge effect and how it applies to reflowed PR micro-lens patterns with a large ROC was carried out. This study gave valuable guidelines for the fabrication of devices based on this technique.

The PR reflow process employed here consists of three steps: the deposition of the PR on the substrate by spin-coating, the definition of the patterns by photolithography and finally the PR reflow by heating on a hotplate above its glass transition temperature, T_g , over 3 minutes. To pattern the sample, the Shipley 220-7.0 positive PR was first spin-coated on the surface of a substrate using a standard spin speed of 3000 rpm for 1 min. Then the sample was soft-baked on a hotplate at a temperature of 90 °C for 1 min followed by a 35-second exposure under a Karl Suss Mask Aligner 6 and then developed in PR developer (MicroDev from Microchem) for 1 min. Finally, the sample was cleaned with de-ionised water and blow dried with a nitrogen gun. Different initial thicknesses of the PR patterns were achieved by varying the spin speed as well as the number of deposited PR layers. In this work, PR with one, two and three layers were deposited by repeating the spin coating process. During the thermal reflow step, the PR turns into a liquid with a fixed contact line and varying contact angles. The typical view is that the PR droplet can be described as a liquid

whose shape is determined by the surface energy, the PR volume and the contact line [22]. However, the existence of the edge bulge observed shows that this simplified view is not always applicable as will be discussed in Section 3.2.1. It is worth pointing out that for reflow times longer than 3 minutes, PR shapes were observed to be independent of the reflow time and the repetition of the reflow step. The profiles of the patterned PR after reflow and cooling down to room temperature were recorded using a Dektak 3 surface profilometer. In this work, $2 \times 2 \text{ cm}^2$ silicon substrates diced from a 6-inch silicon wafer (purchased from Pi-Kem Ltd., reclaim grade, 425-550 μm thick, single side polished, $\langle 100 \rangle$ orientation, P boron doped, resistivity 0-100 Ohm/cm) were used to provide a large sample area. A similar behaviour of PR reflow was also observed on the diamond surface, as will be reported in section 3.3.2.1.

3.2.1 Edge bulge observation and evolution

In order to investigate the edge bulge evolution, the edge bulge propagation was first carried out on large $1 \times 1 \text{ mm}^2$ square PR patterns which minimise the interaction between the bulges and simulate a single bulge evolution.

A set of micrographs of the propagation process with increasing temperatures at a PR initial thickness (h_0) of 15 μm during thermal reflow is shown in Figure 3-1. As can be seen, the edge bulge forms first at the borders of the pattern and then propagates inward when the reflow temperature is gradually increased.

In order to monitor the bulge propagation quantitatively, a propagation distance (d_{max}) was measured, which corresponds to the position of the highest point of the edge bulge, as illustrated in Figure 3-2. These profiles are derived from the surface profiler measurements of the edge bulges and finally formed spherical lens shape as will be discussed later on. The black curve represents a profile with edge bulges. As the reflow temperature and/or PR thickness are increased, the bulge propagates inwards as indicated by the arrows until eventually a convex lens of approximately the spherical shape (red curve) is formed.

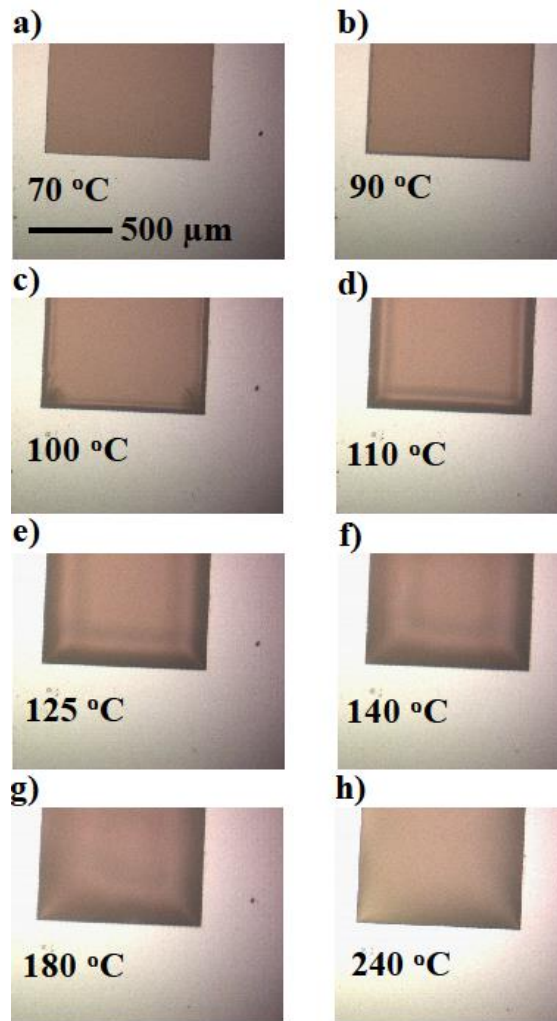


Figure 3-1: Micrographs of PR patterns ($h_0 = 15 \mu\text{m}$) taken at different temperatures during reflow. a) Sample before reflow, $T = 70 \text{ }^\circ\text{C}$, which is below the PR glass transition temperature. (b)-(h) Evolution of the PR pattern while the temperature was gradually raised to $240 \text{ }^\circ\text{C}$.

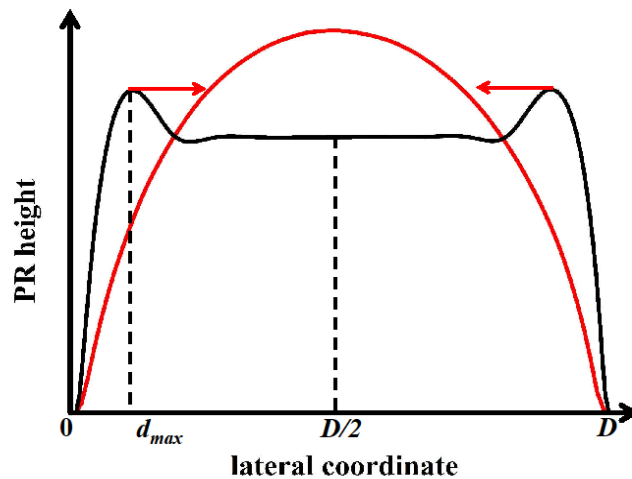


Figure 3-2: Derived profiles from the surface profiler measurements of the edge bulges during reflow in where the black curve represents a profile with an edge bulge and illustrates the key parameters d_{max} and D , and the red curve represents the profile of an eventually evolved convex lens, the arrows indicate the bulge propagation direction.

A schematic illustration of the edge bulge evolution progress is summarised in Figure 3-3 which demonstrates three evolutionary stages of PR bulges on a pattern with a limited area: Stage 1, the bulge formation at the edge of the PR pattern (Figure 3-3 (a)), Stage 2, the propagation of the bulges (Figure 3-3 (b)) and Stage 3, the bulges being completely merged (Figure 3-3 (c)). If the initial PR thickness is large enough, the merged bulges may form a spherical lens shape.

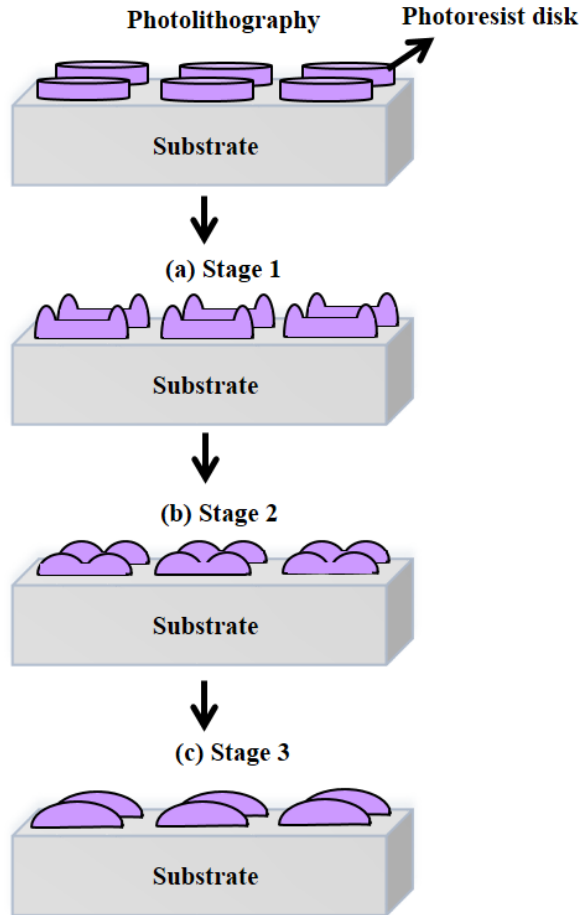


Figure 3-3: Schematic of the PR bulge evolution during reflow.

To investigate the undisturbed propagation of a single bulge during reflow, the profiles of the reflowed edge bulges on the PR patterns was examined. The evolution of the edge bulge is characterised as a function of the reflow temperature, T , and the initial thickness of the PR pattern, h_0 , before reflow. It was observed that in the case of a circular PR pattern with a diameter D , a convex lens shape is formed when $d_{\max} = D/2$, which is also further discussed in Section 3.2.2.

To investigate the influences of T and h_0 , PR patterns with h_0 of $6.3 \mu\text{m}$, $15 \mu\text{m}$ and $21 \mu\text{m}$, corresponding to the thicknesses of the single-, double- and three-layer PR

deposition, respectively, were reflowed at different temperatures. The resulting profiles were measured. In addition, it was found that a PR thickness h_0 around 12 μm , corresponding to the thinnest achievable PR thickness using double-layer PR deposition, could give largest ROC. Thus, a PR pattern reflowed with h_0 at 11.6 μm was also prepared and measured. The d_{max} of these reflowed PR patterns was found to be a function of the reflow temperature which can be empirically derived from the measured d_{max} as shown in Figure 3-4, which plots d_{max} vs. $T-T_g$. The linear theory fit visible in this graph suggests the following empirical relationship:

$$d_{\text{max}} = h_0 \times ((T - T_g)/T_p)^{1/3} \quad (3-1)$$

where $T_p \approx 26.6 \times 10^{-3}$ K is an empirically determined propagation constant, h_0 denotes the initial thickness of the PR pattern and $T_g \approx 352.2$ K denotes the PR glass transition temperature on silicon substrates. The values for T_p and T_g were obtained by fitting the data shown in Figure 3-4.

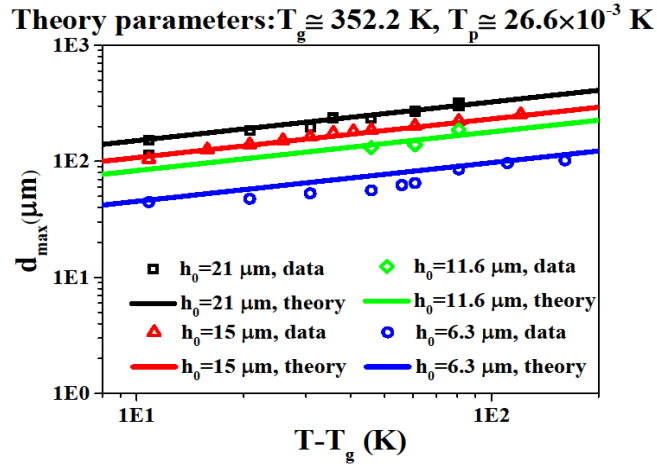


Figure 3-4: d_{max} as a function of $T-T_g$ with h_0 of 6.3, 11.6, 15 and 21 μm , respectively.

As can be seen from Equation (3-1), the d_{max} follows a linear relation of h_0 at a constant reflow temperature. This Equation could be used for the estimation of the propagation of a single bulge on the PR after reflow.

3.2.2 Bulge interaction and minimum thickness for micro-lens formation

In Section 3.2.1, the undisturbed propagation of a single bulge reflowed on the PR pattern was examined. However, in the specific case of micro-lens fabrication, the

bulges from opposing edges of the pattern will eventually interact and merge to form a PR lens shape as shown in Figure 3-2 and Figure 3-3. Furthermore, the bulge propagations might be distorted by the interaction with each other due to a limited propagation area and a circular boundary. This might result in deviations from the propagation behaviour described above in Section 3.2.1. Moreover, a threshold-like phenomenon is expected when the bulges start to merge. After the bulges have completely merged, a convex lens shape is formed as described above.

To investigate the bulge propagation behaviour in a limited area, circular PR patterns with diameters of 200, 250, 350 and 400 μm , respectively, each with different initial thicknesses, were fabricated. These PR patterns were then reflowed at a fixed temperature of 125 $^{\circ}\text{C}$ for 3 min, which is a widely used reflow condition. The d_{max} was measured and is plotted as a function of h_0 in Figure 3-5.

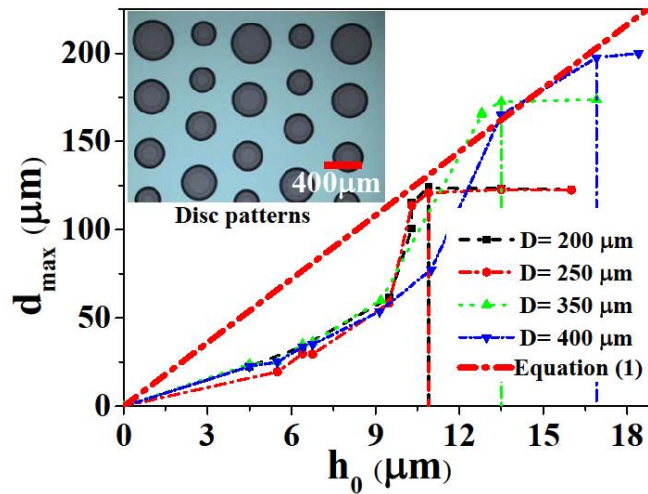


Figure 3-5: Propagation distance d_{max} as a function of the initial thickness h_0 of PR patterns with different diameters. The thick red dashed-dotted line represents Equation (3-1), and the vertical dashed-dotted lines indicate the minimum h_0 at each diameter. Inset: micrograph of PR patterns with an initial thickness of 9.15 μm before thermal reflow.

An optical image of PR patterns at an initial thickness of 9.15 μm before reflow is shown as an inset of Figure 3-5. It can be seen that at first, for $h_0 < 9 \mu\text{m}$, the propagation distance d_{max} of the edge bulge is less than that predicted by Equation (3-1), as represented by a thick red dashed-dotted line in Figure 3-5. As mentioned, this might be an effect of the bulge interaction causing the repulsion of opposing edge bulges in a limited area. Upon further increase of h_0 , d_{max} increases drastically which may be due to the bulge contact and eventually merging.

Additionally, in Figure 3-5, a minimum h_0 at each diameter indicated by the vertical dashed-dotted lines, which corresponds to the point where the d_{\max} reaches the maximum possible value of the $D/2$, can be clearly observed. Above this minimum thickness, the d_{\max} ceased to increase since the bulges completely merged at the centre of the pattern and no further inward propagation is possible. It is worth pointing out that this minimum thickness is consistent with the thickness given by Equation (3-1) for a propagation distance of $d_{\max}=D/2$. This indicates that even for PR patterns with a limited area, Equation (3-1) is applicable to predict the required minimum thickness for bulges merged at the pattern centre to form a convex lens shape at a certain reflow temperature T . For example, to achieve a convex micro-lens with a diameter of $D=400\ \mu\text{m}$, the corresponding d_{\max} should be $200\ \mu\text{m}$. For a conventional reflow temperature of $125\ ^\circ\text{C}$, the minimum PR thickness is calculated to be $16.68\ \mu\text{m}$, which means the PR thickness has to be above this value to form a lens shape after reflow.

In this work, due to the geometry of the Dektak tip with a tip radius of $12.5\ \mu\text{m}$, d_{\max} is systematically overestimated. Note that for $D < 250\ \mu\text{m}$, the systematic error of the Dektak measurement leads to a noticeable overestimation of the diameter in the measured profiles, which is clearly visible in the trace of $D=200\ \mu\text{m}$.

In Figure 3-6, the minimum PR thickness required for lens shape formation with a given lens radius at a reflow temperature of $125\ ^\circ\text{C}$ on silicon is plotted. Similar behaviour has also been observed for PR patterns on diamond.

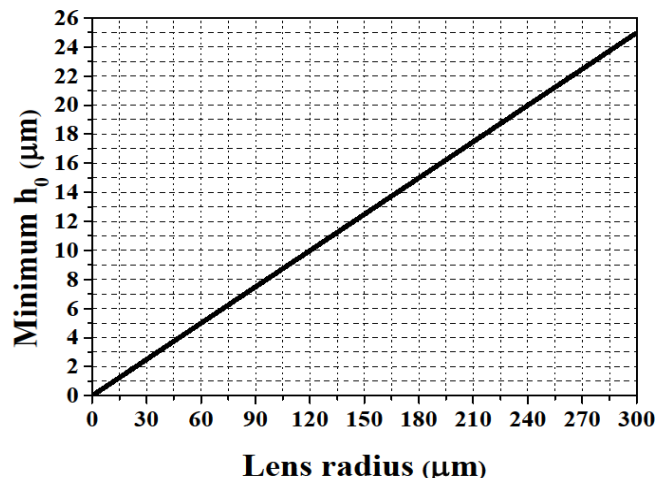


Figure 3-6: Minimum PR thickness needed to form a spherical lens shape with a given radius at a reflow temperature of $125\ ^\circ\text{C}$ on silicon.

Furthermore, it was found that the PR lens shape formed at the minimum initial thickness has the minimum lens height and thus largest ROC at its diameter. Based on this result, a PR micro-lens pattern with the largest reported ROC of 1.4 mm at a diameter of 400 μm was achieved. As shown in Section 3.3.2, such a PR micro-lens pattern with the largest ROC has been successfully transferred onto diamond to form large ROC diamond micro-lenses.

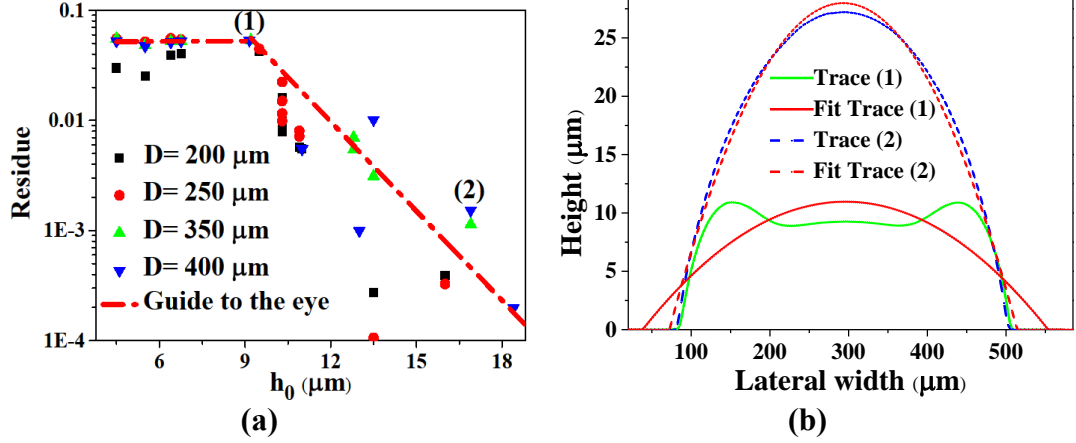


Figure 3-7: (a) Normalised deviation from a spherical lens shape calculated by Equation (3-2) and (b) example traces of measurement and fit of data points (1) and (2) of $D = 400 \mu\text{m}$ shown in (a), Trace (1) $h_0 = 9.15 \mu\text{m}$, $\text{Res} = 0.054$ and Trace (2) $h_0 = 16.9 \mu\text{m}$, $\text{Res} = 0.0015$.

To quantify how closely the reflowed PR shapes resemble a spherical lens shape, the same set of data as shown in Figure 3-5 was fitted by a least squares fit to a spherical shape. As a figure of merit, a normalised least squares residual (Res) is used, which is calculated as:

$$\text{Res} = \frac{\sum_{i=1}^N ((h_{\text{exp},i} - h_{\text{fit},i})^2)}{(N \times h_0^2)} \quad (3-2)$$

where h_{exp} is the height of the experimental trace and h_{fit} is the height of the fitted spherical shape at each point of the trace. The sum is evaluated over all N points of the trace within the interval $[-D/2, +D/2]$, in which the traces are centred to zero. The calculation results are plotted in Figure 3-7 (a). Two examples of the measured and fitted traces are shown in Figure 3-7 (b). It can be seen that the trace with edge bulges deviates strongly from the fitted micro-lens shape and this deviation from the measured trace to the fit can, therefore, be used as a measure for how well the reflowed pattern resembles a spherical lens. In Figure 3-7 (a), for thicknesses $h_0 \leq 9 \mu\text{m}$, Res is approximately constant for different PR thicknesses at a value of $\text{Res} \approx 0.05$. This value

corresponds to Trace (1) in Figure 3-7 (b). When $h_0 > 9 \mu\text{m}$, Res decreases at an exponential rate as indicated by the dashed-dotted line in Figure 3-7 (a). This means that, once a certain thickness is exceeded, the reflowed PR pattern changes to a spherical lens shape exponentially upon further increase of the PR thickness. A typical profile of such a spherical lens shape is shown as Trace (2) in Figure 3-7 (b).

Furthermore, these results on the evolution of the PR profile also show that apart from spherical lenses, PR shapes like hemi-toroids or aspheric micro-lenses can also be achieved by the precise control of h_0 and T, as will be discussed in Section 3.3.

3.2.3 Discussion on the PR bulge evolution during reflow

In this section, the observation of the edge bulge effect is related to past attempts to understand the profiles generated by PR reflow on a theoretical basis. In the simplest and most commonly used case, it is assumed that during reflow, the PR becomes an ideal liquid that forms a droplet with a fixed contact line [17] (or, in a few cases, with a fixed contact angle [22]). This approach satisfactorily describes the reflowed PR shapes obtained well above the minimum thickness described in Section 3.2.2. The more complex shapes observed below minimum thickness, however, cannot be explained by this approach. The underlying reason is that the droplet shape is calculated assuming that the pressure drop determined by the Young-Laplace law equals a constant term (related to the surface tension) plus a contribution from an external force, i.e., in particular, gravity [13]:

$$1/R_1 + 1/R_2 = c + f_{\text{ext}} \quad (3-3)$$

where R_1 and R_2 are the local ROCs of the surface, c is a constant, and f_{ext} is the contribution of external forces [23]. At the edge bulge, a change in sign of the local ROC, is encountered and thus of the pressure drop calculated by the Young-Laplace law. This intriguing observation is a fundamental problem for this simple approach.

Very few theoretical investigations have been made that consider more complex shapes. Audran *et al.* [12] numerically solved the Navier-Stokes Equations and were thus able to model the temporal evolution of the droplet, including intermediate shapes that contain an edge bulge. However, their final shape still does not have an edge bulge. Since the edge bulge observed by us does not represent an intermediate temporal shape, it is questionable if it can really be explained by this model. O'Neill and

Sheridan [11, 24] summarised a number of fitting procedures for the recorded pattern profiles that account for complex surface shapes. While these fitting methods may be useful for engineering purposes, they do not give any insight into the physics causing the observed shapes.

To summarise, the physics of the edge bulge formation remains essentially unknown. It is possible that the underlying mechanism is a so far unexplored aspect of fluid mechanics. Here, we mainly focus on the experimental results and their application in micro-lens fabrication.

3.3 Applications of the controllable PR reflow process

3.3.1 Hemi-toroid on silicon

The potential applications of the controllable PR reflow process developed here is to fabricate special 3D curved profile structures such as hemi-toroids and aspheric micro-lenses on solid-state substrates, i.e. silicon and diamond. As an example, by applying the technique developed above, silicon hemi-toroids were fabricated using the process flow shown in Figure 3-8.

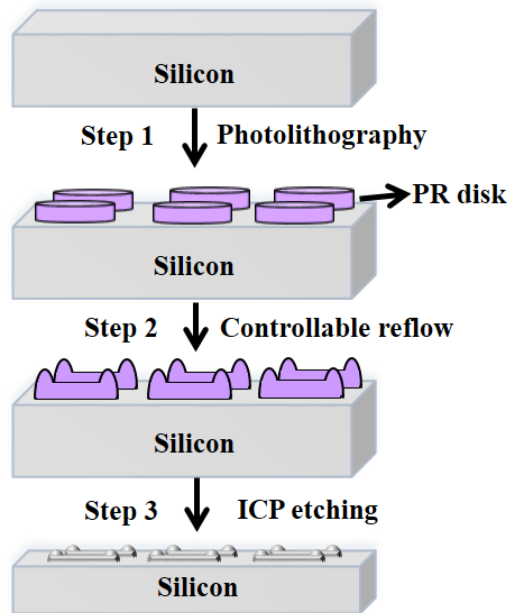


Figure 3-8: Schematic of the process steps for hemi-toroid fabrication on silicon.

Firstly, PR disks were fabricated using photolithography on silicon substrates as shown in Step 1 of Figure 3-8. PR bulges were fabricated on a PR disk pattern (D from 200 to 400 μm) at a reflow temperature of 90 $^{\circ}\text{C}$ and $h_0 = 8.6 \mu\text{m}$ as shown in Step 2

of Figure 3-8. Under these conditions, the d_{\max} is estimated to be $64 \mu\text{m}$. These PR bulges formed PR hemi-toroid structures which were etched to transfer into a silicon substrate as shown in Step 3 of Figure 3-8. The etch recipe used here was: pressure 5 mTorr, Ar flow rate 25 sccm, Cl_2 flow rate 40 sccm, platen power 300 W and coil power 400 W. A plan view optical image of the fabricated hemi-toroids on a silicon substrate is shown in Figure 3-9.

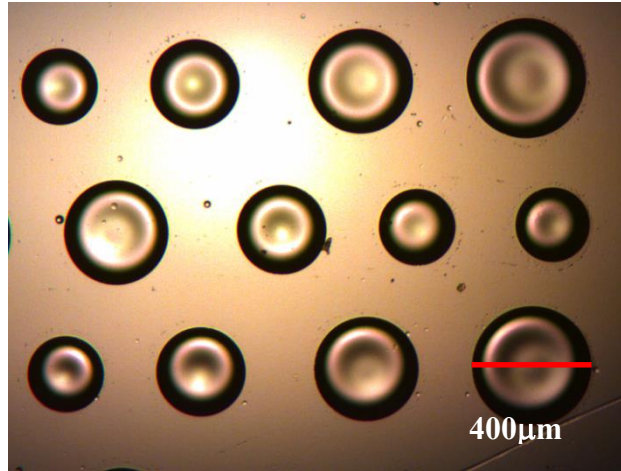


Figure 3-9: Plan view optical image of the fabricated silicon hemi-toroids with D from 200 to $400 \mu\text{m}$.

The fabricated silicon hemi-toroids were characterised using a Dektak surface profilometer. The measured profiles of the PR and a transferred silicon hemi-toroid are shown in Figure 3-10. From Figure 3-10, the measured height of the silicon hemi-toroids is about $1.5 \mu\text{m}$ which agrees well the estimated value based on the height of the original PR bulge and the etch selectivity of PR to silicon under the Ar/ Cl_2 etching.

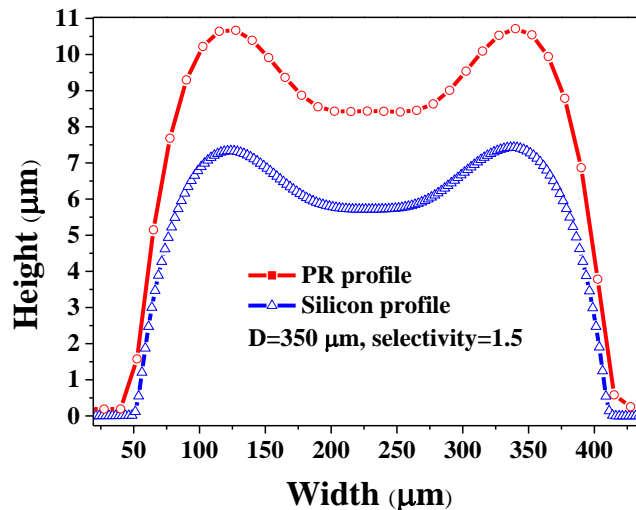


Figure 3-10: Measured profiles of a typical PR and silicon hemi-toroid with a diameter of $350 \mu\text{m}$.

The d_{\max} of the achieved profiles was measured to be 76.6 μm and was close to the estimated value. These fabricated silicon hemi-toroids demonstrate the capability of the PR reflow process developed for such special structure fabrication.

By using an appropriate ICP etching method to transfer the PR patterns, hemi-toroid structures on diamond or other solid state materials could also be realised. This method could also be used to fabricate arrays of concave-lens patterns formed from the PR bulges with tunable separation.

3.3.2 Micro-lenses with large ROCs

As introduced in Chapter 1, diamond is an attractive material for photonic device. To fabricate diamond photonic devices such as diamond micro-lenses with a large ROC, a PR micro-lens with a large ROC and a low ICP etching selectivity for pattern transfer are necessary. The study in Section 3.2.2 demonstrates that at a certain diameter, there is a minimum PR thickness required to form a spherical PR lens structure by thermal reflow on silicon. The PR lens structure formed by adopting this minimum PR thickness has the largest ROC at a certain diameter as it gives a minimum lens height after thermal reflow. The lens ROC is calculated by Equation (3-4):

$$ROC = (D^2 + 4h^2)/8h \quad (3-4)$$

where D is the lens diameter and h is the lens height, respectively.

3.3.2.1 PR thermal reflow on a diamond surface

The work reported here shows that the PR thermal reflow behaviour on a diamond surface is similar to that on a silicon surface. By applying these findings together with a suitable ICP etch method, the fabrication of large ROC micro-lenses on a high-quality single crystal diamond can be achieved. The detailed results will be presented in the following section.

To investigate the PR thermal reflow behaviour and the edge bulge propagation on the diamond surface during reflow, PR patterns which were the same as those used in Section 3.2.1 were developed. The h_0 of these developed PR patterns were 7.2, 16.3 and 20.5 μm , respectively. Reflow temperatures starting from 90 $^{\circ}\text{C}$ up to 240 $^{\circ}\text{C}$ were applied to investigate the single bulge propagation on the diamond surface. Figure 3-11 shows the measured data and fitted curves of the d_{\max} over $T-T_g$. A similar relation

of d_{\max} and T can be derived from these data and fits with $T_g \approx 361.3$ K and $T_p \approx 3.1 \times 10^5$ K. After fitting the measured data, the propagation distance of the PR bulge, d_{\max} over reflow temperature T on a diamond surface, is chosen to fit the data as:

$$d_{\max} = h_0 \times ((T - T_g)/T_p)^{1/5} \quad (3-5)$$

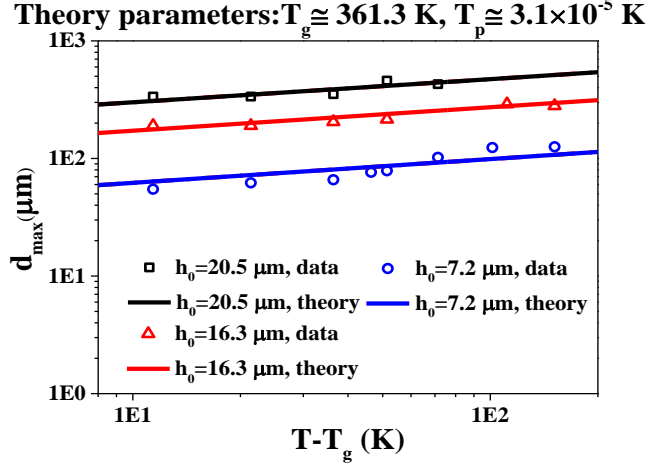


Figure 3-11: Measured and fit of the data of PR bulge propagation on the surface of diamond in which d_{\max} is a function of $T - T_g$ with h_0 of 7.2 μm , 16.3 μm and 20.5 μm , respectively.

Note that the obtained T_g and T_p for PR on diamond might be due to the different characteristics of the diamond and silicon surfaces. However, this derived formula is still suitable as a guideline for the controllable fabrication of PR micro-lens patterns on diamond and subsequent special diamond micro-lens fabrication. The development of the large ROC PR micro-lenses on the diamond surface based on these findings is described in Section 3.3.2.2.

3.3.2.2 Fabrication of large ROC PR micro-lenses on diamond

In the work reported here, a PR micro-lens array mask with a diameter of 400 μm was fabricated on a 4×4 mm^2 optical grade single crystal diamond platelet with a root-mean-square (RMS) surface roughness of < 5 nm (Element 6 Ltd.). A multiplex ICP etch tool (SPTS Ltd.) was used to transfer the PR mask pattern onto diamond. Based on the study shown in Section 3.3.2.1, for a PR micro-lens of 400 μm in diameter and a reflow temperature of 125 $^\circ\text{C}$, the minimum PR thickness is achievable using a thickness that gives adequate uniformity and fidelity of the developed PR patterns on the diamond. Furthermore, increasing the PR thickness will also result in significantly reduced uniformity and pattern fidelity due to an increasing influence of the edge bead effect on the small diamond sample (as will be discussed in detail in Chapter 4).

Therefore, a higher reflow temperature over 135 °C was applied, which allowed PR micro-lens formation with an initial thickness of $h_0=11.5 \mu\text{m}$ on the diamond. In this way, the resulting PR micro-lens on diamond had a ROC as large as 1.4 mm. To fabricate a diamond micro-lens with a larger ROC, an etch recipe with a low etch selectivity is required to transfer the PR micro-lens mask to diamond. The PR profiles formed under one-layer PR deposition and formed at controlled PR thickness based on multiple layers and reflow temperature are shown in Figure 3-12. The etched diamond micro-lens array is shown in Chapter 4, Figure 4-12.

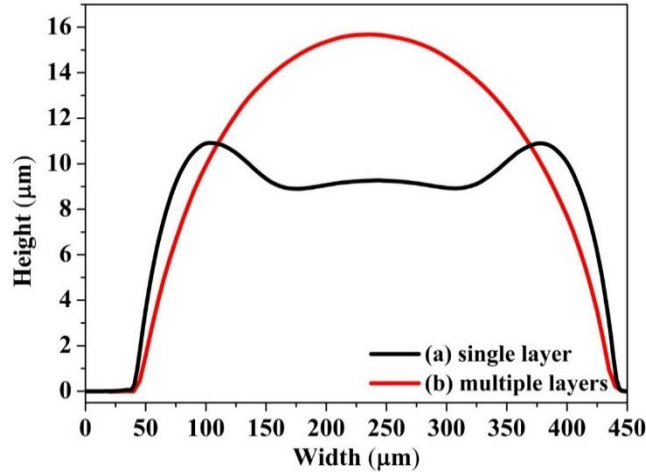


Figure 3-12: Comparison of profiles of formed PR patterns on diamond: (a) the profile with edge bulges formed using single PR layer and (b) the micro-lens formed by controlling the PR thickness at 11.5 μm and a reflow temperature over 135 °C (ROC=1.4 mm) using multiple PR layers.

3.4 Outlook

Based on this study, patterned structures other than spherical convex lenses, such as hemi-toroids [25], concave-lenses, aspheric micro-lenses and the hemi-toroid on optical materials such as GaN, silicon, sapphire and diamond, should be achievable by using the precise control of the PR reflow and optimised ICP etching. Diamond micro-lenses with such large ROCs resulting from these PR masks can be used to form micro-resonators [26] and serve as crucial components for application in a monolithic diamond Raman laser [27]. The detail of the fabrication of these special diamond micro-lenses including the challenges of the fabrication process and the performance of these special micro-lenses in a monolithic diamond Raman laser will be discussed in Chapter 4. The technique of diamond micro-lens fabrication with such special geometry might also find use in SILs for quantum related technologies [28-30].

Similarly, micro-lenses with different diameters and ROCs in various other materials can be achieved following the principles outlined here and might find application in imaging [31] or displays [32]. Importantly, the PR micro-lens masks on a diamond surface discussed in 3.3.2.2 were later transferred to diamond via ICP etching with Ar/Cl₂ plasma [10], which enabled the diamond micro-lens with a state-of-the-art large ROC. This result will be reported in detail in Chapter 4.

3.5 Conclusions

The “edge bulge effect” exhibited during the PR pattern reflow process has been studied and the findings have been applied to develop novel 3D resist geometries on silicon and diamond. An empirical description and relationship of the PR edge bulge evolution as a function of the initial PR thickness and the reflow temperature was provided, although the underlying physics still open to discussion. Importantly, in the case of the fabrication of micro-lenses with certain pattern diameters, it was observed that there is a minimum PR thickness at which a spherical PR lens structure can be formed by thermal reflow and that the lens profile formed has the largest ROC. This minimum thickness is predictable by using Equation (3-1) on silicon and Equation (3-5) on diamond. This study underpins the controllable fabrication of PR patterns using thermal reflow. Furthermore, by combining the controllable fabrication of PR patterns with the PR pattern transfer via suitable ICP etching, silicon hemi-toroids have been achieved.

References

- [1] H.W. Choi, E. Gu, C. Liu, J.M. Girkin, M.D. Dawson, Fabrication and evaluation of GaN negative and bifocal microlenses, *Journal of Applied Physics*, **97**, 1 (2005).
- [2] H.W. Choi, C. Liu, E. Gu, G. McConnell, J.M. Girkin, I.M. Watson, M.D. Dawson, GaN micro-light-emitting diode arrays with monolithically integrated sapphire microlenses, *Applied Physics Letters*, **84**, 2253 (2004).
- [3] E. Gu, H.W. Choi, C. Liu, C. Griffin, J.M. Girkin, I.M. Watson, M.D. Dawson, G. McConnell, A.M. Gurney, Reflection/transmission confocal microscopy characterization of single-crystal diamond microlens arrays, *Applied Physics Letters*, **84**, 2754 (2004).
- [4] N. Laurand, C.L. Lee, E. Gu, J.E. Hastie, S. Calvez, M.D. Dawson, Microlensed microchip VECSEL, *Optics Express*, **15**, 9341 (2007).
- [5] D. Daly, R.F. Stevens, M.C. Hutley, N. Davies, The Manufacture of Microlenses by Melting Photoresist, *Measurement Science and Technology*, **1**, 759 (1990).

- [6] C.L. Lee, E. Gu, M.D. Dawson, Micro-cylindrical and micro-ring lenses in CVD diamond, *Diamond and Related Materials*, **16**, 944 (2007).
- [7] H.W. Choi, E. Gu, C. Liu, C. Griffin, J.M. Girkin, I.M. Watson, M.D. Dawson, Fabrication of natural diamond microlenses by plasma etching, *Journal of Vacuum Science & Technology B*, **23**, 130 (2005).
- [8] E. Roy, B. Voisin, J.F. Gravel, R. Peytavi, D. Boudreau, T. Veres, Microlens array fabrication by enhanced thermal reflow process: Towards efficient collection of fluorescence light from microarrays, *Microelectronic Engineering*, **86**, 2255 (2009).
- [9] C.L. Lee, H.W. Choi, E. Gu, M.D. Dawson, H. Murphy, Fabrication and characterization of diamond micro-optics, *Diamond and Related Materials*, **15**, 725 (2006).
- [10] C.L. Lee, E. Gu, M.D. Dawson, I. Friel, G.A. Scarsbrook, Etching and micro-optics fabrication in diamond using chlorine-based inductively-coupled plasma, *Diamond and Related Materials*, **17**, 1292 (2008).
- [11] F.T. O'Neill, J.T. Sheridan, Photoresist reflow method of microlens production Part I: Background and experiments, *Optik*, **113**, 391 (2002).
- [12] S. Audran, B. Mortini, B. Faure, G. Schlatter, Dynamical formation of microlenses by the reflow method: numerical simulation and experimental study of the process fabrication, *Journal of Micromechanics and Microengineering*, **20**, 095008 (2010).
- [13] A. Schilling, R. Merz, C. Ossmann, H.P. Herzig, Surface profiles of reflow microlenses under the influence of surface tension and gravity, *Optical Engineering*, **39**, 2171 (2000).
- [14] R.D. Deegan, O. Bakajin, T.F. Dupont, G. Huber, S.R. Nagel, T.A. Witten, Capillary flow as the cause of ring stains from dried liquid drops, *Nature*, **389**, 827 (1997).
- [15] S. Das, P.R. Waghmare, M. Fan, N.S.K. Gunda, S.S. Roy, S.K. Mitra, Dynamics of liquid droplets in an evaporating drop: liquid droplet "coffee stain" effect, *RSC Advances*, **2**, 8390 (2012).
- [16] T. Dobroth, L. Erwin, Causes of Edge Beads in Cast Films, *Polymer Engineering & Science*, **26**, 462 (1986).
- [17] I.S. McKinley, S.K. Wilson, The linear stability of a drop of fluid during spin coating or subject to a jet of air, *Physics of Fluids*, **14**, 133 (2002).
- [18] E. Woerner, C. Wild, W. Mueller-Sebert, P. Koidl, CVD-diamond optical lenses, *Diamond and Related Materials*, **10**, 557 (2001).
- [19] N. Laurand, C.L. Lee, E. Gu, S. Calvez, M.D. Dawson, Power-Scaling of Diamond Microlensed Microchip Semiconductor Disk Lasers, *IEEE Photonics Technology Letters*, **21**, 152 (2009).
- [20] N. Laurand, C.L. Lee, E. Gu, J.E. Hastie, A.J. Kemp, S. Calvez, M.D. Dawson, Array-Format Microchip Semiconductor Disk Lasers, *IEEE Journal of Quantum Electronics*, **44**, 1096 (2008).
- [21] H. Liu, J. Herrnsdorf, E. Gu, M.D. Dawson, Control of edge bulge evolution during photoresist reflow and its application to diamond microlens fabrication, *Journal of Vacuum Science & Technology B*, **34**, 021602 (2016).

-
- [22] N. Ph, R. Völkel, H.P. Herzig, M. Eisner, S. Haselbeck, Design, fabrication and testing of microlens arrays for sensors and microsystems, *Pure and Applied Optics: Journal of the European Optical Society Part A*, **6**, 617 (1997).
- [23] B. Lautrup, *Physics of Continuous Matter: Exotic and Everyday Phenomena in the Macroscopic World*, Chapter 8, IOP Publishing Ltd., (2005).
- [24] F.T. O'Neill, J.T. Sheridan, Photoresist reflow method of microlens production Part II: Analytic models, *Optik*, **113**, 405 (2002).
- [25] M.-H. Wu, K.E. Paul, G.M. Whitesides, Patterning flood illumination with microlens arrays, *Applied Optics*, **41**, 2575 (2002).
- [26] H. Liu, S. Reilly, J. Herrnsdorf, E. Xie, V.G. Savitski, A.J. Kemp, E. Gu, M.D. Dawson, Large radius of curvature micro-lenses on single crystal diamond for application in monolithic diamond Raman lasers, *Diamond and Related Materials*, **65**, 37 (2016).
- [27] S. Reilly, V.G. Savitski, H. Liu, E. Gu, M.D. Dawson, A.J. Kemp, Monolithic diamond Raman laser, *Optics Letters*, **40**, 930 (2015).
- [28] W. Pfaff, B.J. Hensen, H. Bernien, S.B. van Dam, M.S. Blok, T.H. Taminiau, M.J. Tiggelman, R.N. Schouten, M. Markham, D.J. Twitchen, R. Hanson, Unconditional quantum teleportation between distant solid-state quantum bits, *Science*, **345**, 532 (2014).
- [29] M. Jamali, I. Gerhardt, M. Rezai, K. Frenner, H. Fedder, J. Wrachtrup, Microscopic diamond solid-immersion-lenses fabricated around single defect centres by focused ion beam milling, *Review of Scientific Instruments*, **85**, 123703 (2014).
- [30] J.P. Hadden, J.P. Harrison, A.C. Stanley-Clarke, L. Marseglia, Y.L.D. Ho, B.R. Patton, J.L. O'Brien, J.G. Rarity, Strongly enhanced photon collection from diamond defect centres under microfabricated integrated solid immersion lenses, *Applied Physics Letters*, **97**, 1 (2010).
- [31] R.P. Rocha, J.P. Carmo, J.M. Gomes, M. Belsley, J.H. Correia, Microlenses Array Made with AZ4562 Photoresist for Stereoscopic Acquisition, *Procedia Engineering*, **47**, 619 (2012).
- [32] T. Knieling, M. Shafi, W. Lang, W. Benecke, Microlens array production in a microtechnological dry etch and reflow process for display applications, **7**, 12007 (2012).

Chapter 4 Large radius of curvature diamond micro-lenses and monolithic diamond Raman lasers

In this chapter, a novel monolithic diamond Raman laser, in which the diamond served as both a Raman gain medium and a micro-resonator is described. The micro-resonator is formed by mirror coating both the micro-lensed and the back plane facets of a monolithic single crystal chemical vapour deposition (CVD) diamond. Such a monolithic diamond Raman laser needs minimal alignment and requires no external mirrors to form an optical resonator, and hence is more compact and robust compared to conventional diamond Raman lasers.

Work on how to realise such a monolithic diamond Raman laser will be presented in this chapter. A micro-lensed monolithic diamond with a large radius of curvature (ROC) to provide a large mode area for the resonator is critical, as described in Section 4.1. The details of the importance and design principles of this diamond micro-lensed resonator are discussed in Section 4.2. The challenges of developing such large radii of curvature micro-lensed resonator in single crystal CVD diamond are described in Section 4.3.

An optimised photoresist (PR) reflow process based on the study of controllable PR reflow as discussed in Chapter 3 and a low selectivity inductively coupled plasma (ICP) etching are used to realise a uniform array of micro-lenses on diamond. As a result, diamond micro-lenses with radii of curvature of 13 mm or more and a high quality surface of root-mean-square (RMS) roughness of 0.18 nm have been developed. Potentially, diamond micro-lenses with an even larger ROC can be achieved using the processes developed in this work. Utilising these new diamond micro-lenses enabled a pulse energy scalable monolithic diamond Raman laser where large ROCs of the micro-lenses are critical. The demonstration and characterisation of such a monolithic diamond Raman laser will be described in Section 4.4.

4.1 Introduction

High power solid-state lasers such as rod lasers, thin disk lasers and Raman lasers are challenged by issues of heat management. This includes “thermal lensing” (in high

power lasers, the gain medium is heated up, causing a transverse gradient of the refractive index from the beam axis to the outer regions, which results in a lensing effect) [1] and “thermal expansion” (thermal induced mechanical bulging of the crystal) [2]. These issues degrade the laser performance and can damage the laser.

An efficient method of heat management is therefore desired to solve these thermal issues. The unparalleled thermal conductivity of diamond, as discussed in Chapter 1, makes it an outstanding material to efficiently manage the heat in high power laser applications [3, 4]. In fact, diamond has already been used as a heat spreader for thermal management in laser diodes [5] and in light emitting diode packages [6, 7] due to its outstanding thermal conductivity.

Additionally, diamond has long been studied [8] as one of the most effective optical and optoelectronic materials. Its unrivalled properties of wide transparency range (from ~220 nm to 2.5 μm) [9], high thermal conductivity ($2000 \text{ Wm}^{-1}\text{K}^{-1}$) [10] and large Raman gain coefficient (which is a function of $1/\lambda$ as discussed in Table 1-2 Chapter 1, and is measured to be ~42 cm/GW at 532 nm [11], with previously reported values ranged between 20~75 cm/GW [8, 12]), along with recent advances in the growth of single crystal synthetic diamond [13] have led the material being one of the best choices to be used in Raman lasers [14].

Raman lasers are based on stimulated Raman scattering which is a way of efficiently converting a pump laser beam with a certain wavelength to an output laser beam with another longer wavelength. A diamond Raman laser is attractive due to the diamond crystal having a high thermal conductivity which solves the thermal issues and a high Raman gain coefficient which means a shorter length of laser crystal needed and thus a more compact laser configuration can be achieved. Furthermore, diamond has a large Stokes shift to allow access to hard to reach wavelengths. Moreover, a diamond Raman laser can also be used to convert a low brightness source to a beam operating near the diffraction limit. In biomedical applications, for example, a laser that is compact and robust and converts widely available pulsed green output to the yellow-orange spectral region is highly desired [15] and this can be achieved via the capabilities of a diamond Raman laser.

4.2 Diamond Raman laser

A diamond Raman laser is a special laser that converts a certain wavelength of input light to another longer wavelength of output using stimulated Raman scattering (SRS) in diamond to provide gain. When pumped with a laser source, the incident photons interact with vibrational modes in the diamond crystal. When a high enough photon flux is reached, i.e. when the threshold is exceeded, SRS leads to the incident photon with higher energy being converted into a lower-energy signal photon, and the difference of photon energies is carried away by a phonon (a quantum of the lattice vibrations). A schematic demonstrating the principle of Raman scattering is shown in Figure 4-1, where in this illustrative case, the Stokes shift is such as to convert the input green laser pump to a yellow Raman laser output.

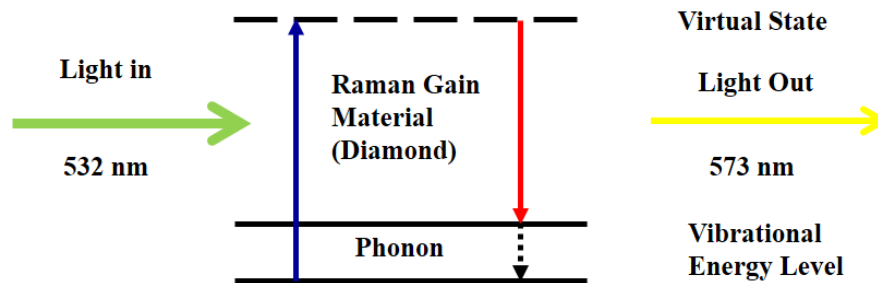


Figure 4-1: Mechanism of Raman scattering in a diamond Raman laser, (a wavelength shift from 532 nm to 573 nm is used here for illustration).

SRS was first observed in natural diamonds in 1963 [16]. It was not until 2004 that the SRS was observed in a 350 μm thick polycrystalline diamond with a pulsed laser for the first time [17]. Intensive efforts have been put into research on diamond Raman lasers since then.

Conventionally, diamond Raman lasers are composed of three parts: a pump laser (the input source of energy for the system), a diamond (the Raman gain medium which takes that energy and uses it to amplify light), and external mirrors used to form a laser resonator (oscillating the SRS light through the gain medium to build up the laser output) [12]. An example of such a diamond Raman laser is shown in Figure 4-2. Diamond Raman lasers with both high output power and continuous wave (CW) output have been reported. For example, 1.6 W output power was reported using a CW laser [18] and 24.5 W output power was reported using a pulsed laser [19]. Now over 100 W output power has been reported [20]. Before 2008, SRS with diamond was mainly

achieved using such pulsed lasers. The first CW diamond Raman laser was reported by Lubeigt et al. with an output power of 200 mW [21]. Then a 1.6 W CW diamond Raman laser was reported [18] and a 5.1 W output CW diamond Raman laser was reported [14]. A 10.1 W output power CW diamond Raman laser was reported in [22] using an external resonant cavity, which to the best of our knowledge is the highest CW Raman output power reported so far with diamond.

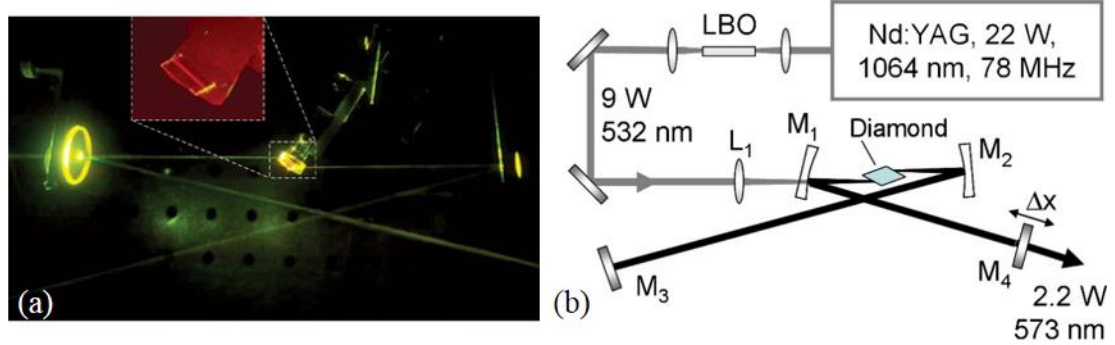


Figure 4-2: (a) A conventional picosecond pulsed diamond Raman laser and (b) a schematic of this laser [23].

However, in this work, by forming micro-lens structures onto the diamond surface and coating with dielectric mirrors, a simpler, more compact and robust monolithic diamond Raman laser has been achieved. This monolithic diamond Raman laser needs minimal alignment (mainly of the laser beam through the micro-lens) and has no further requirements of external mirrors [24]. The monolithic diamond Raman laser developed here and its schematic are shown in Figure 4-3 (a) and (b), respectively.

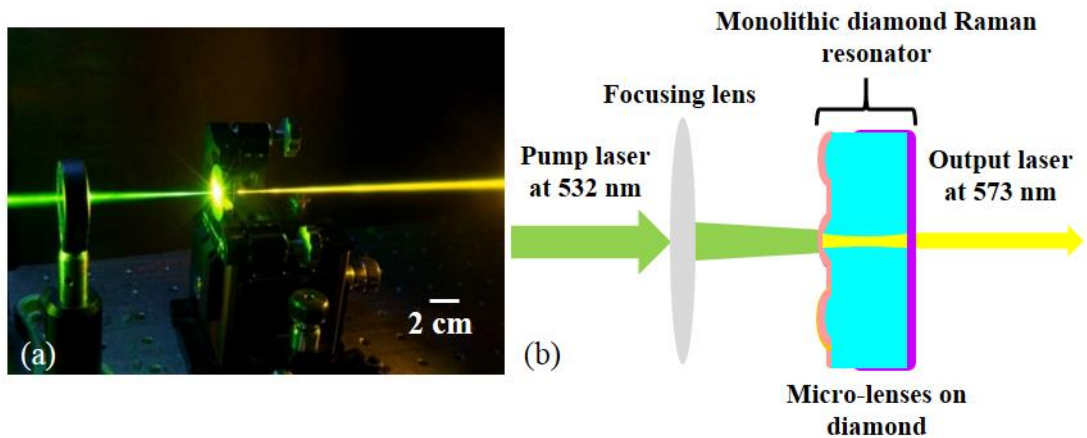


Figure 4-3: (a) Demonstration of a monolithic diamond Raman laser based on the micro-lensed resonator using a pulsed 532 nm laser of 1.5 ns duration at a pump pulse energy of 1.5 μ J and (b) Schematic of the monolithic diamond Raman laser.

4.2.1 Diamond micro-lenses and micro-resonators

To realise such a monolithic diamond Raman laser, the optimisation of the fabrication process for fabricating diamond micro-lenses is of critical importance since the Raman cavity mode is primarily defined by the micro-lens characteristics [24]. A large cavity mode, and hence a large ROC (>10 mm) micro-lens, as discussed in Section 4.2, is crucial to avoid high power laser-induced damage to the diamond and to the optical coatings deposited on the diamond surface.

Diamond micro-lenses have attracted much attention in previous studies due to their performance e.g. as a laser cavity to stabilize laser oscillation [4] and as a solid immersion lens (SIL) to collect light [25, 26]. However, lens fabrication on diamonds is difficult due to the extreme hardness and chemical inertness of diamond itself. Research on diamond micro-lenses has accelerated during the last decade due to the development of synthetic diamond [27], which reduces the cost of diamonds for research and applications. Recently, the achievement of diamond micro-lenses with diameters from tens to hundreds of microns were reported by different groups using different fabrication techniques [28-31].

The techniques for fabricating diamond micro-lenses are categorised into four main methods which are summarised as follows. The first method was developed by W. Nelissen et al. who used a laser-cutting technique and polished a 1 mm diameter diamond micro-lens with a RMS surface roughness of less than 30 nm from homo-epitaxial CVD diamond [32]. This polished diamond micro-lens was used [33] as a SIL to increase the collection of single photons from colour centres, as described in Chapter 1. However, the diamond SIL is relatively large and the approach is not scalable for the diamond micro-lenses discussed here. The second method, proposed by J. P. Hadden et al., is to mill a diamond SIL by sequential concentric ring cuts with different diameters and gradient height increase using a focused ion beam (FIB) [34]. This method is potentially scalable with capabilities of aligning the lens with individual colour centres [35]. Similar FIB methods were used by Ronald Hanson et al. [36, 37]. However, the drawback of this FIB milling process is the relatively long time it takes. The third diamond lens fabrication method used a bottom-up CVD growth approach, as reported by E. Woerner [29]. By growing diamond onto structured substrates followed by a subsequent lift off process, freestanding diamond lenses are

formed. The limit of this method is that the grown diamond can only be polycrystalline which has a much lower quality than single crystal diamonds. The fourth method involves the use of PR thermal reflow and plasma etching. The lens pattern is first formed in reflowed PR due to surface tension and then plasma etching transfers the PR lens shapes into diamond [30, 31]. The micro-lenses made in this way, reported so far, have lens diameters ranging from 20 μm to 100 μm and a methodology involving single layer-PR thermal reflow [38] and pattern transfer by ICP etching was widely used. This approach yields simplicity, high reproducibility and high lens surface quality and is adapted for our micro-lens fabrication. However, to the best of our knowledge, the ROC of diamond micro-lenses fabricated using this methodology have so far been limited to below 10 mm [3, 28-31].

In general, diamond micro-lenses are fabricated by single-layer PR thermal reflow [38] to form PR micro-lenses and then Ar/O₂ ICP etching to transfer the PR structures into diamond [28]. However, to make diamond lenses with a large ROC, this method needed to be further developed. The difficulties of fabricating diamond micro-lenses with a large ROC are threefold. Firstly, the PR layer may have a non-uniform thickness due to the “edge bead” effect during PR coating on a small sample surface [39]. Secondly, as discussed in more detail in Section 4.3 and Chapter 3, an edge bulge phenomenon occurs during thermal reflow when the applied PR is too thin. Finally, the conventionally used Ar/O₂ plasma etching does not have the optimal etch selectivity (typical > 0.22 [42], and as compared in Table 2-2 and Table 2-3) for the transfer of shallow micro-lens patterns.

In our work, a novel fabrication process was developed that enables the production of diamond micro-lenses with larger ROCs. This process uses an optimised thermal reflow of multiple-layer PR to achieve a large ROC micro-lens PR mask and then a low selectivity Ar/Cl₂ ICP etching to transfer this micro-lens PR mask pattern into diamond. Profilometry and optical measurements have shown that the ROCs of the fabricated 400 μm diameter diamond micro-lenses are around 13 mm and these micro-lenses on a single crystal CVD diamond have an RMS roughness of 0.18 nm on an area of $3 \times 3 \mu\text{m}^2$ of the micro-lens top surface. Such high quality diamond micro-lenses have enabled us to achieve monolithic diamond Raman lasers with a high pump to output conversion efficiency.

4.3 Design of the diamond micro-lenses

In a monolithic diamond Raman laser, two facets of a diamond sample, the front micro-lensed surface and the back planar surface, are coated with dielectric mirrors to form a monolithic resonator. These coatings can be damaged if the optical field intensity exceeds a certain threshold.

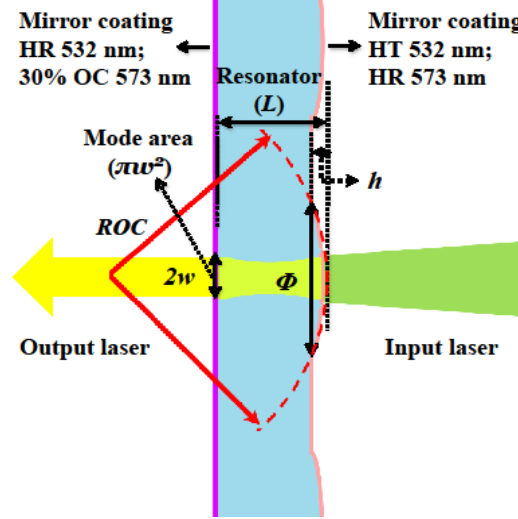


Figure 4-4: Schematic of the resonator based on a diamond micro-lens illustrating the key parameters of: beam radius on the planar surface w , mode area πw^2 , resonator length L , lens diameter Φ and lens height h . Specifications of mirror coatings are: HT 532 nm, high transmission at 532 nm; HR 532/573 nm, high reflectivity at 532/573 nm; 30% OC 573 nm, 30% output coupling at 573 nm.

The peak intensity (P_{max}) of a laser at the side of the plane mirror is determined by the mode area:

$$P_{max} = \frac{E}{\Delta\tau \times (\pi w^2)} \quad (4-1)$$

where w represents the beam radius of the mode area (πw^2), E denotes the pump pulse energy and $\Delta\tau$ is the pump pulse duration. These key parameters are illustrated in Figure 4-4. Hence, a large mode area is critical to enable higher pulse energies without damage. The beam radius w on the plane surface of the micro-lens resonator depends on the ROC of the micro-lens, the wavelength of the laser emission λ , the length of the diamond micro-lens resonator L and the refractive index of diamond n (~ 2.42)[3]:

$$w = \sqrt{\frac{L \times \lambda}{n \times \pi}} \times \sqrt{\frac{ROC \times n}{L} - 1} \quad (4-2)$$

From Equation (4-2) it can be seen that a large mode area can be achieved by fabricating micro-lenses with a large ROC. In particular, a micro-lens ROC larger than 10 mm is critical if a micro-joule-class diamond Raman laser is required [24].

The ROC, as schematically shown in Figure 4-4, depends on the diameter Φ and height h of the micro-lens:

$$ROC = \frac{\Phi^2 + 4h^2}{8h} \quad (4-3)$$

Thus, to achieve the largest possible ROC, a large aspect ratio of diameter to height is needed. We targeted a diamond micro-lens of 400 μm in diameter which was chosen as a trade-off between the fabrication challenges described here and the usage of the sample area. This choice allows us to fit an 8×8 array of micro-lenses on the 4×4 mm² area of the diamond sample. Therefore, the maximum ROC of the micro-lens is determined by the achievable minimum height h of the micro-lens. Thus, diamond micro-lenses as shallow as possible with a diameter of 400 μm are desired. The following section 4.3 describes the fabrication process for such large ROC micro-lenses.

4.4 Fabrication of diamond micro-lenses with a large ROC

The sample used in this work was a 2 mm thick (corresponding to resonator length L), 4×4 mm² high purity single crystal CVD diamond from Element Six Ltd. The single crystal CVD diamond has a birefringence of $<1 \times 10^{-6}$.

To fabricate a shallow micro-lens in diamond using thermal resist reflow and ICP etching, two aspects are crucial: 1). a shallow and uniform micro-lens PR mask and 2). a low selectivity ICP etching to transfer the micro-lens PR mask to diamond. To fabricate a shallow and uniform micro-lens PR mask, there are two main issues. The first is the “edge bead effect” [39] which occurs when spin coating the PR on the surface of small samples (< 4 mm). This “edge bead effect” affects the uniformity of the spin coated PR and the control of the PR thickness. The second issue (described earlier) is the deformation of the PR pattern, namely the edge bulges, after reflow. This deformation happens due to insufficient surface tension especially when forming a big lens. The schematic of the diamond micro-lens fabrication process is illustrated in

Figure 4-5. The challenges during the fabrication of each step and their solution will be discussed in detail in Section 4.4.1.

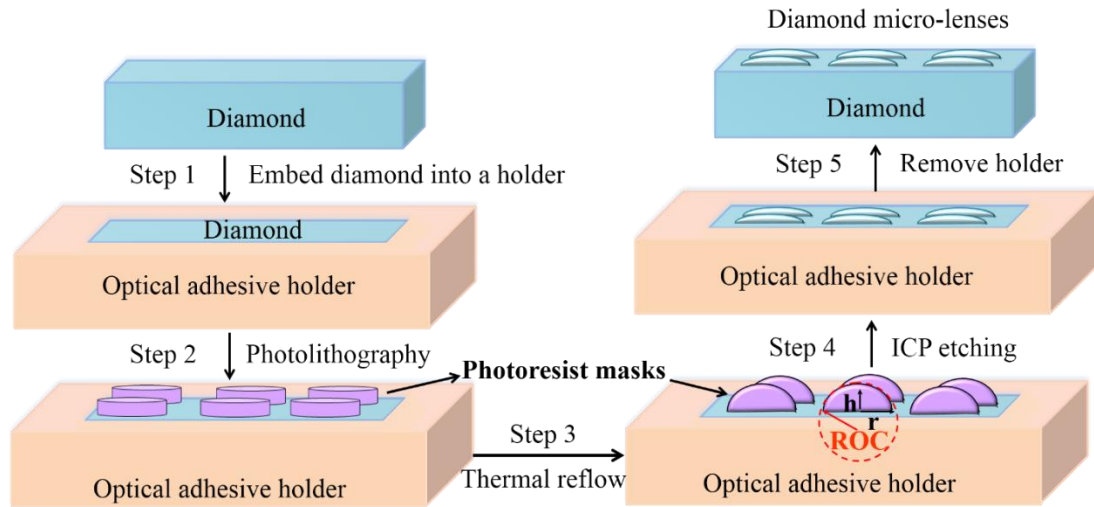


Figure 4-5: Schematic of the fabrication process of diamond micro-lenses.

4.4.1 Fabrication of large ROC PR micro-lens mask

4.4.1.1 “Edge bead effect”

The “edge bead effect” is a universal problem when spin coating PR on the surface of samples with small sizes (i.e. <5 mm; for samples with larger sizes the unwanted edge part can be cut off). During the PR spin coating, the centrifuge forces the PR to the edge of the sample surface. Under surface tension, the PR then forms a bead shape at the edge. A schematic of the “edge bead effect” and its influence is shown in Figure 4-6. Such an effect will degrade the uniformity of the PR layer and result in low pattern fidelity and compromise of the subsequent exposure and development process. This “edge bead effect” will become worse if a thick PR layer is used such as is the case here. The solution for this “edge bead effect” has been studied and different methods have been proposed. One is to jet PR dissolvable solutions (PR remover) at the edge of the sample [40]. This method has low controllability and needs extra complicated facilities. Another is using a different PR deposition technique other than spin coating, e.g. using a PR inkjet printing method as previously reported by Yanfeng Zhang et al. in our group [41]. However, only certain PR types (S1805 series from Shipley Ltd. in previous reports) can be used and limited PR patterns can be printed by this method and thus it is not suitable for our lens pattern fabrication. Here, a new method to solve this “edge bead effect” is developed with

very few extra steps involved. This method can be widely used to solve the issues of developing patterns on the small sample surface using lithography methods.

“Edge bead effect”

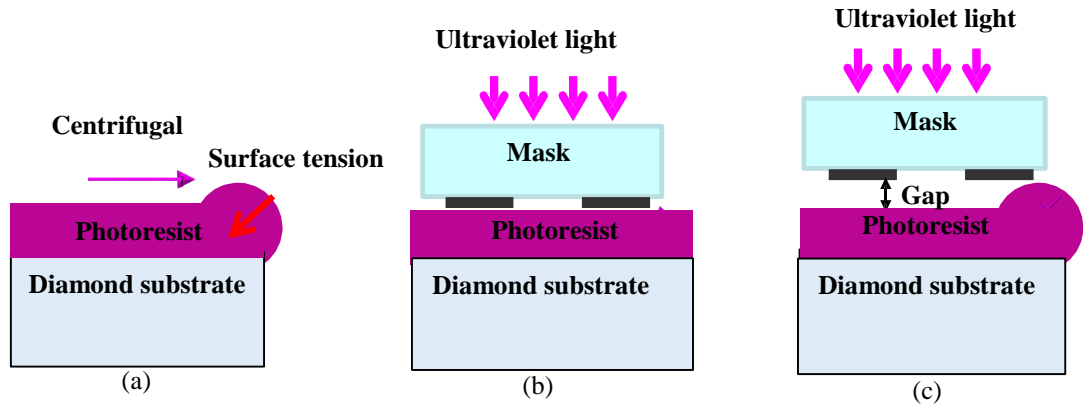


Figure 4-6: Schematic of the "edge bead effect": (a) PR bead formed at edge of the diamond sample after spin coating due to surface tension; (b) and (c) demonstrate the “edge bead effect” during lithography by comparing spin coated PR without and with “edge bead effect”.

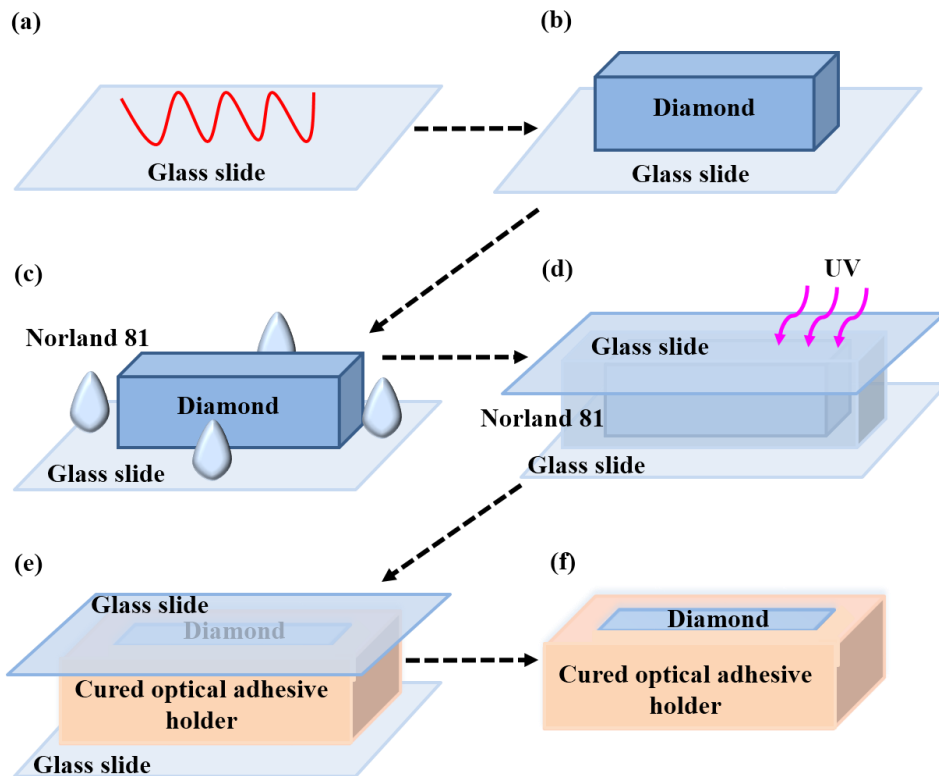


Figure 4-7: Schematic of the fabrication process of the optical adhesive holder.

To minimise the “edge bead effect”, we developed a UV curable polymer holder, which was made of Norland 81. A schematic of the developing progress of this UV

curable optical adhesive holder is shown in Figure 4-7. The process to create this holder is as follows. The diamond sample was first sandwiched between two glass slides, the surfaces of which were pre-coated with a thin layer of wax or primer. The purpose of the wax or primer was to aid the lift-off process from these glass slides. Then the sandwiched diamond sample was surrounded by the optical adhesive Norland 81. After a while, this liquid optical adhesive flowed and spread out to cover the diamond sample from the four sidewalls. The optical adhesive was then UV-cured to form the holder. By removing the glass slides (heating on a hotplate to melt the wax on the glass slides and sinking in acetone to dissolve the wax or primer), the holder was disengaged from the glass slides and a free-standing holder with the diamond embedded was obtained. This holder effectively extended the boundaries of the diamond and shifted the edge bead from the edge of the diamond to the holder. The edge bead on the holder was then cleaned using a cleanroom swab. This process is to ensure that the exposure process will not be affected by the edge bead when the photolithography mask approaches the PR layer. After removal of the edge bead, PR patterns developed on the diamond sample surface had a uniform pattern thickness using a standard lithography process. This optical adhesive holder can be removed after the ICP etching step by using an acid mixture of $\text{H}_2\text{SO}_4:\text{H}_2\text{O}_2$ with a ratio of 3:1 (piranha clean) within several minutes.

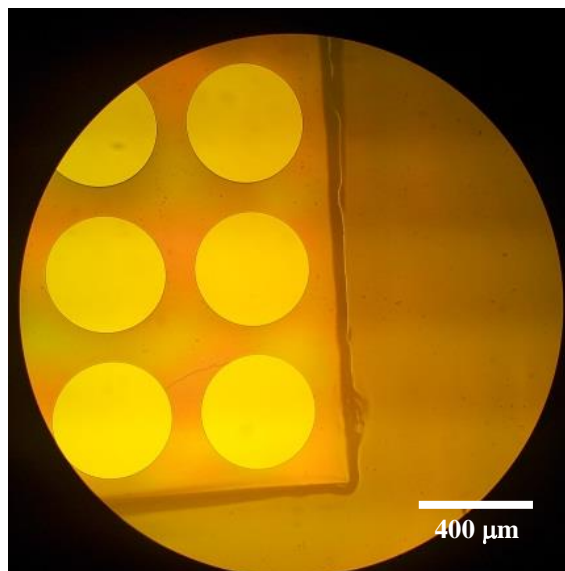


Figure 4-8: A plan view micrograph under the microscope demonstrating a uniform PR coating at the interface of the diamond and the holder.

As illustrated in Figure 4-7, such an optical adhesive holder is easy to fabricate (within 10 mins). The holder fabricated can be repeatedly used in a standard lithography process and was applied to the diamond micro-lens fabrication. Shipley 220 7.0 positive PR was spin coated with an optimised spin speed of 3400 rpm. Figure 4-8 shows the magnified image of the corner of diamond-holder sample after PR spin-coating. An even layer of PR across the border of the diamond and the holder surfaces can be clearly seen in Figure 4-8.

A Dektak surface profilometer was used to characterise the profiles of the spin coated PR, and a comparison between the spin coated PR profiles at the borders of the diamond surface without and with the holder is shown in Figure 4-9. The corresponding optical image of the surfaces of two PR spin-coated diamond samples is shown as an inset in Figure 4-9. It can be seen that the use of the holder greatly improves the uniformity of the spin coated PR layer and thus enlarges the usable area of the diamond sample surface

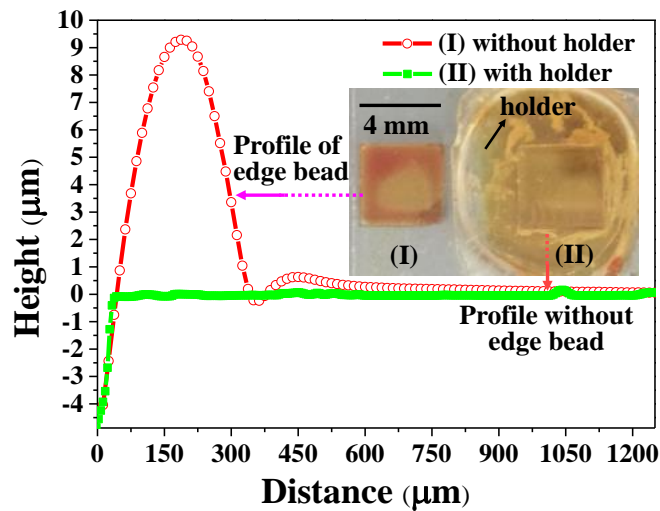


Figure 4-9: Measured profiles of the spin coated PR on surface of two diamond samples with and without a holder, demonstrating the effective removal of the edge bead. Inset is a plan view photograph of the surfaces of the PR spin coated diamond samples.

4.4.1.2 “Edge bulge effect”

During our experiments, edge bulges occurred when PR patterns were reflowed as has been discussed systematically in Chapter 3. It is found that at a certain reflow temperature, there is a minimum PR thickness above which the reflowed PR will form the desired micro-lens shape. It is desirable to fabricate micro-lenses using a PR layer close to the minimum thickness since this minimum thickness allows the minimum h

of the reflowed PR micro-lens, and hence the largest possible ROC at a certain diameter as expressed in Equation (4-3), Section 4.2. Based on the study in Chapter 3, an optimised PR thickness of 11.5 μm , which is close to the minimum thickness at a reflow temperature of 135 $^{\circ}\text{C}$, is used to provide a high uniformity and pattern fidelity of the lithographically-defined PR patterns. It is not possible to achieve such a PR thickness by spin coating only a single Shipley 220 7.0 PR layer and therefore a double-layer deposition was employed which gave a PR thickness of 14 μm under standard 3000 rpm spin speed. After pattern exposure/development and 3-minute reflow of the PR patterns on a hotplate under 135 $^{\circ}\text{C}$, a uniform array of PR micro-lenses was formed on the surface of the diamond sample. The resulting PR micro-lens had an ROC as large as 1.3 mm. Figure 4-10 shows the achieved PR micro-lens array on the diamond with a high uniformity and pattern fidelity. The PR micro-lenses were then transferred into diamond using an ICP etching via a multiplex ICP etch tool (SPTS Technologies Ltd.).

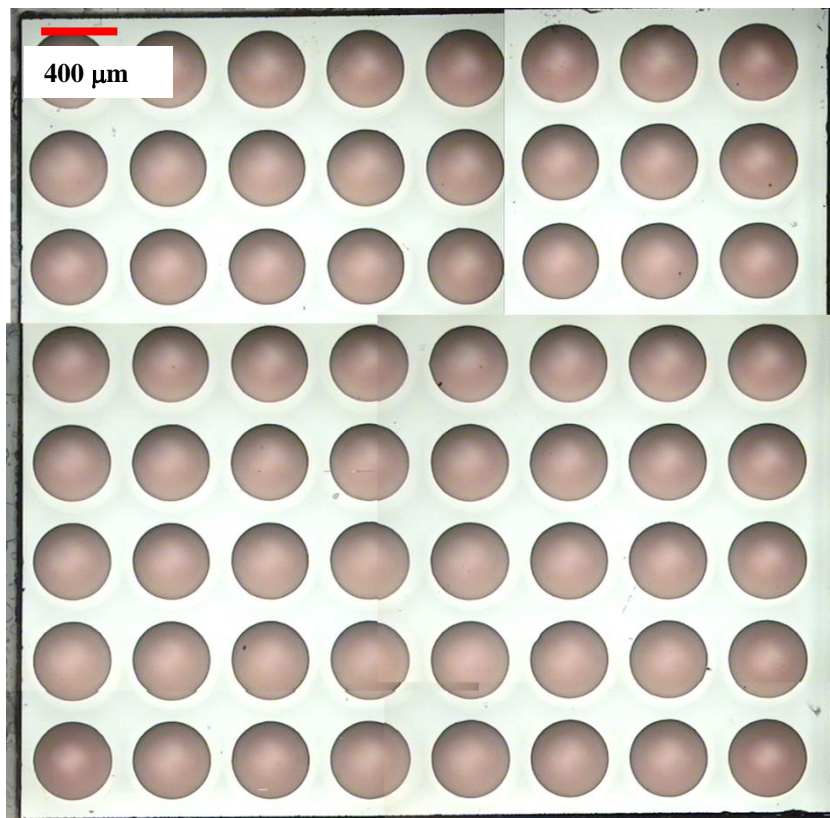


Figure 4-10: Achieved PR micro-lens array on the diamond surface with a high uniformity and pattern fidelity (stitched from multiple plan view images taken under the microscope with the same magnification).

4.4.2 Fabrication of large ROC diamond micro-lenses

ICP etching of diamond is conventionally performed using Ar/O₂ plasma as listed in Table 2-3, Chapter 2. However, the selectivity of this Ar/O₂ etch recipe, which is defined as the ratio of the etch rate of diamond to the etch rate of PR, is higher than 0.22 [29]. This selectivity limits the ROC of transferred diamond micro-lenses to less than 9 μm . Thus, an etch recipe with a lower selectivity is needed.

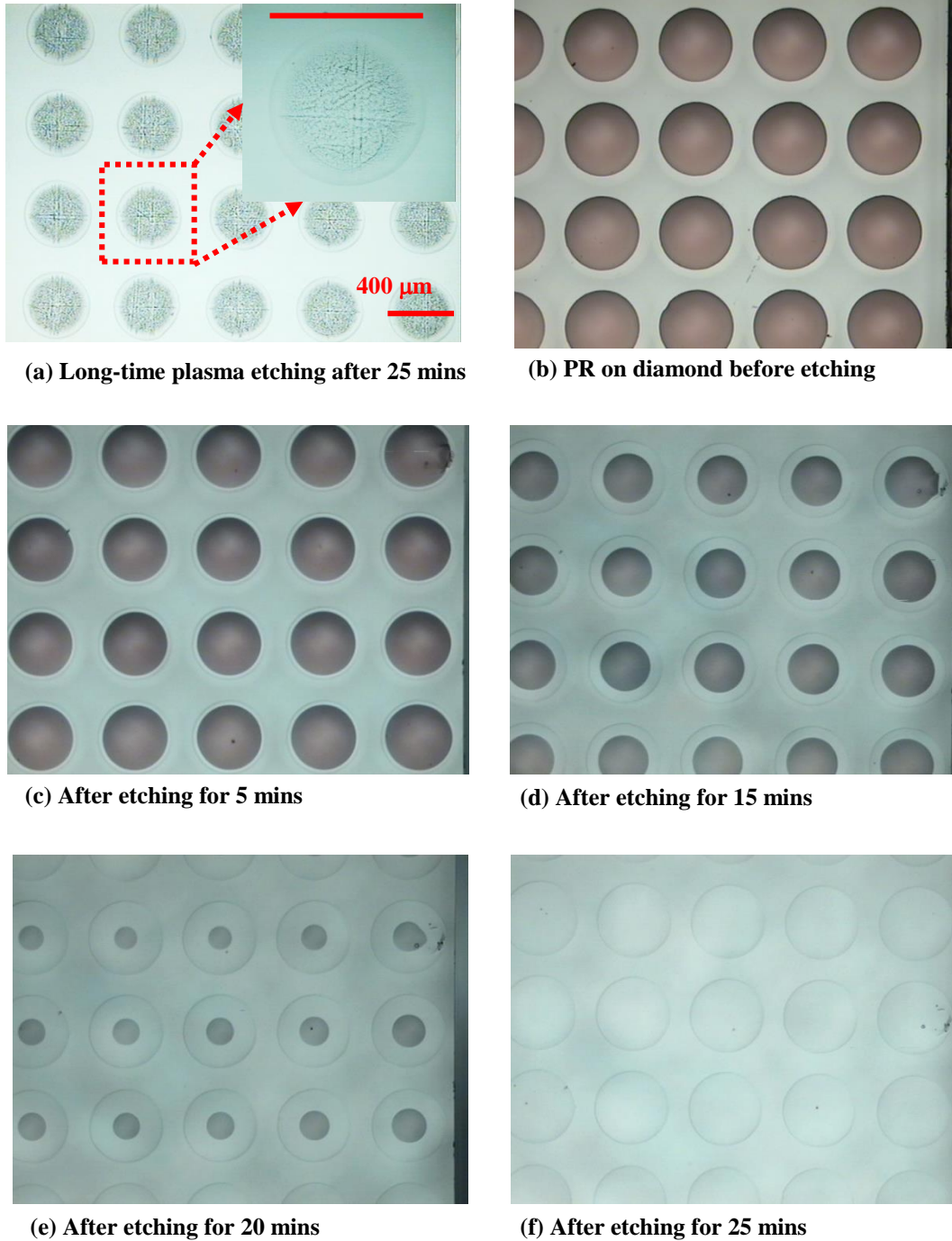


Figure 4-11: Plan view images of etched PR micro-lenses on diamond with different etching

methods and etching durations: (a) long time plasma etching after 25 mins and (b)-(f) five-step etching with 5 mins duration of each step, the scales of each image are the same as shown in (a) and the inset.

The chlorine-based diamond ICP etching chemistry developed by our group has a selectivity of 0.1, half that of the conventional Ar/O₂ etching under the same ICP conditions [42]. Transferring the micro-lens PR mask to diamond is therefore performed using ICP etching with an Ar/Cl₂ plasma. This enables a shallower etched structure and therefore a larger ROC of the resulting diamond micro-lens. The etch recipe as listed in Table 2-2 in Chapter 2 was used for the diamond etching. This recipe yields a diamond etch rate of 75 nm/min. The full transfer process of the PR pattern to diamond takes around 25 mins in total.

It is worth pointing out that a PR burning phenomenon was noticed which is due to excessive plasma etching induced overheating. The burned PR had a rough surface and this rough PR surface could be transferred to diamond during the subsequent plasma etching. It resulted in an unexpected rough diamond surface as shown in Figure 4-11 (a) and the magnified image inset. A multiple-step etching strategy was adapted to avoid this issue and 5 mins duration for each step was used which takes up to five etching steps in total as shown in Figure 4-11 (b)-(f). This strategy efficiently solved the PR burning issue and had a smooth etched surface as discussed in Section 4.4.

4.5 Results and discussion

4.5.1 Diamond micro-lenses

A diamond micro-lens array was etched onto one side of a 4×4 mm² by 2 mm thick single crystal diamond using the method described above. The fabricated diamond micro-lenses were characterised and then applied in a monolithic diamond Raman laser. Optical images of the fabricated large ROC diamond micro-lenses are shown in Figure 4-12.

The heights of these micro-lenses were measured to be 1.7 μm or less using a Dektak surface profilometer. Figure 4-13 (a) shows the measured profiles of three adjacent micro-lenses indicated by the black dotted arrow in Figure 4-12. These measured profiles have a uniform height and the ROCs of these micro-lenses is calculated to be 12 mm using Equation (4-3). Fitting with a semi-circle equation as

shown in Figure 4-13 (a) yields slightly larger ROCs of 13 mm or more. For this fit, only data points close to the centre of the micro-lenses were taken into account. This restriction of the fit region was made because the lens profiles deviate from a spherical shape at the bottom of the profiles. Since the laser mode is confined to a region close to the centre of the micro-lens, the ROC value obtained from this fit is more relevant than the one obtained by Equation (4-3). The deviation from the spherical shape results from the original high aspect ratio PR micro-lens and the subsequent low selectivity etching process and is not thought to influence the laser operation.

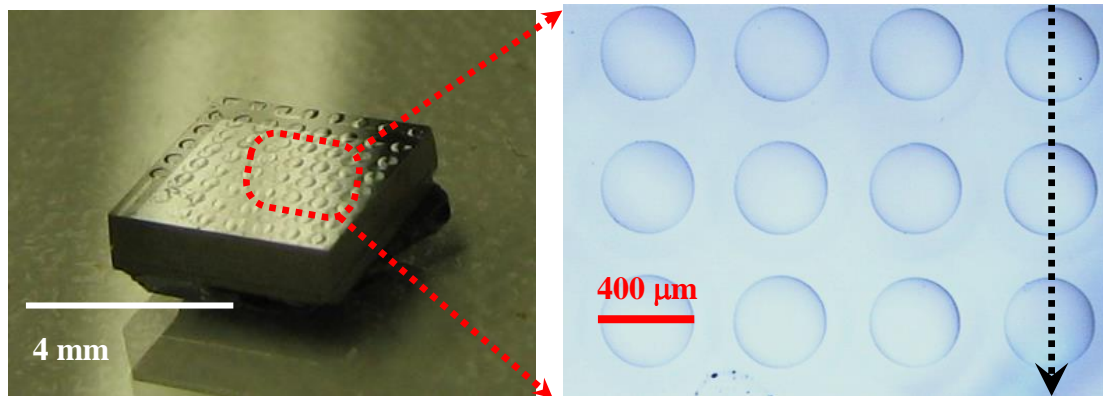


Figure 4-12: Optical images of fabricated diamond micro-lenses with large ROCs.

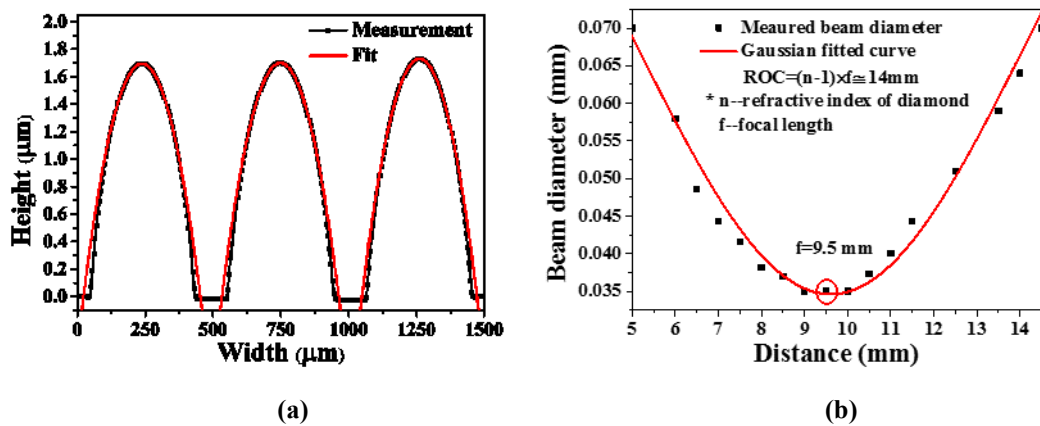


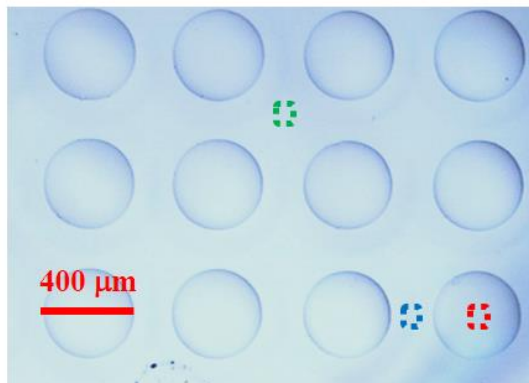
Figure 4-13: (a) Measured and fitted profiles of a column of fabricated diamond micro-lenses as shown in Figure 4-12 along the black dotted arrow and (b) focal length measurement of a representative diamond micro-lens fabricated with a height of 1.7 μm or less, distance being measured in reference to the place where diamond is located.

For further characterisation, the focal length of a representative diamond micro-lens was measured optically. The collimated beam from a He-Ne laser was passed through the micro-lens and the beam diameters were measured, as a function of position in reference to the place where the diamond lens was located, along the

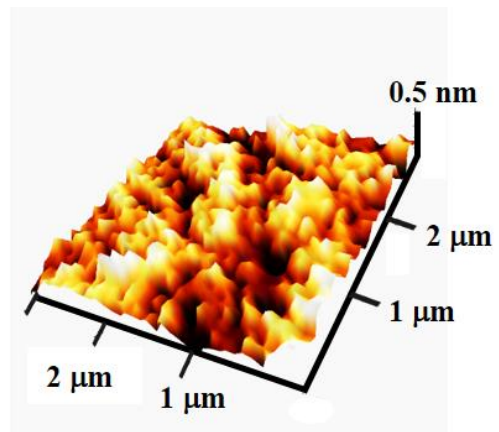
principal axis using the knife-edge technique [43]. The measurement yielded a focal length of 9.5 ± 0.5 mm as shown in Figure 4-13 (b). The ROC was then calculated using the thin lens approximation:

$$ROC \cong (n - 1) \times f \quad (4-4)$$

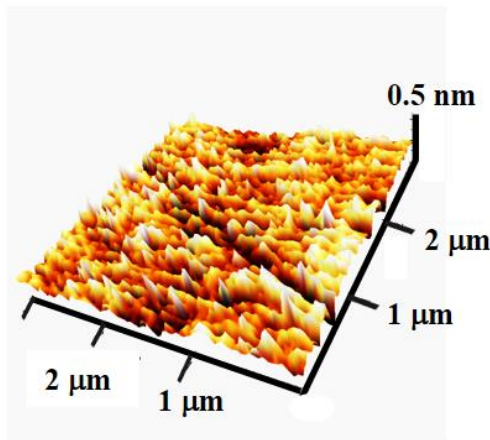
where n is the refractive index of the diamond (2.42) and f is the focal length. The ROC calculated from Equation (4-4) is 13.5 mm, which is consistent with the values obtained from the profile measurement.



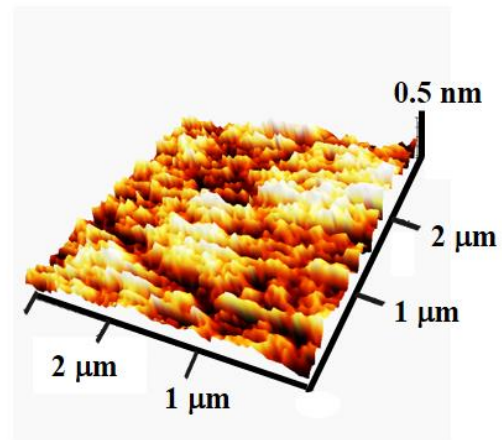
(a) Optical image of fabricated diamond lens array.



(b) Lens' top, red dashed square, $R_q = 0.180 \text{ nm}$ ($3 \times 3 \mu\text{m}^2$)



(c) Lens' bottom, blue dashed square $R_q = 0.130 \text{ nm}$ ($3 \times 3 \mu\text{m}^2$)



(d) Gap between lenses, green dashed square, $R_q = 0.150 \text{ nm}$ ($3 \times 3 \mu\text{m}^2$)

Figure 4-14: Characterisation of surface roughness of fabricated diamond micro-lenses: (a) image of the diamond micro-lens with AFM measured areas indicated by red, blue and green dashed squares, respectively; (b) measured RMS roughness at the top of the micro-lens, corresponding to the red-dashed square labelled area in (a); (c) measured RMS roughness at the bottom of the micro-lens, corresponding to the blue-dashed square labelled area in (a) and (d) measured RMS roughness at the gap between micro-lenses, corresponding to the green-dashed square labelled area in (a).

Atomic force microscopy (AFM) measurement shows that the diamond micro-lenses have a RMS roughness of around 0.18 nm on an area of $3 \times 3 \mu\text{m}^2$. The measurements were taken on areas of the lens top (red dotted square), lens bottom (blue dotted square) and the gap between two micro-lenses (green dotted square) as shown in Figure 4-14 (a). All AFM measurements taken at different areas demonstrated a consistent RMS roughness of etched diamond micro-lens surface as shown in Figure 4-14. The obtained micro-lens roughness value was comparable to the value reported by Lee et al. [42] and the work reported by M. Karlsson et al. [30].

Removal of polished marks

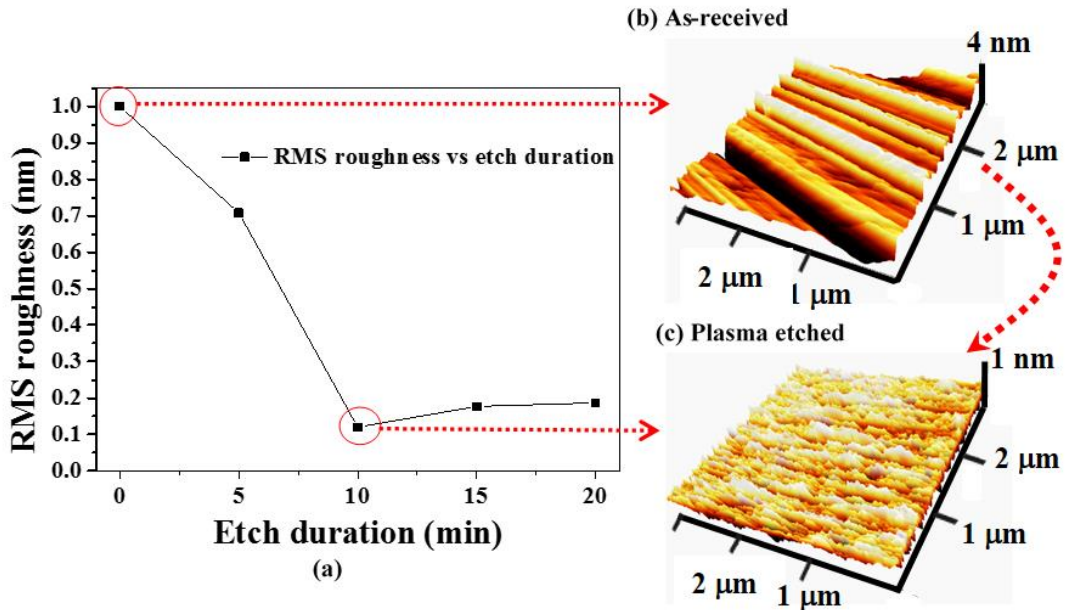


Figure 4-15: (a) RMS roughness of Ar/Cl₂ plasma etched diamond surface as a function of etch durations and corresponding measured surfaces taken at (b) surface of the as-received diamond sample and (c) surface after plasma etching for 10 mins.

The as-received diamond surface was measured to have a RMS roughness of around 1 nm. In order to determine the influence of the etching on the diamond surface, the RMS roughness of the etched diamond surfaces was measured as a function of the etch duration as shown in Figure 4-15 (a). It can be seen that the measured roughness was reduced from 1 nm, as received, to less than 0.2 nm after 10 minutes etching. This result is consistent with the “surface smoothing effect” of Ar/Cl₂ plasma etching reported by Lee et al. [42]. It is worth pointing out that the polishing marks on the as-received diamond surface, which are groove-like features as shown in the Figure 4-15 (b), have been removed after the Ar/Cl₂ etching as shown in Figure 4-15 (c). This

removal of the polishing-mark contributes to the smoother surface and smaller RMS surface roughness value after etching. Such a smooth surface is important for the following mirror coating step so as to form a high quality laser resonator.

4.5.2 Micro-lensed monolithic diamond Raman lasers

By depositing the appropriate mirrors on both sides of the lensed diamond, a monolithic diamond Raman laser was achieved. The diamond resonators were pumped with an Elforlight SPOT laser emitting Q-switched pulses at 532 nm with pulse durations of 1.5 ns and pulse repetition rates of 10 kHz.

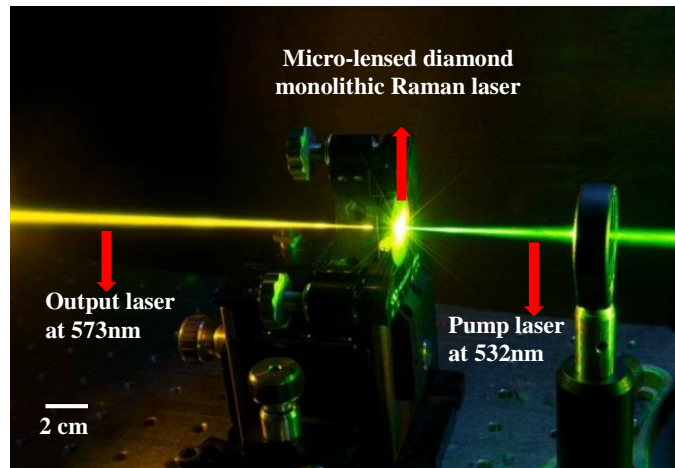


Figure 4-16: Demonstration of the monolithic diamond Raman laser based on the micro-lens resonator using a pulsed laser of 1.5 ns duration at a pump pulse energy of 1.5 μJ .

The pump was attenuated using a combination of a half wave-plate and a polarizing cube. It was then focused using a 50 mm focal length lens and through a single micro-lens onto the back surface of the diamond. This resulted in a pump spot radius of 9 μm . The micro-lens cavity had a fundamental mode radius of 24 μm as calculated using Equation (4-2). The pump light propagated along a $\langle 110 \rangle$ direction and was polarized along a $\langle 100 \rangle$ direction in the diamond. An image of the resulting compact and robust monolithic diamond Raman laser in operation is shown in Figure 4-16.

A Raman conversion of the green pump at 532 nm to the yellow at 573 nm occurred when the pump pulse energy reached 1.5 μJ . Figure 4-17 demonstrates the generated Raman output spectrum with 1st, 2nd and 3rd Raman Stokes wavelengths presented. Due to the limit of a resolution of 0.13nm, sub-structures in the peaks were unable to be resolved.

The converted energy of the 1st, 2nd and 3rd Stokes orders together with the combined Raman output was measured as shown in Figure 4-18 (a). A pump to combined Raman conversion efficiency (the ratio between the energy output and the input) was measured as shown in Figure 4-18 (b). The pump to combined Raman conversion efficiency was measured to be as high as 84% at the maximum pump pulse energy of 16 μJ .

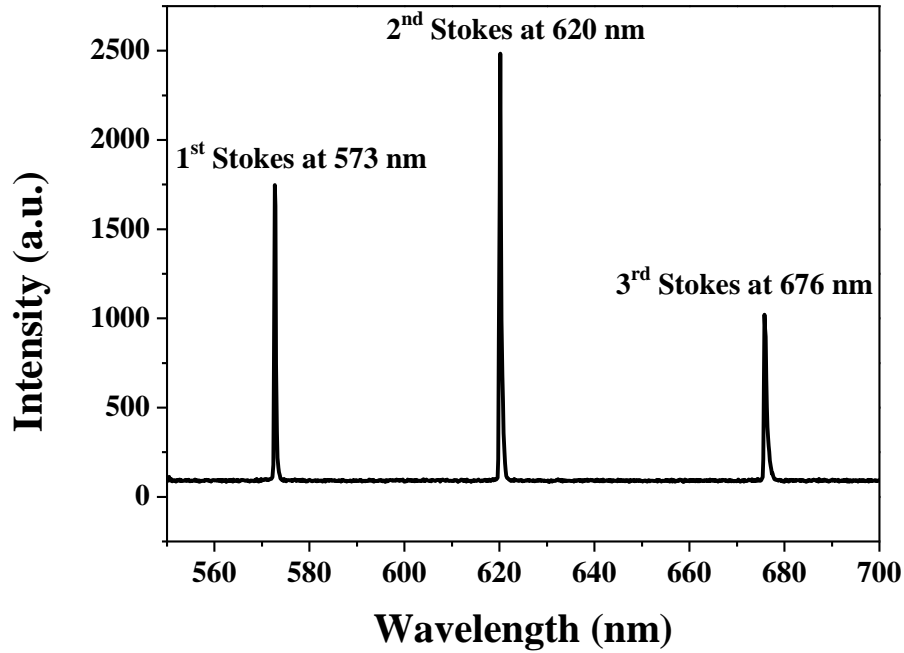


Figure 4-17: Typical generated Raman shift spectrum with 1st and 2nd Stokes wavelengths being presented.

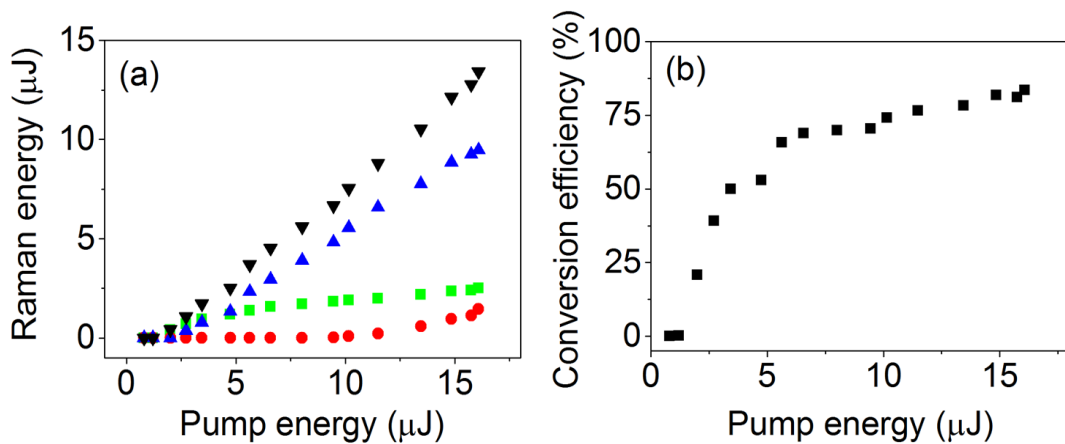


Figure 4-18: (a) Energy transfer characteristics for the 1st (green squares), 2nd (blue triangles), and 3rd Stokes orders (red circles) and the combined Raman output (inverted black triangles) of the micro-lensed monolithic diamond Raman laser and (b) the conversion efficiency from pump to combined Raman.

The maximum average powers of the combined Raman outputs were measured to be 134 mW. This result is comparable to a conventional diamond Raman laser pumped at this energy level. The detailed laser characterisation and performance was reported in [24].

At a pulse duration of ~ 1.2 ns at the low pump powers was measured as shown in Figure 4-19 (a). Only the 1st Stokes is above threshold at this pump. At maximum pump power however, the 1st Stokes pulse duration was measured to be 3.2ns as shown in Figure 4-19 (b). The 1st Stokes pulse at high pump power is longer than expected. A measurement is taken of the depleted pump with a FWHM of 2.4ns, which might be the reason of this longer 1st Stokes pulse at high pump power [24].

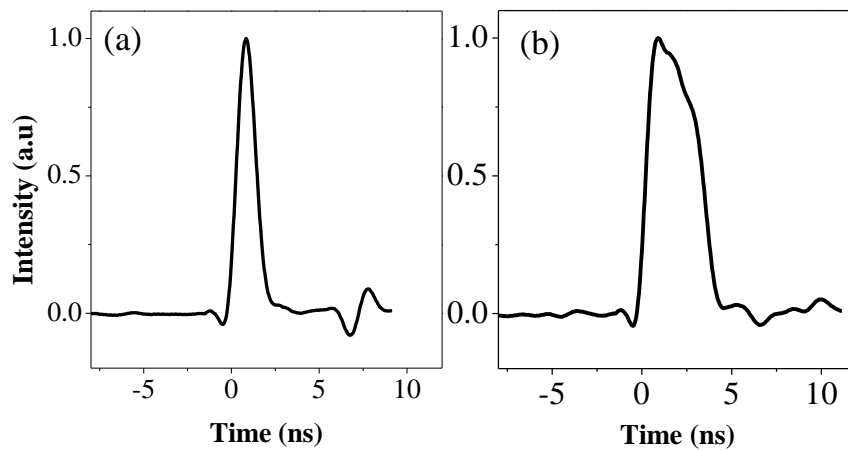


Figure 4-19: 1st Stokes pulses at 573nm (a) below threshold of 2nd Stokes and (b) at maximum pump power with both 2nd and 3rd Stokes oscillating.

As diamond is transparent over a larger range of wavelengths, by depositing the appropriate mirror coatings on the facets of the micro-lensed resonator, and using different pump lasers, it should be possible to operate such monolithic diamond Raman lasers over a wide wavelength range. The large ROC diamond micro-lenses fabricated here may also be used for application in higher power monolithic semiconductor disk lasers [3]. The technique developed in this work can further be used to fabricate diamond micro-lenses with even larger ROCs with a bigger lens diameter than the ones reported here. Moreover, this technique might also find use in developing other diamond components such as solid immersion lenses for photon collection [34, 44] and aspheric lenses.

4.6 Conclusion

In this chapter, the fabrication of diamond micro-lenses with large ROCs using PR thermal reflow and ICP etching was discussed. This is done by using a novel diamond micro-lens fabrication process. This fabrication process includes the development of an optical adhesive holder which is used to solve the “edge bead effect” during PR spin coating and control of the PR pattern reflow to form a micro-lens PR mask at its largest possible ROC with diameter of 400 μm and the final transfer of PR micro-lens mask to diamond to form diamond micro-lenses with large ROC using a low selectivity diamond etching recipe-the Ar/Cl₂ plasma etching. Diamond micro-lenses with large ROCs of 13 mm or more were achieved as a result. The ROCs of these diamond micro-lenses were measured and confirmed by profilometry and optical measurements. These diamond micro-lenses have a very smooth surface of 0.18 nm root-mean-square roughness. By mirror coating these diamond micro-lenses, a resonator is formed which enables compact and robust monolithic diamond Raman lasers with high conversion efficiency.

References

- [1] W. Koechner, Thermal Lensing in a Nd:YAG Laser Rod, *Applied Optics*, **9**, 2548 (1970).
- [2] N. Ter-Gabrielyan, V. Fromzel, M. Dubinskii, Linear thermal expansion and thermo-optic coefficients of YVO₄ crystals the 80-320 K temperature range, *Optical Materials Express*, **2**, 1624 (2012).
- [3] N. Laurand, C.L. Lee, E. Gu, S. Calvez, M.D. Dawson, Power-Scaling of Diamond Microlensed Microchip Semiconductor Disk Lasers, *IEEE Photonics Technology Letters*, **21**, 152 (2009).
- [4] N. Laurand, C.L. Lee, E. Gu, J.E. Hastie, S. Calvez, M.D. Dawson, Microlensed microchip VECSEL, *Optics Express*, **15**, 9341 (2007).
- [5] K.E. Goodson, K. Kurabayashi, R.F.W. Pease, Improved heat sinking for laser-diode arrays using microchannels in CVD diamond, *Components, Packaging, and Manufacturing Technology, IEEE Transactions on Advanced Packaging*, **20**, 104 (1997).
- [6] C. Po Han, L. Ching Liang, Y.K. Liu, C. Te Yuan, L. Cheng-Yi, Diamond Heat Spreader Layer for High-Power Thin-GaN Light-Emitting Diodes, *IEEE Photonics Technology Letters*, **20**, 845 (2008).
- [7] A.J. Trindade, B. Guilhabert, E.Y. Xie, R. Ferreira, J.J.D. McKendry, D. Zhu, N. Laurand, E. Gu, D.J. Wallis, I.M. Watson, C.J. Humphreys, M.D. Dawson, Heterogeneous integration of gallium nitride light-emitting diodes on diamond and silica by transfer printing, *Optics Express*, **23**, 9329 (2015).
- [8] R. Mildren, J. Rabeau, *Optical Engineering of Diamond*, Wiley, (2013).

-
- [9] A. Tallaire, A.T. Collins, D. Charles, J. Achard, R. Sussmann, A. Gicquel, M.E. Newton, A.M. Edmonds, R.J. Cruddace, Characterisation of high-quality thick single-crystal diamond grown by CVD with a low nitrogen addition, *Diamond and Related Materials*, **15**, 1700 (2006).
- [10] S.E. Coe, R.S. Sussmann, Optical, thermal and mechanical properties of CVD diamond, *Diamond and Related Materials*, **9**, 1726 (2000).
- [11] V.G. Savitski, S. Reilly, A.J. Kemp, Steady-State Raman Gain in Diamond as a Function of Pump Wavelength, *IEEE Journal of Quantum Electronics*, **49**, 218 (2013).
- [12] R.P. Mildren, J.E. Butler, J.R. Rabeau, CVD-diamond external cavity Raman laser at 573 nm, *Optics Express*, **16**, 18950 (2008).
- [13] I. Friel, S.L. Geoghegan, D.J. Twitchen, G.A. Scarsbrook, Development of high quality single crystal diamond for novel laser applications, **7838**, 783819-1 (2010).
- [14] V.G. Savitski, I. Friel, J.E. Hastie, M.D. Dawson, D. Burns, A.J. Kemp, Characterization of Single-Crystal Synthetic Diamond for Multi-Watt Continuous-Wave Raman Lasers, *IEEE Journal of Quantum Electronics*, **48**, 328 (2012).
- [15] A.D. Greentree, S. Praver, Yellow lasers: A little diamond goes a long way, *Nature Photonics*, **4**, 202 (2010).
- [16] G. Eckhardt, D.P. Bortfeld, M. Geller, Stimulated emission of stokes and anti-stokes raman lines from diamond, calcite, and α -sulfur single crystals, *Applied Physics Letters*, **3**, 137 (1963).
- [17] A.A. Kaminskii, V.G. Ralchenko, V.I. Konov, Observation of stimulated raman scattering in CVD-diamond, *Journal of Experimental and Theoretical Physics Letters*, **80**, 267 (2004).
- [18] W. Lubeigt, V.G. Savitski, G.M. Bonner, S.L. Geoghegan, I. Friel, J.E. Hastie, M.D. Dawson, D. Burns, A.J. Kemp, 1.6 W continuous-wave Raman laser using low-loss synthetic diamond, *Optics Express*, **19**, 6938 (2011).
- [19] J.-P.M. Feve, K.E. Shortoff, M.J. Bohn, J.K. Brasseur, High average power diamond Raman laser, *Optics Express*, **19**, 913 (2011).
- [20] R.J. Williams, O. Kitzler, A. McKay, R.P. Mildren, Investigating diamond Raman lasers at the 100W level using quasi-continuous-wave pumping, *Optics Letters*, **39**, 4152 (2014).
- [21] W. Lubeigt, J. Gomes, G. Brown, A. Kelly, V. Savitski, D. Uttamchandani, D. Burns, Control of solid-state lasers using an intra-cavity MEMS micromirror, *Optics Express*, **19**, 2456 (2011).
- [22] O. Kitzler, A. McKay, R.P. Mildren, Continuous-wave wavelength conversion for high-power applications using an external cavity diamond Raman laser, *Optics Letters*, **37**, 2790 (2012).
- [23] I. Aharonovich, A.D. Greentree, S. Praver, Diamond photonics, *Nature Photonics*, **5**, 397 (2011).
- [24] S. Reilly, V.G. Savitski, H. Liu, E. Gu, M.D. Dawson, A.J. Kemp, Monolithic diamond Raman laser, *Optics Letters*, **40**, 930 (2015).
- [25] S. Castelletto, J.P. Harrison, L. Marseglia, A.C. Stanley-Clarke, B.C. Gibson, B.A. Fairchild, J.P. Hadden, Y.L.D. Ho, M.P. Hiscocks, K. Ganesan, S.T. Huntington, F. Ladouceur, A.D. Greentree, S. Praver, J.L. O'Brien, J.G. Rarity, Diamond-based structures to collect and guide light, *New Journal of Physics*, **13**, 1 (2011).

- [26] J.P. Hadden, J.P. Harrison, A.C. Stanley-Clarke, L. Marseglia, Y.L.D. Ho, B.R. Patton, J.L. O'Brien, J.G. Rarity, Strongly enhanced photon collection from diamond defect centres under microfabricated integrated solid immersion lenses, *Applied Physics Letters*, **97**, 1 (2010).
- [27] M. Werner, R. Locher, Growth and application of undoped and doped diamond films, *Reports on Progress in Physics*, **61**, 1665 (1998).
- [28] H.W. Choi, E. Gu, C. Liu, C. Griffin, J.M. Girkin, I.M. Watson, M.D. Dawson, Fabrication of natural diamond microlenses by plasma etching, *Journal of Vacuum Science & Technology B*, **23**, 130 (2005).
- [29] E. Woerner, C. Wild, W. Mueller-Sebert, P. Koidl, CVD-diamond optical lenses, *Diamond and Related Materials*, **10**, 557 (2001).
- [30] M. Karlsson, F. Nikolajeff, Diamond micro-optics: microlenses and antireflection structured surfaces for the infrared spectral region, *Optics Express*, **11**, 502 (2003).
- [31] E. Gu, H.W. Choi, C. Liu, C. Griffin, J.M. Girkin, I.M. Watson, M.D. Dawson, G. McConnell, A.M. Gurney, Reflection/transmission confocal microscopy characterization of single-crystal diamond microlens arrays, *Applied Physics Letters*, **84**, 2754 (2004).
- [32] W.G.M. Nelissen, H.P. Godfried, E.P. Houwman, P.A.C. Kriele, J.C. Lamers, G.J. Pels, B.M. Van Oerle, P.G.H.M. Spaay, M.R. McClymont, C.J.H. Wort, Google Patents, (2012).
- [33] P. Siyushev, F. Kaiser, V. Jacques, I. Gerhardt, S. Bischof, H. Fedder, J. Dodson, M. Markham, D. Twitchen, F. Jelezko, J. Wrachtrup, Monolithic diamond optics for single photon detection, *Applied Physics Letters*, **97**, 241902 (2010).
- [34] J.P. Hadden, J.P. Harrison, A.C. Stanley-Clarke, L. Marseglia, Y.-L.D. Ho, B.R. Patton, J.L. O'Brien, J.G. Rarity, Strongly enhanced photon collection from diamond defect centres under microfabricated integrated solid immersion lenses, *Applied Physics Letters*, **97**, 241901 (2010).
- [35] L. Marseglia, J.P. Hadden, A.C. Stanley-Clarke, J.P. Harrison, B. Patton, Y.-L.D. Ho, B. Naydenov, F. Jelezko, J. Meijer, P.R. Dolan, J.M. Smith, J.G. Rarity, J.L. O'Brien, Nanofabricated solid immersion lenses registered to single emitters in diamond, *Applied Physics Letters*, **98**, 133107 (2011).
- [36] H. Bernien, L. Childress, L. Robledo, M. Markham, D. Twitchen, R. Hanson, Two-Photon Quantum Interference from Separate Nitrogen Vacancy Centres in Diamond, *Physical Review Letters*, **108**, 043604 (2012).
- [37] L. Robledo, L. Childress, H. Bernien, B. Hensen, P.F.A. Alkemade, R. Hanson, High-fidelity projective read-out of a solid-state spin quantum register, *Nature*, **477**, 574 (2011).
- [38] Z.D. Popovic, R.A. Sprague, G.A. Connell, Technique for monolithic fabrication of microlens arrays, *Applied Optics*, **27**, 1281 (1988).
- [39] T. Dobroth, L. Erwin, Causes of Edge Beads in Cast Films, *Polymer Engineering & Science*, **26**, 462 (1986).
- [40] J.E. Oberlander, E.S. Sison, C. Traynor, J. Griffin, Development of an edge bead remover (EBR) for thick films, *Proc. SPIE*, **4345**, 475 (2001).

- [41] Y. Zhang, L. McKnight, Z. Tian, S. Calvez, E. Gu, M.D. Dawson, Large cross-section edge-coupled diamond waveguides, *Diamond and Related Materials*, **20**, 564 (2011).
- [42] C.L. Lee, E. Gu, M.D. Dawson, I. Friel, G.A. Scarsbrook, Etching and micro-optics fabrication in diamond using chlorine-based inductively-coupled plasma, *Diamond and Related Materials*, **17**, 1292 (2008).
- [43] A.E. Siegman, M.W. Sasnett, T.F. Johnston, Choice of clip levels for beam width measurements using knife-edge techniques, *IEEE Journal of Quantum Electronics*, **27**, 1098 (1991).
- [44] W. Pfaff, B.J. Hensen, H. Bernien, S.B. van Dam, M.S. Blok, T.H. Taminiau, M.J. Tiggelman, R.N. Schouten, M. Markham, D.J. Twitchen, R. Hanson, Unconditional quantum teleportation between distant solid-state quantum bits, *Science*, **345**, 532 (2014).

Chapter 5 Diamond membranes and their applications to quantum information processing

In this chapter, the development of large area, high purity, single crystal diamond membranes with submicron thickness is introduced. The diamond membranes are critical components for open optical cavity coupling in applications to scalable quantum information processing. The NV colour centre in the diamond membrane, its application to cavity-coupling in quantum technologies and a review of the diamond membrane fabrication are introduced in Section 5.1. The challenges of the development of large area, ultrathin diamond membranes and the details of the process development are discussed in Section 5.2. Characterisation of the diamond membranes in terms of their thickness and surface quality are described in Section 5.3. A discussion of the NV emission in the diamond membrane applied to optical cavity coupling is presented in Section 5.4. Some other potential implementations of diamond membranes are described at the end of Section 5.4. A conclusion of the work shown in this chapter is then given in Section 5.5.

5.1 Introduction

Diamond membranes and platelets are currently in high demand [1]. They can be used for X-ray windows [2], radiation detection [3, 4], and micro-electric-mechanical-system/nano-electric-mechanical-system (MEMS/NEMS) [5], for example. Additionally, they are required for the development of high quality optical and photonic devices [6]. Micro/nano photonic devices such as nano-beam cavities[7], nanopillar waveguides [8] or ring resonators [9] have been fabricated based on diamond membranes. In particular, submicron thick high quality, large area, free-standing single crystal diamond membranes with colour centres in them, e.g. NV centres, could be used to provide single photon sources for quantum technologies such as quantum communication [10], quantum cryptography [11], quantum sensing [12] and quantum computation [13].

Quantum computation, which utilises quantum bits (qubits) as the basic information elements instead of the electronic bits used in conventional computers, offers much to physics and computer science in the 21th century. There are several

protocols that are promising to realise quantum computation in reality: ion traps, nuclear magnetic resonance (NMR), optical photons and optical cavity quantum electrodynamics (cavity-QED) [14].

5.1.1 Cavity-coupled NV in diamond membrane

Cavity-QED describes how atoms and light interact in cavities and is one of the most promising ways to realise quantum computation using qubits of cavity-coupled atoms. Cavity-QED has been the focus of much research in the last decade. However, to realise quantum computation using cavity-QED, single atoms and single photons are necessary. In particular, single atoms with quantum states that can be initialised, manipulated and subsequently readout are essential [14]. For such a single ‘atom’ and single photon system, the diamond NV centre is a promising candidate to realise cavity-QED as has been introduced in Chapter 1.

To harness the full potential of the NV centre in diamond for emerging quantum technologies requires both stronger ‘atom’-photon interaction and enhanced emission from these centres at the zero phonon line (ZPL). Cavity coupling the NV centre emission offers an ideal solution for the above requirements.

The behaviour of cavity-coupled ‘atom’-photon interactions is described by cavity-QED. When matched to a cavity with the appropriate cavity mode, both the interaction between the NV centre and the emitted photons and the spontaneous emission rate from the ZPL can be enhanced within the resonant cavity. This is because in an optical cavity, only optical waves with particular wavelengths that satisfy the relation in Equation (5-1) can resonate. If the ZPL emission wavelength is in-resonance, the interference between photons at the mirrors is constructive. Thus, the ZPL emission is preserved and enhanced in the cavity. The emissions at other wavelengths, however, interfere destructively at the mirror and thus are suppressed. The requirement for cavity-enhanced emission is expressed as:

$$L_{cav} = \frac{m\lambda}{2n} \quad (5 - 1)$$

where L_{cav} denotes the cavity length and m denotes an integer number, λ denotes the wavelength in vacuum and n denotes the refractive index of the medium in the cavity.

To quantify the enhancement effect of spontaneous emission from the atom-photon interaction in the cavity, the Purcell factor is used. In a cavity, the atom is first stimulated by an external source such as a pulsed laser. Then the atom emits photons in the way described in Chapter 1. The emitted photons are bounced back and forwards inside the cavity until absorbed by the atom again or coupled out from the cavity. This atom-photon interaction is enhanced if the coupling strength (g) is larger than the losses from both the coupling out loss rate κ and the non-resonant decay rate γ as shown in Figure 5-1. The spontaneous emission rate from the atom is enhanced when the emission matches the resonance mode and the dipoles are orientated along the field direction. This phenomenon is called the Purcell effect. To quantify the enhanced spontaneous emission, the following Equation applies:

$$F_p = \frac{g^2}{\gamma\kappa} = \frac{3Q \left(\frac{\lambda}{n}\right)^3}{4\pi^2 V_0} > 1 \quad (5 - 2)$$

where F_p denotes the Purcell factor, Q denotes the quality factor (see discussion on page 122), and V_0 denotes the cavity volume. The reference [23] presents the detail of how this Purcell equation is derived.

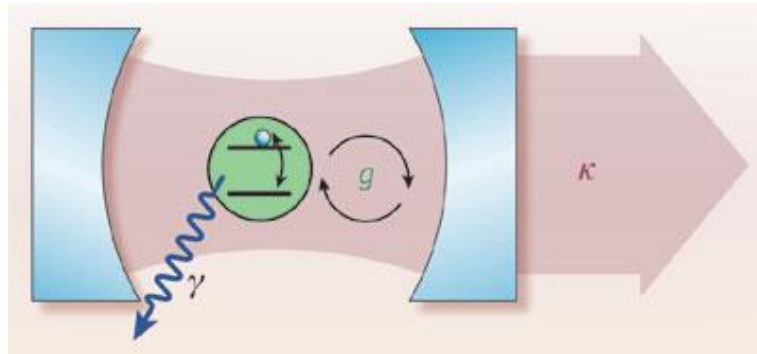


Figure 5-1: Schematic of cavity-quantum electrodynamics [25].

The benefits of coupling the diamond NV centres in the cavity are threefold: 1). the interactions between the NV centres and the photons are enhanced; 2). the spontaneous emission rate of the NV centre at the ZPL is enhanced; and 3). the lifetime of the NV centre is shortened so that the NV can emit photons at a higher rate. This paves the way for efficient use of the qubits that come from these atoms and photons in QIP.

Different schemes have been proposed so far to cavity-couple the NV centre in order to enhance the emission [9, 26-29]. Among these schemes, an “open” optical

cavity-coupling of the NV centre that offers flexible tuning of the cavity mode to be resonant with the NV emission to enhance the emission in the ZPL is promising [30, 31]. Compared to other methods of cavity tuning, this open optical cavity approach offers more flexible tuning of the cavity resonance mode via controlling the distance between the two mirrors with piezo actuators. This open optical cavity can be accurately tuned to match the resonant wavelength with the NV centre ZPL without degrading the cavity quality.

To optimise the coupling in the open optical cavity, two basic conditions should be satisfied: the cavity needs to have a high quality factor (Q-factor) and the cavity volume should be as low as possible. The quality factor of a cavity is determined by the loss of the dielectric cavity mirrors when the photons are reflected by these mirrors. The cavity volume is decided by the ROC as well as the distance between the cavity mirrors.

NV centre (in nano-diamonds) coupling was demonstrated recently using this open optical cavity approach. In this cavity, the ROC and the distance between the cavity mirrors were $7.6 \mu\text{m}$ and $1.11 \mu\text{m}$, respectively, providing a cavity volume of $1.24 \mu\text{m}^3$. The results show that the broad sideband emissions of the NV centre were suppressed while the spontaneous emission from the ZPL was enhanced by a factor of 6.25 in resonance with the cavity.

Nevertheless, due to the poor controllability of the NV centres in nano-diamonds, single crystal diamond membranes that contain single NV centres are highly desired for cavity-enhanced emission. Especially, the NV centres can be created at particular positions in diamond membranes by ion implantation, a feature which is essential for networked QIP. To couple NV emissions from a diamond membrane into the open optical cavity, the diamond membrane located between the two cavity mirrors needs to be as thin as possible so as to achieve a cavity with a small volume. Our work to develop the ultrathin (thickness $< 1 \mu\text{m}$) single crystal diamond membranes for QIP applications is described in this chapter. The open optical cavity used to enhance NV centre emissions from the diamond membrane is shown in Figure 5-2. This open cavity consists of a planar mirror and a curved mirror to form the cavity as depicted in Figure 5-2 (a). A diamond membrane with NV centres is placed on top of the planar mirror. An SEM image of the curved concave mirrors is shown in Figure 5-2 (b).

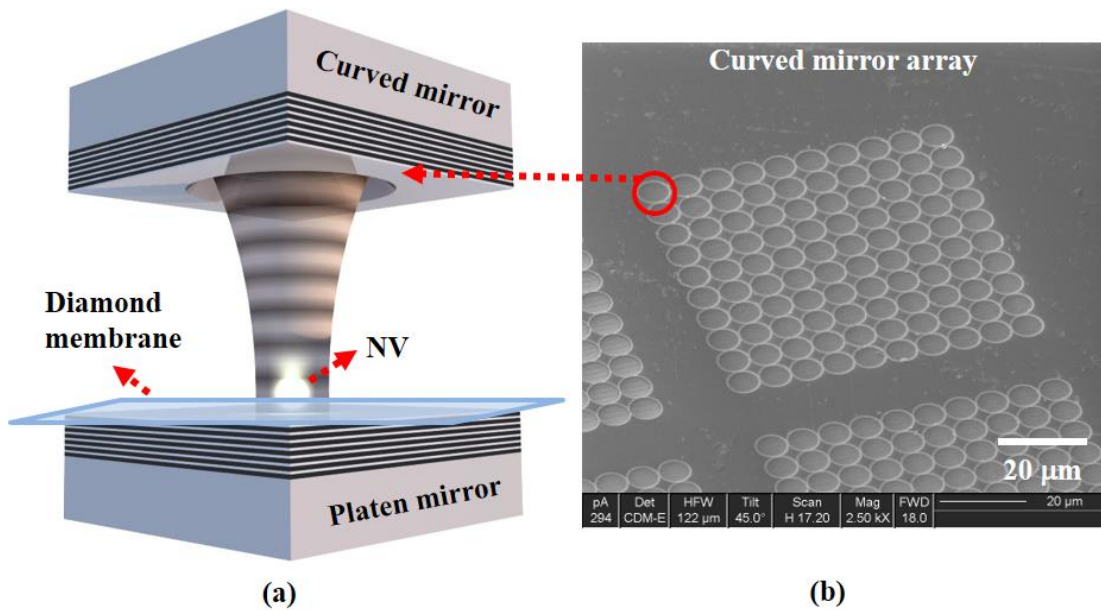


Figure 5-2: (a) Schematic of the open-optical mirror cavity with coupled NV centres in the diamond membrane and (b) an SEM of the curved mirror cavity fabricated using focused ion beam (FIB) milling. Images courtesy: Photonic Nanomaterials Group, University of Oxford [30].

Thus, an ultrathin high purity diamond membrane is highly desired to achieve cavity-enhanced emissions. Additionally, a diamond membrane having a submicron thickness offers NV centre emission with narrower linewidth and longer electron spin coherence time compared to NV centre emissions from nano-diamonds [30]. Furthermore, diamond membranes with individual NV centres implanted in predetermined positions [32] could serve as critical components for networked quantum computation.

5.1.2 Review of diamond membrane fabrication

To apply the diamond membrane to open optical cavity-QED, fabricating large size single crystal diamond membranes without damages or cracks is critical [33]. There are some commercially available thin diamond platelets (e.g. Element Six, Ltd) [34], however, these diamond platelets are too “thick” ($> 30 \mu\text{m}$) for cavity applications.

There are several ways of fabricating high purity single crystal diamond membranes. The fabrication methods can be generally classified into two categories: the “bottom-up” method and the “top-down” method. The “bottom-up” methods used homoepitaxial growth of diamond on top of a single crystal diamond substrate [35, 36].

This method, however, needs an etching process to remove the rough surface from the backside of the as-grown diamond facet [36].

The “top-down” method thins down a thicker e.g. 20 μm , diamond platelet to achieve the membrane. Several strategies and techniques have been developed in this category including ion implantation [1, 37], FIB milling [38-40], laser cutting [41] and template polishing [42]. However, diamond sample swelling or damage may occur during these processes [43].

Diamond thinning by using RIE or ICP etching was found to be an effective method with the least damage to the diamond sample and thus the least influence on the colour centres [44]. Several diamond structures including nano-wires, photonic crystals, circular gratings, nano-waveguides and integrated diamond circuit have been developed based on this etching method [45-49]. It is worth noting that a combination of the δ -doping and RIE etching method to create NV centres in diamond photonic crystal cavities has been demonstrated recently [50]. Nevertheless, fabrication of large size ($> 2 \text{ mm}$) freestanding diamond membranes with thickness below 1 μm without cracking or damage has not yet been reported and the handling of ultrathin diamond membranes is still a challenge.

In this work, the fabrication technique of such diamond membranes was developed and large size ($\Phi \sim 3 \text{ mm}$), damage-free, ultrathin diamond membranes (thicknesses ranged from 250 nm to 1 μm) were achieved. The details of the fabrication methods will be discussed in Section 5.2. After the fabrication, diamond membranes were transferred to distributed Bragg reflection (DBR) mirrors for further characterisation, which will be discussed in Section 5.3.

5.2 Fabrication of large area ultrathin diamond membranes

To fabricate ultrathin high quality diamond membranes for QIP, the challenges are threefold:

- 1). To handle the diamond membranes without breaking them. The fabricated diamond membrane needs to be manipulated and placed onto a mirror with good conditions for cavity applications. However, the normal handling using tweezers has the risk of breaking diamond membranes due to the contact force.

2). To characterise and control the membrane thickness with high precision. The final diamond membrane thickness is controlled by the etch duration. Due to the typical existence of a wedge, over-etching will etch away part of the diamond membrane and under-etching will make the membrane too thick for cavity applications. Additionally, the information of the membrane morphology is also important for cavity applications. However, since the submicron thick membrane is so fragile, the conventional contact characterisation methods for thickness and surface morphology measurements such as using a Dektak profilometer might break the membrane due to contact force. Moreover, the Dektak is only able to scan 1D line each time across the sample which makes the thickness and profile measurements time-consuming. Thus, a more efficient noncontact measuring method is preferred.

3). To maintain and even improve the diamond surface quality since the surface defects, contamination and roughness will influence the NV emission and detection. Thus, a proper and optimised fabrication process is necessary. These challenges will be revisited separately in the following sections. In this work, the diamond membrane was fabricated from a single crystal diamond platelet produced by Element Six Ltd (initial thickness $\sim 20\ \mu\text{m}$). The diamond platelet is a type II a (nitrogen density $< 1\ \text{ppm}$), (110) oriented natural diamond with a diameter of 3 mm. The process flow used to fabricate the large area diamond membrane is shown in Figure 5-3.

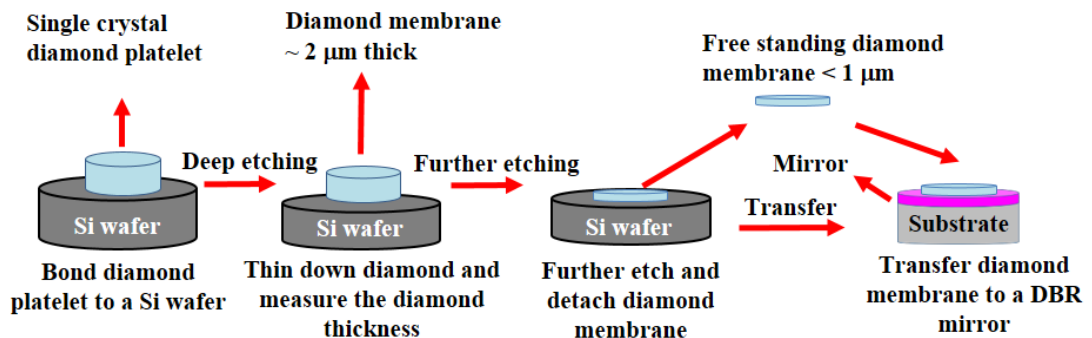


Figure 5-3: Schematic of the fabrication flow for the diamond membrane.

In this method, the diamond platelet was first capillary-bonded onto a polished 4'' supporting silicon (Si) wafer, then thinned down to 2~3 μm by ICP deep etching. Then the thin diamond was detached, cleaned, flipped and re-bonded on a new Si wafer. The cleaning process was used to remove the etch residues. The processes of diamond flipping, re-bonding and the subsequent etching were necessary for removing the

polish marks and improving the surface quality on the other side of the diamond. Re-bonding the thin diamond onto a new Si wafer is necessary for the measurement of the diamond thickness on a flat surface using Dektak surface profiler. The diamond thickness was carefully measured which indicates the etch duration for the further etching process. After re-bonding, additional etching was carried out to etch the diamond to the targeted thickness. Then, the diamond membrane with the desired thickness was detached from the Si wafer and transferred to a DBR mirror with 10 periods of alternating $\lambda/4$ layers of TiO_2 and SiO_2 . The DBR mirrors used have a reflectivity higher than 99.8%. The following sections will give more details on some of these procedures.

Sample preparation

The diamond platelets were first cleaned with Piranha acid (H_2SO_4 : H_2O_2 = 3:1) at 80 °C for 30 mins. The volume of the acids was measured separately with two 100 ml glass beakers. 60 ml 96% sulphuric acid and 20 ml 30% aqueous hydrogen peroxide solutions, were measured first and then mixed in a 100 ml polytetrafluoroethylene (PTFE) heatable beaker: the 30% hydrogen peroxide is first poured into the heatable beaker and the 60 ml 96% sulphuric acid is added little by little. Since adding sulphuric acid to hydrogen peroxide solutions generates considerable heat, the acid mixing must be done slowly, with continuous stirring using a dry glass alcohol thermometer, to avoid local boiling of the mixture. Since the acids are corrosive, one should operate by wearing personal protective equipment including eye goggles, face shield and gloves during the process. The acid mixing process is done in the PTFE beaker as the temperatures generated during mixing may shatter a glass beaker due to thermal shock or melt a plastic one. The unused acids and mixture are disposed of by pouring the them into a tank containing a large volume of water, followed by flushing with excess water. At the end, all work areas and protective equipment are rinsed and wiped dry.

After cleaning, the diamond samples were picked up, transferred and capillary-bonded to a new 4” Si carrier wafer through the van der Waals force. It is worth pointing out that the freshly cleaned diamond samples have the strongest adhesion and thus the bonding process must be done as soon as possible. The cleaning process is highly important since it helps to remove any organic contaminants on the sample

surface. The diamond sample surface must be kept clean since any contaminant will act as an etch mask during diamond etching.

Diamond thinning down by ICP etching

For the diamond thinning process, Ar/Cl₂ ICP etching was used which generates a better etched surface after the deep etching process. The etch recipe was the same as stated in Chapter 2. Before the diamond thinning, a chamber clean using O₂ plasma was conducted for 30 mins. This process helps to remove the deposited contaminants on the sidewalls of the ICP machine from other etching processes. Additionally, the carrier wafer should be cleaned before loading to the chamber. The contaminant may form micro-masks during the diamond etching. After the diamond sample was loaded into the chamber, it was etched for 4 hrs in total. The average etch rate during the etching was 65 nm/min.

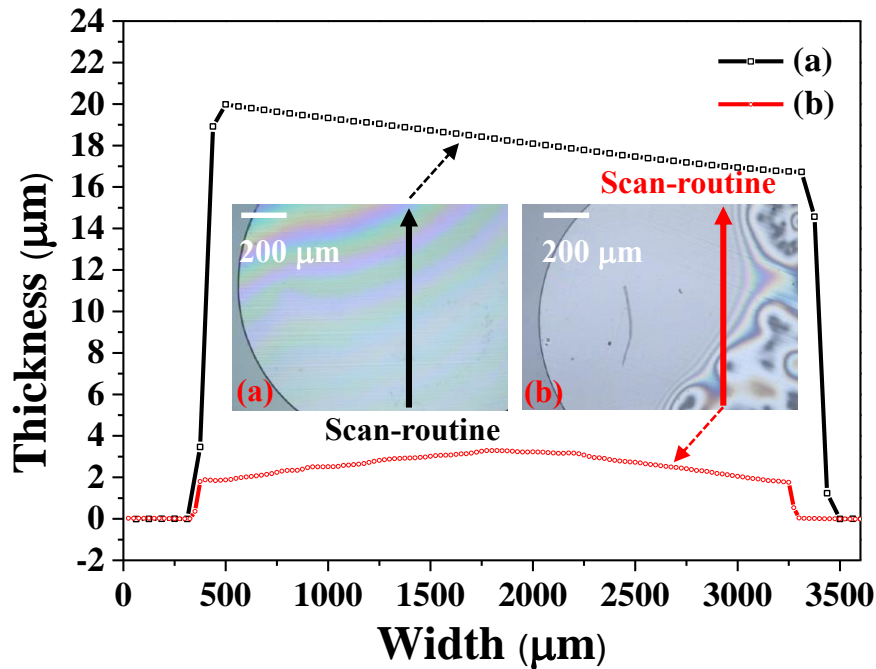


Figure 5-4: Thickness of the diamond platelet (a) before thinning and (b) after thinning. The insets are the corresponding optical images of the diamond sample taken under a microscope, the arrows indicated the scan-routines of the Dektak profiler.

As mentioned above, the diamond platelet was first thinned down to a thickness of 2~3 μm . A diamond membrane with such thickness is relatively easier to handle. The thinned diamond membranes were then transferred to another Si wafer or a DBR mirror for further etching. Before this etching, however, the diamond membrane was measured with a Dektak to confirm the thickness. A thickness comparison before and

after the thinning process is shown in Figure 5-4 where Figure 5-4 (a) is the initial thickness of the diamond platelet before etching and (b) shows the thickness after etching. The corresponding diamond optical images are shown as insets. As shown in Figure 5-4, the average thickness of the wedged diamond platelet before etching is around $18\ \mu\text{m}$ and the thinned diamond membrane has a thickness of around $2.5\ \mu\text{m}$. This thinned diamond membrane was then de-bonded from the Si wafer using a DI water floating method.

Diamond membrane floating

To address the challenge of handling very thin diamond membranes, the procedure described below was used. After thinning, the diamond membrane is usually bonded firmly to the Si wafer. To detach the membrane from the Si wafer, a plastic transfer pipette was used to gently flush the membrane with DI water. Then, the diamond membrane would be detached and floated on the surface of the Si wafer. A schematic and a picture of the floated diamond membrane are shown in Figure 5-5 (a) and (b), respectively. Sometimes, the diamond membrane was too firmly bonded and was not able to be separated by DI water. In this case, one may try to use a small amount of the Piranha acid instead of the DI water to separate the diamond membrane. This process should be carried out in a large glass Petri dish which prevents the diamond membrane from breaking.

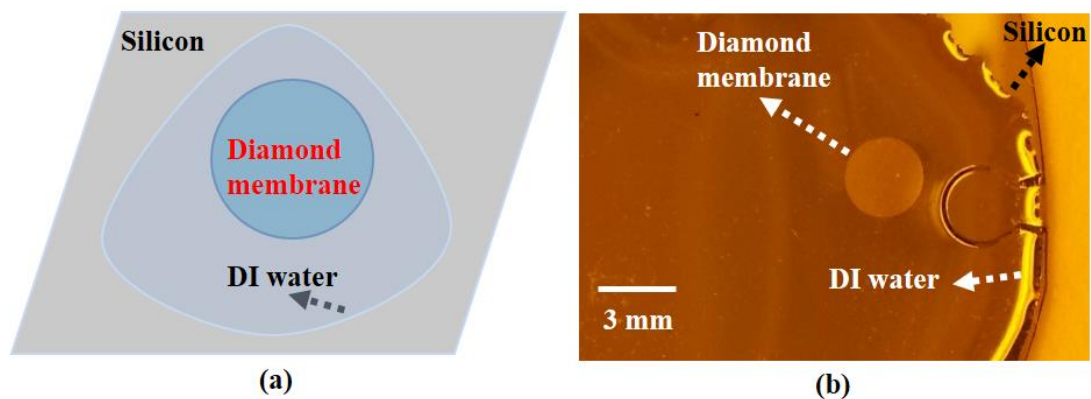


Figure 5-5: (a) Schematic of the floated diamond membrane on a Si wafer using DI water and (b) a picture of the floated diamond membrane on a Si wafer.

Diamond transfer

To transfer to the second Si substrate or a DBR mirror, the diamond membrane was “picked” and “placed” using a clean room wipe. This is preferable to tweezers to avoid breaking the membrane. To pick up the membrane, the wipe is soaked with DI

water or IPA. A photograph of the diamond membrane stuck to the wipe at the edge is shown in Figure 5-6 (a) (the picture was taken using a square diamond sample for illustration purposes). The thinned diamond membrane was then transferred to the targeted substrate for further processing. A photograph of the transferred diamond membrane sitting on a solvent cleaned Si substrate is shown in Figure 5-6 (b).

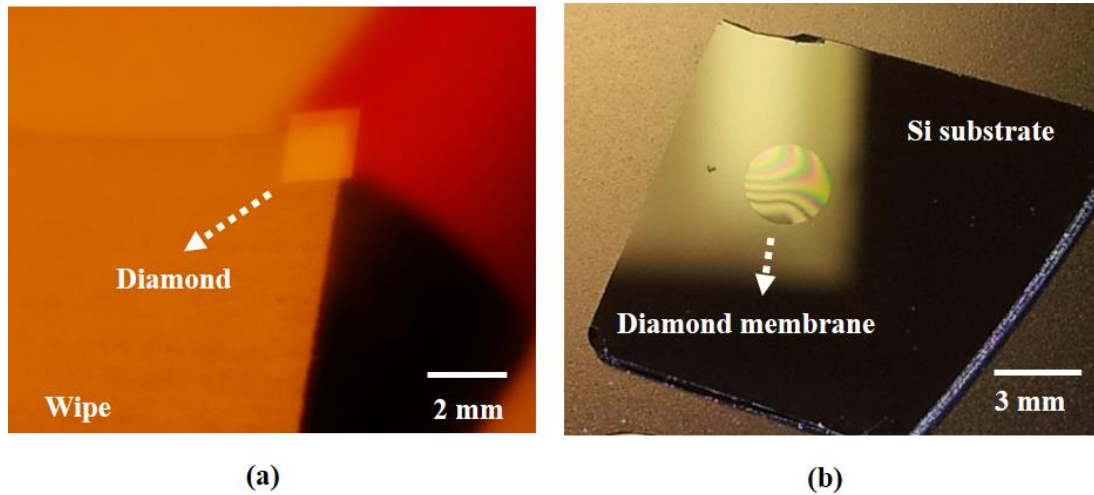


Figure 5-6: Diamond membrane transfer process: (a) a picture demonstrating “pick-up” of the diamond sample using the corner of a cleanroom wipe and (b) a picture of the diamond membrane placed on a solvent-cleaned Si substrate.

Final etching

After transfer, it is necessary to measure the membrane thickness. The measured thickness profile of the diamond membrane is shown by the red curve in Figure 5-4. Further etching of the diamond membrane could be continued after this measurement. The final etching and handling at this stage needs to be carried out with extreme care and the diamond etch rate using ICP Ar/Cl₂ plasma must be calibrated as precisely as possible. The calibrated etch rate was used to set the final etch duration. Once the diamond was etched to an average thickness of less than 1 μm, the etching in the chamber was monitored through the top view window of the ICP chamber. Due to the existence of the wedge on the original diamond platelet, the thinnest part of the diamond is first etched away and the etching must be stopped before etching through the diamond at the thinnest part. This can be monitored from the reflection at the diamond surface through the top view window of the ICP chamber.

After reaching the desired thickness, the submicron diamond membrane was transferred onto a DBR mirror using the floating and transfer procedures, as described above. A photograph of the resulting diamond membrane on a DBR mirror is shown

in Figure 5-7 (a). An image of the same diamond membrane on the DBR mirror under a microscope is shown in Figure 5-7 (b). The diamond membrane was characterised by using non-contact mode AFM in order to avoid damage due to the contact force. The characterisation results will be presented and discussed in the next section.

It is worth noting that the final step of etching using a Cl-based plasma might be detrimental to the subsurface NV centres inside diamond membrane and a surface treatment using the oxygen plasma to change the surface termination to ‘NV-friendly’ O-terminations might be beneficial for the resulting NV centre emissions [51].

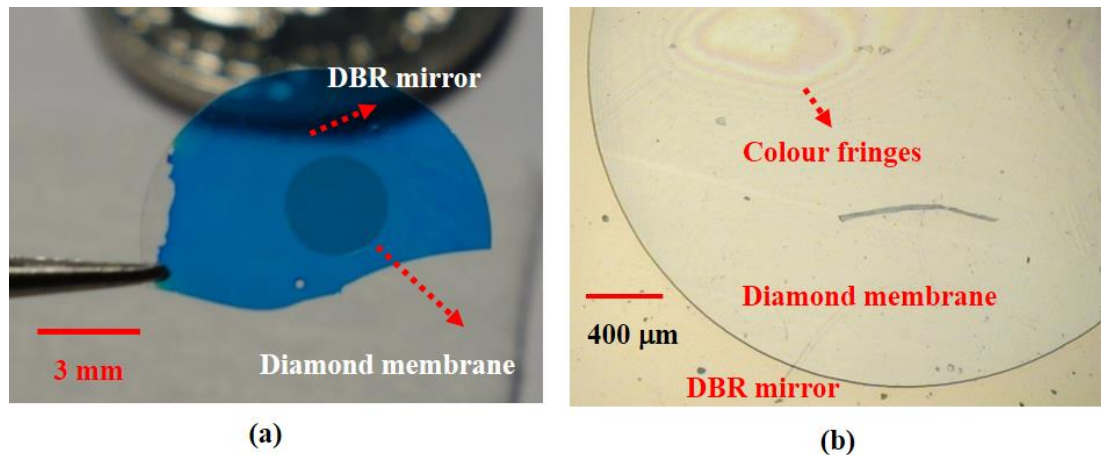


Figure 5-7: Images of the fabricated diamond membrane: (a) A photograph of the fabricated natural diamond membrane. This diamond membrane was capillary bonded to a DBR mirror; (b) Optical image of the natural diamond membrane under a microscope, colour fringes can be observed at the top left corner which indicates the thickness variation there.

5.3 Characterisation of diamond membranes

SEM and AFM were used for the characterisation of the fabricated ultrathin diamond membranes. The general conditions of the diamond membrane, i.e. the uniformity and the flatness, were characterised by using SEM. AFM was used to measure the thickness and the surface roughness of the achieved membranes.

5.3.1 Thickness of the diamond membrane

The SEM images of the fabricated natural diamond membrane with different magnifications are shown in Figure 5-8. These images were taken at a tilt angle of 45°. Figure 5-8 (a) shows the whole diamond membrane was uniformly etched. As far as we know, this is the first time such a large area submicron thick single crystal diamond membrane has been achieved. Figure 5-8 (b) shows a magnified SEM image at the left hand corner of the membrane indicated by a red dotted square in Figure 5-8 (a). A

well-bonded interface between the diamond membrane and the DBR mirror can be observed in this image.

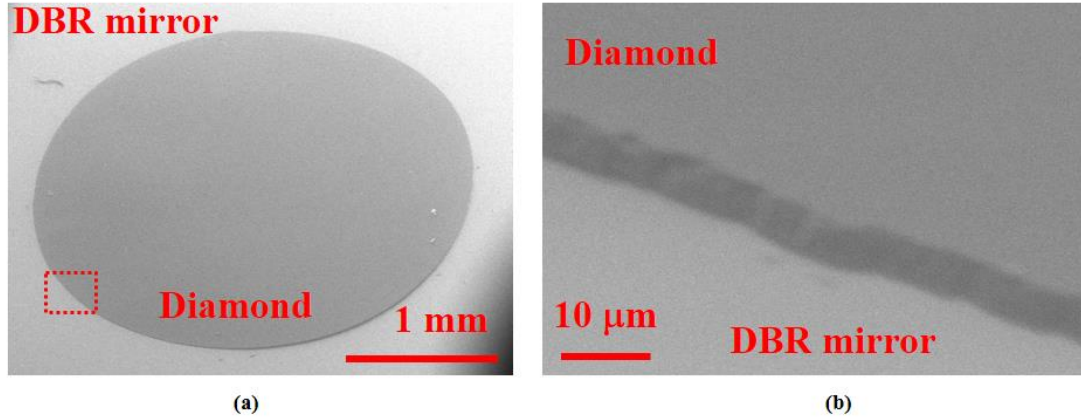


Figure 5-8: SEM images of the achieved thinned natural diamond membrane on a DBR mirror, where the images were taken at a tilted angle of 45° . (a) SEM image of the natural diamond membrane on DBR mirror demonstrating the uniformity of the achieved diamond membrane and (b) SEM image of the left corner indicated by the red dotted square in (a), demonstrating the well-bonded interface between the diamond membrane and the DBR mirror.

To further measure the thickness of the achieved natural diamond membrane with high precision, a non-contact mode AFM was used. AFM measurements were taken at the same corner indicated by the red dotted square shown in Figure 5-8 (a). The measured results are shown in Figure 5-9.

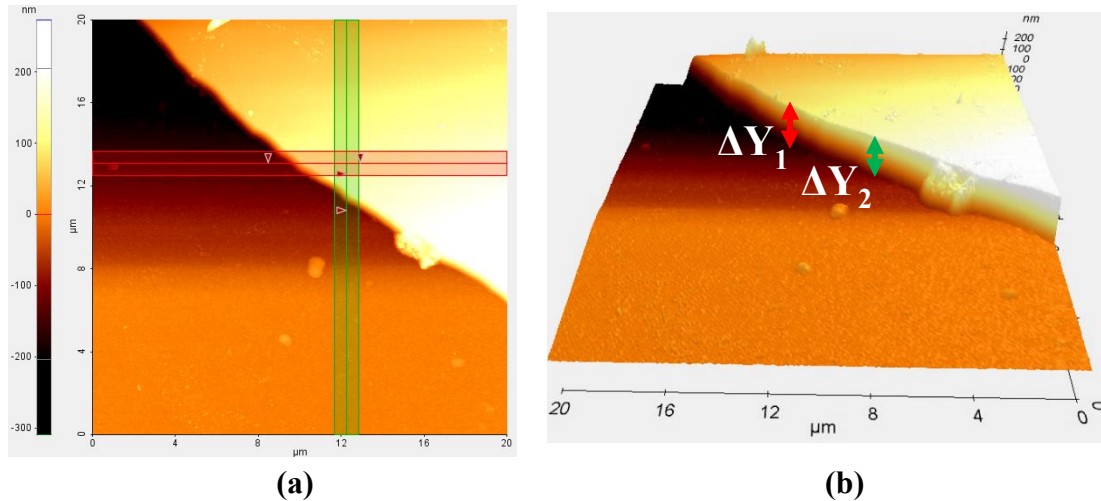


Figure 5-9: AFM measurement results: (a) top view of a measured area of $20 \times 20 \mu\text{m}^2$ at the same corner indicated by the red-dotted-square shown in Figure 5-8 (a); (b) 3D perspective image of the measured corner of the diamond membrane. Thicknesses of the edges indicated by the green and red line shown in (a) were labelled with white letters, demonstrating thicknesses of the membrane ΔY_1 is 294.4 nm and ΔY_2 is 257.8 nm, respectively.

Figure 5-9 (a) illustrates the top view of the overall measured area of the natural diamond membrane. The measured area is $20 \times 20 \mu\text{m}^2$. Figure 5-9 (b) shows the

measured thicknesses at the edges of the membrane indicated by the lateral red line and vertical green line cross over in Figure 5-9 (a). The measured thicknesses at these two edges are $\Delta Y_1=294.4$ nm and $\Delta Y_2=257.8$ nm, respectively. These measured results are consistent with the estimation by using the etch rate and duration, confirming the submicron thickness of the diamond membrane.

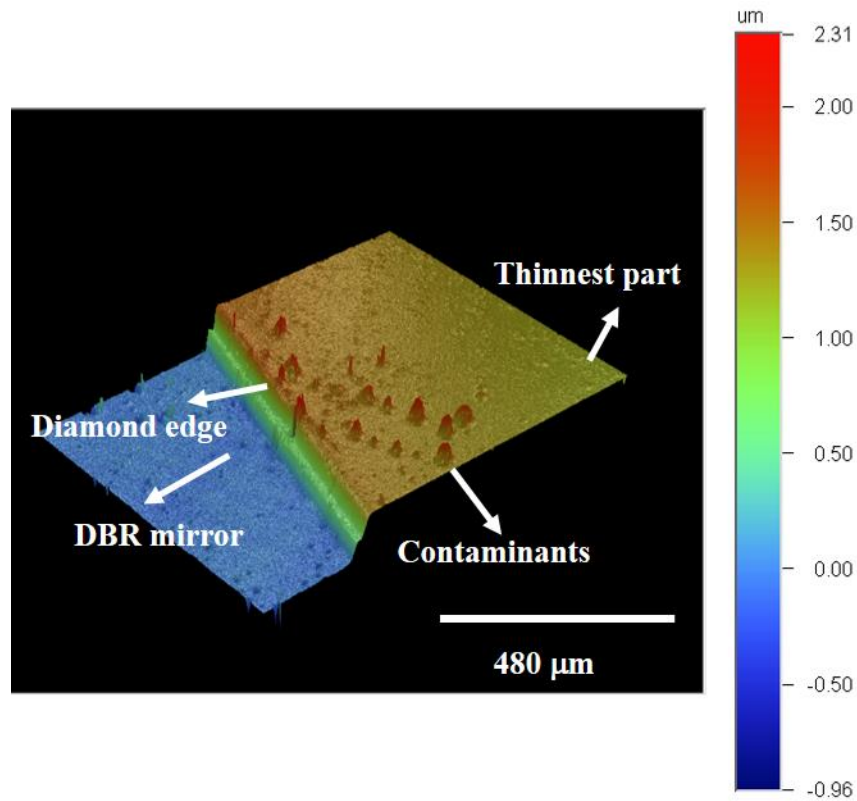


Figure 5-10: 3D image of the measured thickness variation using the optical profiler. The coloured bar indicates the corresponding thickness reflected in the 3D image, the measured area is $640 \times 480 \mu\text{m}^2$.

In using AFM, only a limited area (up to $40 \times 40 \mu\text{m}^2$) can be measured each time. This makes it difficult to map the thickness of the whole diamond membrane. The Dektak measurement, however, can only measure the thickness profile in a single scanned line each time and thus has the same problem of thickness mapping as the AFM. Besides, the contact force from the stylus of the Dektak might damage the ultrathin diamond membrane. However, for cavity applications, the thickness mapping of the diamond membrane is critical. In order to map the thickness of diamond membrane, a non-contact and more efficient measuring method is necessary. In this work, an optical profiler, Wyko NT 1100, has been used for the thickness mapping of the achieved diamond membrane. The principle of this tool was presented in Chapter

2. The measured result for the diamond membrane is shown in Figure 5-10 with a measured area of $640 \times 480 \mu\text{m}^2$. Large area thickness mapping could be realised by stitching of several such measured images together. Figure 5-10 shows the 3D image of the diamond membrane on the DBR mirror. The thinnest part of the measured area can be seen from the corresponding colour based on the colour bar. This optical profiler is an ideal method for the overall thickness mapping of the achieved diamond membrane. Further measurements are necessary for full characterisation of the whole membrane. However, due to the time limitation, only the initial measurement was carried out and shown here.

5.3.2 Surface quality of diamond membranes

To characterise the diamond membrane surface quality after etching, AFM was used to measure the RMS surface roughness. Additionally, the surface of the as-received diamond platelet was also measured for a comparison. Figure 5-11 (a) shows the surface of the as-received diamond platelet and (b) shows the surface of the achieved diamond membrane, respectively. These measurements show that the as-received diamond platelet has an RMS surface roughness of 0.83 nm ($3 \times 3 \mu\text{m}^2$) compared with an etched diamond surface having an RMS roughness of 0.25 nm ($3 \times 3 \mu\text{m}^2$). This results show that the ICP Ar/Cl₂ plasma etching used here has improved the surface quality of the diamond sample, consistent with the result reported by C. Lee et al. [52].

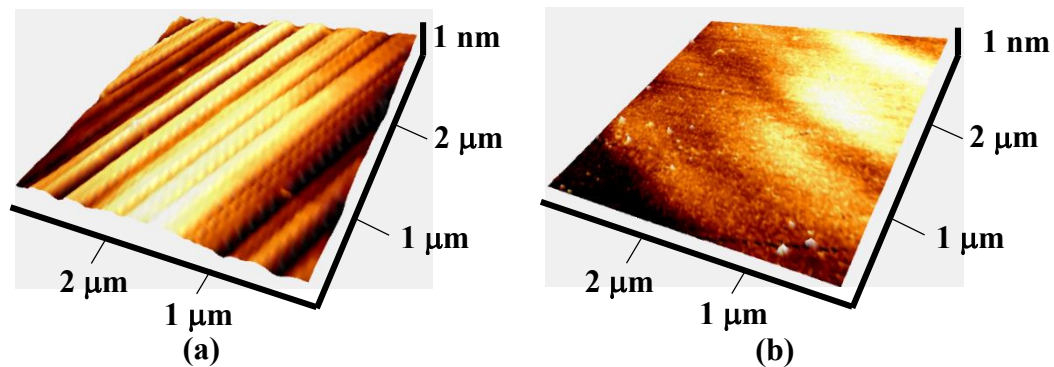


Figure 5-11: AFM measured RMS surface roughness results of: (a) As-received diamond surface, R_q is 0.83 nm ($3 \times 3 \mu\text{m}^2$); (b) Etched membrane surface, R_q is 0.25 nm ($3 \times 3 \mu\text{m}^2$).

5.4 Applications of diamond membranes in cavity-QED

As mentioned in Section 5.1, the main purpose of developing the ultrathin diamond membrane is for cavity-coupled NV centre emission enhancement. The NV centre emissions from the achieved diamond membranes are characterised here. The emission from an NV centre in the diamond membrane was characterised first in free space. Then, to evaluate the cavity-coupled emission enhancement, characterisation of the emission from the open optical cavity-coupled diamond membrane was carried out.

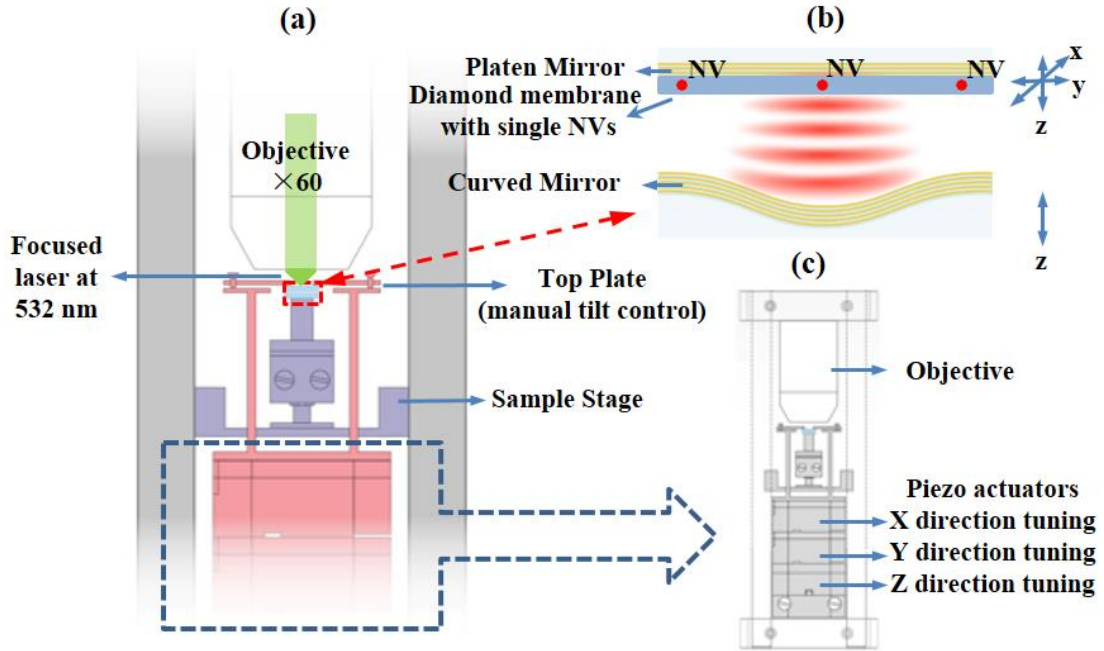


Figure 5-12: Schematics of the experimental setup of the open optical cavity-coupled diamond membrane: (a) schematic of the sample stage, (b) schematic of the independently tunable mirrors and (c) schematic of the piezo actuators.

To characterise the NV centre emission, the home-built scanning confocal microscope mentioned in Chapter 2 was used. Schematics of the experimental setup of the open optical cavity-coupled diamond membrane are shown in Figure 5-12, in which (a) shows the sample stage, where an objective lens ($\times 60$) was used to focus the laser beam onto the sample, (b) highlights the independently tunable mirror cavity-coupling of the diamond membrane sample and (c) shows the piezo actuators used to tune the positions of the featured mirror at X, Y, Z directions. For this confocal microscope, the laser excitation wavelength is at 532nm. Either a 670nm-810nm band-pass filter or a 650 nm long-pass filter was used in the microscope collection arm for better PL imaging quality. The emission spectra from the ultrathin diamond

membranes were taken using a liquid nitrogen cooled Princeton CCD camera. Both photoluminescence (PL) images and the emission spectrum from the NV centres were measured.

5.4.1 Emission from the NV centre in free space

At the initial PL scans, the PL background from the membrane was very high, with a photon count rate of about 150,000 counts/sec under 1mW excitation power with a power density of 0.396 mW/cm^2 (single NV centres usually have a count rate of roughly 30,000 counts/sec [30]). To suppress the background fluorescence, the diamond membrane was exposed to the laser radiation overnight. By using this method, the background fluorescence is reduced. This phenomenon is named photo-bleaching [23].

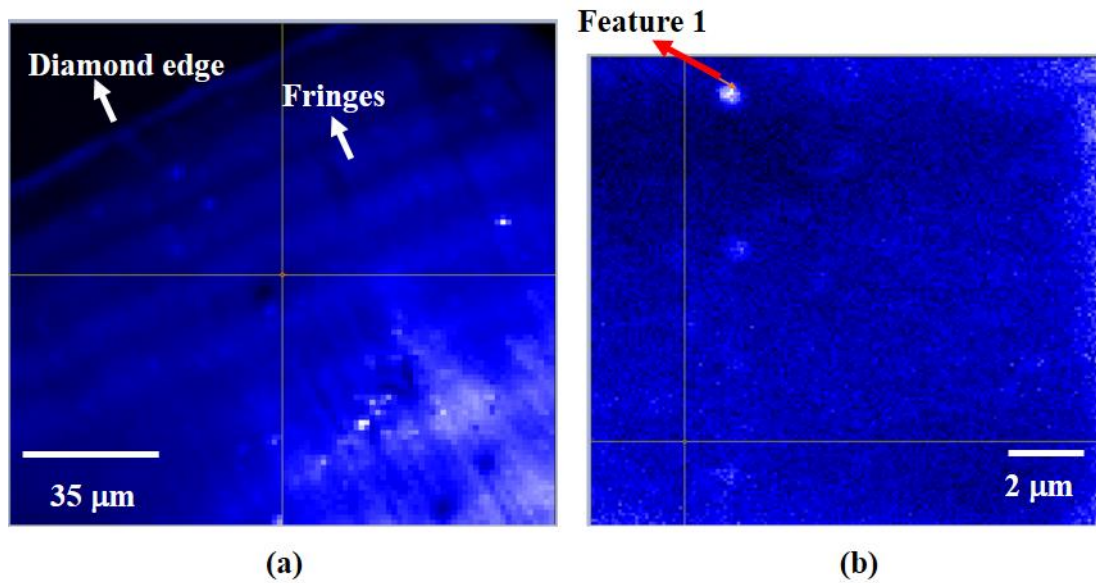


Figure 5-13: PL images at the membrane edge: (a) PL image of the overall scan at an area of $140 \times 140 \mu\text{m}^2$, some fringes can be observed at the edge which represent uneven thicknesses due to the wedge; (b) Zoom-in of the PL image which presents a bright single feature as labelled with Feature 1.

After several hours of photo-bleaching, PL images were taken. Figure 5-13 (a) shows the PL image of a $140 \times 140 \mu\text{m}^2$ area at the edge of the diamond membrane. Some fringes close to the diamond edge can be observed from this PL image indicating the thickness variation of the diamond membrane. A bright spot feature, which might be NV centre emission, was observed and is labelled as Feature 1 in the zoomed-in PL image in Figure 5-13 (b). The measured area for this image is $14 \times 14 \mu\text{m}^2$. The PL

spectrum of Feature 1 was also measured and is shown in Figure 5-14 (a). A sharp line at 573 nm which represents the first order of Raman shift mentioned in Chapter 4, is observed in this spectrum. Apart from this Raman peak, the measured spectrum seems to be a modified NV centre emission spectrum due to the etalon effect [53]. The broad emissions up to 800 nm are expected from the nature of the NV centre emission as discussed in Section 5.1.1.

To further characterise the emission, the saturation power of Feature 1 was measured and fitted. The PL intensity of a solid-state NV centre saturates when the excitation power reaches a certain level. The measured power saturation curve is shown in Figure 5-14 (b) with a fitted saturation power of 1.8mW using the method as reported in [54]. This result is consistent with typical NV centres and confirms the NV nature of this feature [55].

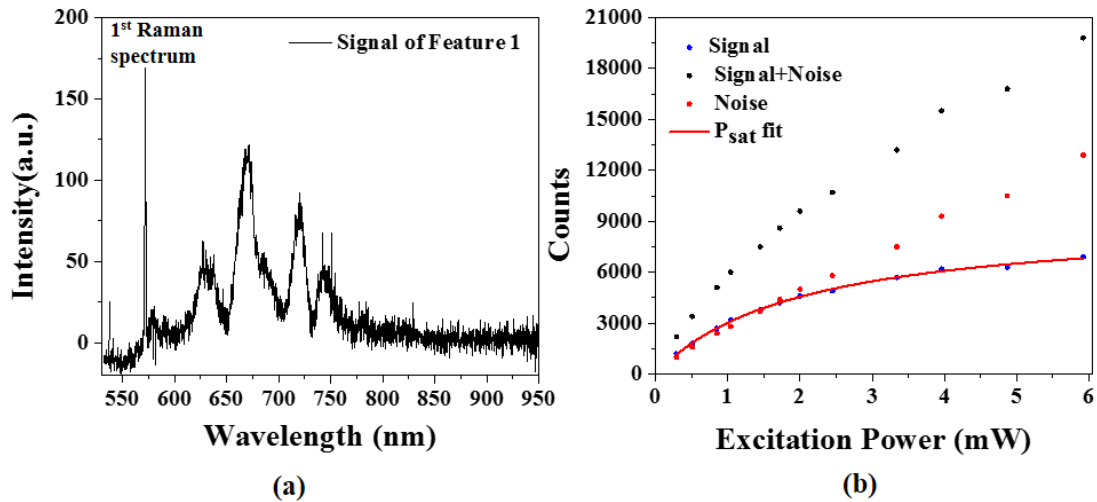


Figure 5-14: (a) Emission spectrum from Feature 1 under 1mW excitation power, a sharp line at 573 nm represents the 1st Raman peak. (b) Measured result of the power saturation of Feature 1 and the fit, signal refers to the count from the NV, noise refers to the count from the background noise and P_{sat} fit refers to the saturation fit of the power used at 1.8 mW, 0.396 mW/cm² using the method as reported in [54].

5.4.2 Cavity-enhanced emission

To evaluate the enhancement of cavity-enhanced emission, the natural diamond membrane was placed on top of a planar DBR mirror and coupled to a curved concave mirror. The planar and concave mirrors have reflectivities of 99.7% and >99.99%, respectively, at a design wavelength of 637 nm, and their reflection bands extend from 550 nm to 720 nm. The planar mirror is terminated with a low index layer to provide a field anti-node at its surface. A 532 nm laser was used to excite the NV centres in

the diamond membrane from the planar mirror side. The schematic and a picture of the cavity with an inserted diamond membrane are shown in Figure 5-15.

As introduced in Section 5.1, the NV centre emission will be enhanced when it matches a cavity resonance. The enhancement will be larger if the cavity has a higher Q-factor and a smaller cavity volume. The Q-factor of a cavity is calculated as:

$$Q = \frac{\lambda}{\delta\lambda} \quad (5-3)$$

where λ denotes the central wavelength and $\delta\lambda$ denotes the full-width-half-maximum (FWHM) of emission spectrum in resonance with the cavity mode.

The cavity Q-factor is determined by the cavity materials and structures and thus cannot be tuned. Thus, to achieve the maximum enhancement, the two cavity mirrors should be as close as possible. The curved concave mirror used in our experiment has a radius of curvature of 20 μm .

During the experiments, as the diamond membrane has a wedge profile, we moved the curved concave mirror to the edge and the centre of the membrane and adjusted its vertical position so as to form a cavity with the minimum cavity length/volume. Figure 5-15 and Figure 5-17 show these two configurations, respectively.

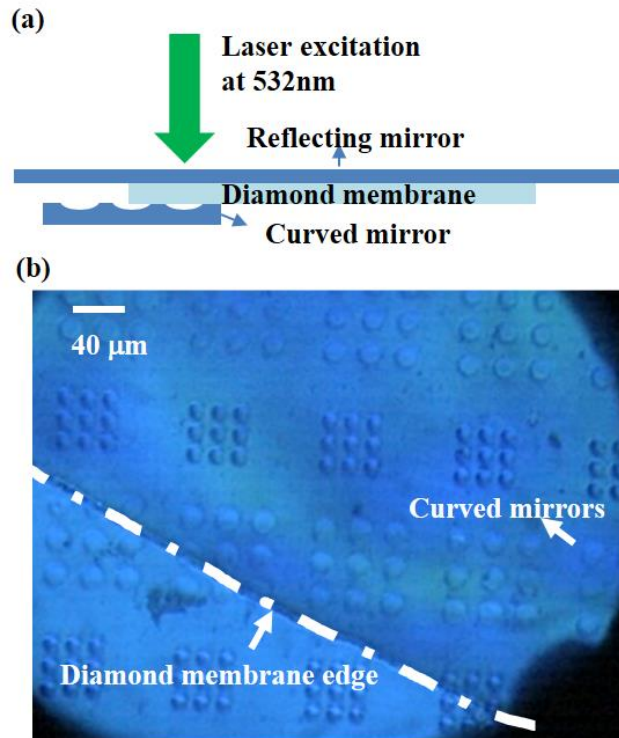


Figure 5-15: (a) Side-view schematic of the cavity-coupled diamond membrane at the edge and (b) an image of the open optical cavity-coupled diamond membrane under a microscope.

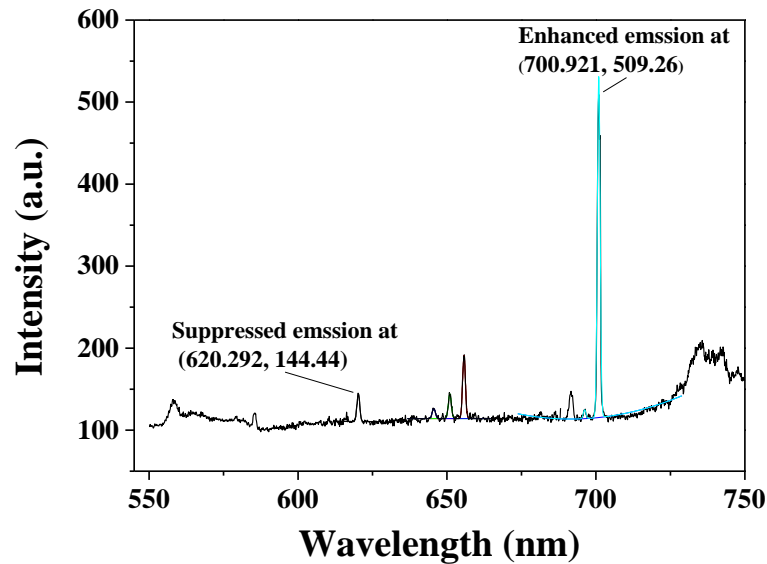


Figure 5-16: Spectrum of cavity-enhanced emission from the diamond membrane, cavity length 2.11 μm .

For the configuration with the emission from the edge of the diamond membrane, the minimum achieved cavity length is 2.11 μm . Figure 5-16, shows the Gaussian function fitted cavity-enhanced emission spectrum. In this spectrum, an enhanced emission peak is seen at 700.9 nm with an FWHM of 1.086 nm. This emission peak might come from a NV centre emission tuned by the etalon effect or from NV centre ensembles. The Q-factor is 645, calculated from this emission and Equation (5-3). The enhancement of this emission spectrum and the suppression of other emissions can be clearly observed in Figure 5-16. The enhanced intensity is 3.5 times larger than the suppressed intensity at 620.3 nm.

Similarly, the configuration for the central part of the cavity-coupled diamond membrane being inside the cavity is shown in Figure 5-17. In this case, the cavity length is 3.39 μm . A Q-factor of 695 (FWHM 1.019 nm) is obtained from the emission peak at 708.6 nm as shown in Figure 5-18. The intensity of the emission at 708.6 nm is 4.5 times larger than the suppressed emission at 599.4 nm. Again, this 708.6 nm peak might come from the NV centre emission tuned by the etalon effect or from NV centre ensembles. However, the diamond sample used has a high NV centre density, and so it is difficult to identify a single NV centre in the membrane in practice.

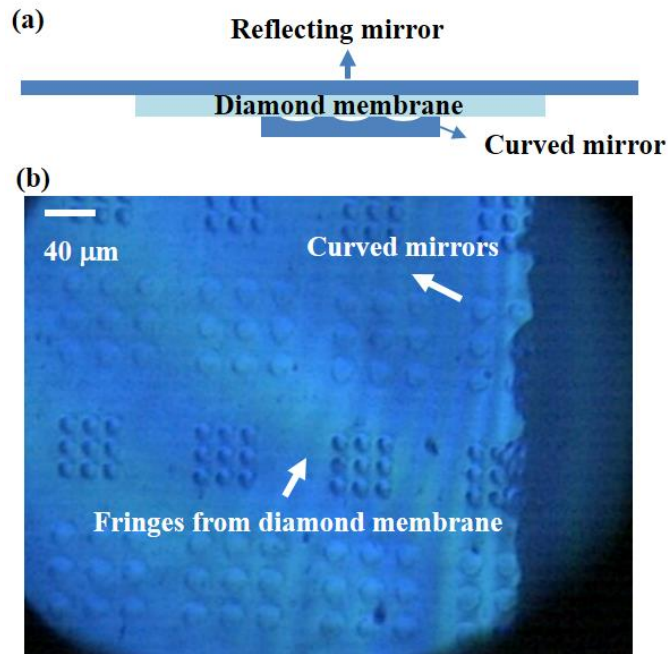


Figure 5-17: (a) Side-view schematic of cavity-coupled diamond membrane and (b) an image of the open optical cavity-coupled diamond membrane under a microscope.

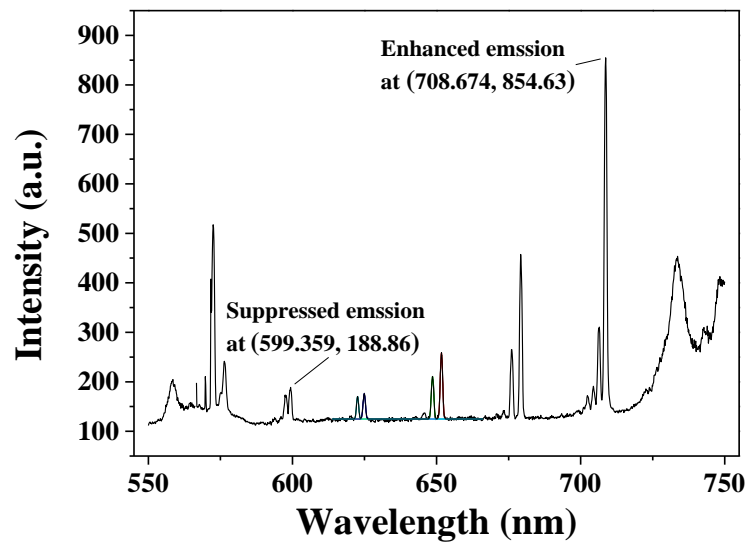


Figure 5-18: Spectrum of cavity-enhanced emission from the diamond membrane, cavity length $3.39 \mu\text{m}$.

The above characterisations verify the cavity enhanced emissions from the diamond membrane. Note that the Q-factors derived from the cavity-enhanced emissions have not changed much according to the cavity lengths. This means that the enhancement of cavity-coupled emission might more likely be limited by the quality of the DBR mirrors used. Single NV emission enhancement at the ZPL has not been

observed which may be due to the lack of single NV centre features in the diamond membrane. Diamond with implanted NV centres should be used for membrane fabrication in future. In particular, by combining diamond membrane fabrication with controllable implantation of single NV centres, one could realise single NV centre arrays in diamond membranes. This could be an attractive route towards the construction of scalable quantum computing.

In addition, NV centres are also important in other applications such as magnetometry and thermostats as the NV centres are sensitive to magnetic field, electric field and thermal gradient. Incorporating ion implantation of a single colour centre to produce a solid-state photo-stable single photon source at room temperature is one basis for quantum computing applications.

By using focus ion beam milling or electron beam lithography well defined micro/nano- diamond structures such as ring resonators and waveguides can be further developed on the diamond membranes. These micro/nano diamond structures are critical components to enhance and guide emissions from NV centres for applications in scalable quantum processors. Moreover, combined with the use of transfer printing, freestanding diamond membranes with NV centres can be transferred to a particular position at a photonic structure to achieve the integrated quantum photonic circuits. Besides, diamond membranes can also find use in X-ray windows [2], protein detection, heavy metal detection and neutron detections [3, 4]. The large Young's modulus of diamond makes diamond membranes also useful in MEMS and NEMS for fast switching [5].

5.5 Conclusion

In this chapter, a method of fabricating large area ultrathin diamond membranes is reported. The fabricated diamond membrane has thicknesses ranging from 0.25 μm to a 1 μm edge-to-edge due to the existing initial diamond wedge. The SEM and the AFM are used to characterise the uniformity and thicknesses of the fabricated natural diamond membrane. An optical profiler was used to map the thickness variation at a large area and could be further explored for the morphology of the fabricated diamond membrane. The fabricated diamond membrane was transferred to planar DBR mirrors for characterisation of the NV emission under a home-built confocal microscope. A

potential NV centre feature embedded in the achieved diamond membranes was characterised. The PL intensities of the NV emission are measured both in free space and coupled open optical cavity. Note that the emission is affected by long term exposure under laser excitation, demonstrating a photo-bleaching behaviour. This might be due to the unstable charge state of the NV. Enhanced emissions that are matched to the cavity resonance mode have been observed, which confirms the feasibility of cavity-coupled diamond membranes for applications in quantum information processing.

References

- [1] J.C. Lee, A.P. Magyar, D.O. Bracher, I. Aharonovich, E.L. Hu, Fabrication of thin diamond membranes for photonic applications, *Diamond and Related Materials*, **33**, 45 (2013).
- [2] X. Ying, J. Luo, P. Wang, M. Cui, Y. Zhao, G. Li, P. Zhu, Ultra-thin freestanding diamond window for soft X-ray optics, *Diamond and Related Materials*, **12**, 719 (2003).
- [3] M. Pomorski, B. Caylar, P. Bergonzo, Super-thin single crystal diamond membrane radiation detectors, *Applied Physics Letters*, **103**, 112106 (2013).
- [4] V. Grilj, N. Skukan, M. Pomorski, W. Kada, N. Iwamoto, T. Kamiya, T. Ohshima, M. Jakšić, An ultra-thin diamond membrane as a transmission particle detector and vacuum window for external microbeams, *Applied Physics Letters*, **103**, 243106 (2013).
- [5] Y. Tao, J.M. Boss, B.A. Moores, C.L. Degen, Single-crystal diamond nanomechanical resonators with quality factors exceeding one million, *Nature Communications*, **5**, 1 (2014).
- [6] A.P. Magyar, J.C. Lee, A.M. Limarga, I. Aharonovich, F. Rol, D.R. Clarke, M. Huang, E.L. Hu, Fabrication of thin, luminescent, single-crystal diamond membranes, *Applied Physics Letters*, **99**, 081913 (2011).
- [7] L. Li, T. Schröder, E.H. Chen, M. Walsh, I. Bayn, J. Goldstein, O. Gaathon, M.E. Trusheim, M. Lu, J. Mower, M. Cotlet, M.L. Markham, D.J. Twitchen, D. Englund, Coherent spin control of a nanocavity-enhanced qubit in diamond, *Nature Communications*, **6**, 1 (2015).
- [8] Y. Zhang, L. McKnight, Z. Tian, S. Calvez, E. Gu, M.D. Dawson, Large cross-section edge-coupled diamond waveguides, *Diamond and Related Materials*, **20**, 564 (2011).
- [9] A. Faraon, P.E. Barclay, C. Santori, K.-M.C. Fu, R.G. Beausoleil, Resonant enhancement of the zero-phonon emission from a colour centre in a diamond cavity, *Nature Photonics*, **5**, 301 (2011).
- [10] C.-H. Su, A.D. Greentree, L.C.L. Hollenberg, High-performance diamond-based single-photon sources for quantum communication, *Physical Review A*, **80**, 052308 (2009).
- [11] A. Beveratos, R. Brouri, T. Gacoin, A. Villing, J.-P. Poizat, P. Grangier, Single Photon Quantum Cryptography, *Physical Review Letters*, **89**, 187901 (2002).
- [12] R. Schirhagl, K. Chang, M. Loretz, C.L. Degen, Nitrogen-Vacancy Centres in Diamond: Nanoscale Sensors for Physics and Biology, *Annual Review of Physical Chemistry*, **65**, 83 (2014).

-
- [13] T. van der Sar, Z.H. Wang, M.S. Blok, H. Bernien, T.H. Taminiau, D.M. Toyli, D.A. Lidar, D.D. Awschalom, R. Hanson, V.V. Dobrovitski, Decoherence-protected quantum gates for a hybrid solid-state spin register, *Nature*, **484**, 82 (2012).
- [14] M.A. Nielsen, I.L. Chuang, *Quantum Computation and Quantum Information: 10th Anniversary Edition*, Cambridge University Press, (2010).
- [15] V.V. Dobrovitski, G.D. Fuchs, A.L. Falk, C. Santori, D.D. Awschalom, Quantum Control over Single Spins in Diamond, *Annual Review of Condensed Matter Physics*, **4**, 23 (2013).
- [16] M.W. Doherty, N.B. Manson, P. Delaney, F. Jelezko, J. Wrachtrup, L.C.L. Hollenberg, The nitrogen-vacancy colour centre in diamond, *Physics Reports*, **528**, 1 (2013).
- [17] G. Balasubramanian, P. Neumann, D. Twitchen, M. Markham, R. Kolesov, N. Mizuochi, J. Isoya, J. Achard, J. Beck, J. Tissler, V. Jacques, P.R. Hemmer, F. Jelezko, J. Wrachtrup, Ultralong spin coherence time in isotopically engineered diamond, *Nature Materials*, **8**, 383 (2009).
- [18] E. Togan, Y. Chu, A.S. Trifonov, L. Jiang, J. Maze, L. Childress, M.V.G. Dutt, A.S. Sorensen, P.R. Hemmer, A.S. Zibrov, M.D. Lukin, Quantum entanglement between an optical photon and a solid-state spin qubit, *Nature*, **466**, 730 (2010).
- [19] I. Aharonovich, S. Castelletto, D.A. Simpson, C.H. Su, A.D. Greentree, S. Prawer, Diamond-based single-photon emitters, *Reports on Progress in Physics*, **74**, 076501 (2011).
- [20] F. Takahiro, D. Yuki, M. Takehide, M. Yoshiyuki, K. Hiromitsu, M. Tsubasa, M. Toshiharu, Y. Satoshi, M. Ryusuke, T. Norio, H. Mutsuko, S. Yuki, M. Hiroki, T. Toshiyuki, M. Shinji, S. Yoshishige, M. Norikazu, Perfect selective alignment of nitrogen-vacancy centres in diamond, *Applied Physics Express*, **7**, 055201 (2014).
- [21] S. Arroyo-Camejo, A. Lazarev, S.W. Hell, G. Balasubramanian, Room temperature high-fidelity holonomic single-qubit gate on a solid-state spin, *Nature Communications*, **5**, 1 (2014).
- [22] N. Bar-Gill, L.M. Pham, C. Belthangady, D. Le Sage, P. Cappellaro, J.R. Maze, M.D. Lukin, A. Yacoby, R. Walsworth, Suppression of spin-bath dynamics for improved coherence of multi-spin-qubit systems, *Nature Communications*, **3**, 858 (2012).
- [23] S. Prawer, I. Aharonovich, *Quantum Information Processing with Diamond: Principles and Applications*, Elsevier Science, (2014).
- [24] K. Beha, H. Fedder, M. Wolfer, M.C. Becker, P. Siyushev, M. Jamali, A. Batalov, C. Hinz, J. Hees, L. Kirste, H. Obloh, E. Gheeraert, B. Naydenov, I. Jakobi, F. Dolde, S. Pezzagna, D. Twitchen, M. Markham, D. Dregely, H. Giessen, J. Meijer, F. Jelezko, C.E. Nebel, R. Bratschitsch, A. Leitenstorfer, J. Wrachtrup, Diamond nanophotonics, *Beilstein Journal of Nanotechnology*, **3**, 895 (2012).
- [25] R.J. Schoelkopf, S.M. Girvin, Wiring up quantum systems, *Nature*, **451**, 664 (2008).
- [26] D. Englund, B. Shields, K. Rivoire, F. Hatami, J. Vučković, H. Park, M.D. Lukin, Deterministic Coupling of a Single Nitrogen Vacancy Centre to a Photonic Crystal Cavity, *Nano Letters*, **10**, 3922 (2010).

- [27] R. Albrecht, A. Bommer, C. Deutsch, J. Reichel, C. Becher, Coupling of a Single Nitrogen-Vacancy Centre in Diamond to a Fiber-Based Microcavity, *Physical Review Letters*, **110**, 243602 (2013).
- [28] Y. Ruan, B.C. Gibson, D.W.M. Lau, A.D. Greentree, H. Ji, H. Ebendorff-Heidepriem, B.C. Johnson, T. Ohshima, T.M. Monro, Atom-Photon Coupling from Nitrogen-vacancy Centres Embedded in Tellurite Microspheres, *Scientific Reports*, **5**, 11486 (2015).
- [29] P.E. Barclay, K.-M. Fu, C. Santori, R.G. Beausoleil, Hybrid photonic crystal cavity and waveguide for coupling to diamond NV-centres, *Optics Express*, **17**, 9588 (2009).
- [30] S. Johnson, P.R. Dolan, T. Grange, A.A.P. Trichet, G. Hornecker, Y.C. Chen, L. Weng, G.M. Hughes, A.A.R. Watt, A. Auffèves, J.M. Smith, Tunable cavity coupling of the zero phonon line of a nitrogen-vacancy defect in diamond, *New Journal of Physics*, **17**, 122003 (2015).
- [31] D.G. Andrew, Nanodiamonds in Fabry-Perot cavities: a route to scalable quantum computing, *New Journal of Physics*, **18**, 021002 (2016).
- [32] R. Hanson, Quantum information: Mother Nature outgrown, *Nature Materials*, **8**, 368 (2009).
- [33] A.H. Piracha, K. Ganesan, D.W.M. Lau, A. Stacey, L.P. McGuinness, S. Tomljenovic-Hanic, S. Prawer, Scalable fabrication of high-quality, ultra-thin single crystal diamond membrane windows, *Nanoscale*, **8**, 6860 (2016).
- [34] Element Six Ltd. http://www.e6.com/wps/wcm/connect/e6_content_en/home
- [35] I. Aharonovich, J.C. Lee, A.P. Magyar, B.B. Buckley, C.G. Yale, D.D. Awschalom, E.L. Hu, Homoepitaxial Growth of Single Crystal Diamond Membranes for Quantum Information Processing, *Advanced Materials*, **24**, OP54 (2012).
- [36] I. Aharonovich, A.D. Greentree, S. Prawer, Diamond photonics, *Nature Photonics*, **5**, 397 (2011).
- [37] B.A. Fairchild, P. Olivero, S. Rubanov, A.D. Greentree, F. Waldermann, R.A. Taylor, I. Walmsley, J.M. Smith, S. Huntington, B.C. Gibson, D.N. Jamieson, S. Prawer, Fabrication of Ultrathin Single-Crystal Diamond Membranes, *Advanced Materials*, **20**, 4793 (2008).
- [38] A.A. Martin, S. Randolph, A. Botman, M. Toth, I. Aharonovich, Maskless milling of diamond by a focused oxygen ion beam, *Scientific Reports*, **5**, 8958 (2015).
- [39] T.M. Babinec, J.T. Choy, K.J.M. Smith, M. Khan, M. Lončar, Design and focused ion beam fabrication of single crystal diamond nanobeam cavities, *Journal of Vacuum Science & Technology B*, **29**, 010601 (2011).
- [40] P. Olivero, S. Rubanov, P. Reichart, B.C. Gibson, S.T. Huntington, J.R. Rabeau, A.D. Greentree, J. Salzman, D. Moore, D.N. Jamieson, S. Prawer, Characterisation of three-dimensional microstructures in single-crystal diamond, *Diamond and Related Materials*, **15**, 1614 (2006).
- [41] Delaware Diamond Knives, Inc. <http://www.ddk.com/cvd-diamond.php>
- [42] Y. Tao, C. Degen, Facile Fabrication of Single-Crystal-Diamond Nanostructures with Ultrahigh Aspect Ratio, *Advanced Materials*, **25**, 3962 (2013).
- [43] A. Silverman, J. Adler, R. Kalish, Diamond membrane surface after ion-implantation-induced graphitization for graphite removal: Molecular dynamics simulation, *Physical Review B*, **83**, 224206 (2011).

- [44] L. Li, M. Trusheim, O. Gaathon, K. Kisslinger, C.-J. Cheng, M. Lu, D. Su, X. Yao, H.-C. Huang, I. Bayn, A. Wolcott, R.M. Osgood, D. Englund, Reactive ion etching: Optimized diamond membrane fabrication for transmission electron microscopy, *Journal of Vacuum Science & Technology B*, **31**, 06FF01 (2013).
- [45] B.J.M. Hausmann, J.T. Choy, T.M. Babinec, B.J. Shields, I. Bulu, M.D. Lukin, M. Lončar, Diamond nanophotonics and applications in quantum science and technology, *Physica status solidi (a)*, **209**, 1619 (2012).
- [46] L. Li, T. Schröder, E.H. Chen, H. Bakhru, D. Englund, One-dimensional photonic crystal cavities in single-crystal diamond, *Photonics and Nanostructures-Fundamentals and Applications*, **15**, 130 (2015).
- [47] B.J.M. Hausmann, M. Khan, Y. Zhang, T.M. Babinec, K. Martinick, M. McCutcheon, P.R. Hemmer, M. Lončar, Fabrication of diamond nanowires for quantum information processing applications, *Diamond and Related Materials*, **19**, 621 (2010).
- [48] L. Li, E.H. Chen, J. Zheng, S.L. Mouradian, F. Dolde, T. Schröder, S. Karaveli, M.L. Markham, D.J. Twitchen, D. Englund, Efficient Photon Collection from a Nitrogen Vacancy Centre in a Circular Bullseye Grating, *Nano Letters*, **15**, 1493 (2015).
- [49] S.A. Momenzadeh, R.J. Stöhr, F.F. de Oliveira, A. Brunner, A. Denisenko, S. Yang, F. Reinhard, J. Wrachtrup, Nanoengineered Diamond Waveguide as a Robust Bright Platform for Nanomagnetometry Using Shallow Nitrogen Vacancy Centres, *Nano Letters*, **15**, 165 (2015).
- [50] J.C. Lee, D.O. Bracher, S. Cui, K. Ohno, C.A. McLellan, X. Zhang, P. Andrich, B. Alemán, K.J. Russell, A.P. Magyar, I. Aharonovich, A. Bleszynski Jayich, D. Awschalom, E.L. Hu, Deterministic coupling of delta-doped nitrogen vacancy centres to a nanobeam photonic crystal cavity, *Applied Physics Letters*, **105**, 261101 (2014).
- [51] S. Cui, A.S. Greenspon, K. Ohno, B.A. Myers, A.C.B. Jayich, D.D. Awschalom, E.L. Hu, Reduced Plasma-Induced Damage to Near-Surface Nitrogen-Vacancy Centres in Diamond, *Nano Letters*, **15**, 2887 (2015).
- [52] C.L. Lee, E. Gu, M.D. Dawson, I. Friel, G.A. Scarsbrook, Etching and micro-optics fabrication in diamond using chlorine-based inductively-coupled plasma, *Diamond and Related Materials*, **17**, 1292 (2008).
- [53] RP photonics encyclopedia:<https://www.rp-photonics.com/etalons.html>
- [54] A. Khalid, K. Chung, R. Rajasekharan, D.W.M. Lau, T.J. Karle, B.C. Gibson, S. Tomljenovic-Hanic, Lifetime Reduction and Enhanced Emission of Single Photon Color Centres in Nanodiamond via Surrounding Refractive Index Modification, *Scientific Reports*, **5**, 11179 (2015).
- [55] C. Kurtsiefer, S. Mayer, P. Zarda, H. Weinfurter, Stable Solid-State Source of Single Photons, *Physical Review Letters*, **85**, 290 (2000).

Chapter 6 Summary and future work

6.1 Summary

This thesis presents a detailed study on fabrication, characterisation and applications of novel diamond photonic structures and devices. By using the optimised fabrication techniques, diamond micro-lenses with radii of curvature larger than 13 mm and diamond membranes with a thickness less than 250 nm have been developed. The profiles, optical focal length and surface roughness of these diamond micro/nano-structures have been fully characterised using Surface profilometer, a knife-edge technique and AFM, respectively. Based on these diamond micro/nano-structures and components, monolithic diamond Raman lasers and Fabry-Perot cavity-coupled NV emission have been achieved.

In Chapter 1 of this thesis, the general background of diamond, which includes the diamond structure, type, synthesis, property and the diamond processing methods is introduced. At the end of this chapter, a brief overview of recent progress on diamond photonic devices including diamond optics, diamond Raman lasers and cavity-coupled diamond quantum light sources has been presented.

Chapter 2 introduced the basic techniques used to develop diamond micro/nano structures and photonic devices. The main fabrication techniques include the photolithography to define the PR mask patterns on surfaces of the diamond samples and the RIE/ICP dry etching to transfer the PR mask patterns to the diamond to achieve the diamond micro/nano-structures. The methods for characterising these diamond structures and photonic devices are introduced in the second part of this chapter, which includes the surface profilometer, the optical profiler, the AFM for the profile and surface characterisations and the knife-edge technique and the scanning confocal microscope for the optical characterisations.

The previously unclear PR reflow mechanisms and the PR shape evolution have been investigated in detail in Chapter 3. The “edge bulge effect” exhibited during the PR pattern reflow process has been observed and studied. The findings were then applied to develop controllable 3D PR structures on the silicon and the

diamond, especially to control the PR lens formation on the diamond surface. With such high controllability, PR hemi-toroid structures and micro-lenses with a diameter of 400 μm and a state-of-the-art ROC of 1.4 mm were achieved and these structures were also transferred successfully to the substrates such as diamond.

Chapter 4 reported the design and development of a novel concept of micro-lensed monolithic diamond Raman lasers based on the diamond lens fabrication and optimization. Combined with the PR pattern transfer via optimised Ar/Cl₂ ICP etching, the diamond micro-lenses with a large ROC have been achieved. These diamond micro-lenses presented a state-of-the-art large ROC (>13 mm) and sub-nanometre surface roughness which are critical for the performances of diamond Raman lasers. By applying these diamond micro-lenses fabricated on one surface of a 2 mm thick bulk diamond and coated with selective dielectric mirrors, the micro-lensed monolithic diamond Raman lasers have been demonstrated for the first time.

The development of state-of-the-art large size, single crystal ultrathin diamond membrane is presented in Chapter 5. The achieved diamond membrane has a diameter larger than 3 mm and a thickness less than 250 nm. By bonding this free-standing ultrathin diamond membrane on a high reflection DBR mirror and assembling them with a curved mirror, an open optical Fabry-Perot cavity was formed which enabled the modified NV emission from the diamond membrane. With considerable flexibility and tunability, this novel approach has great potential for achieving cavity enhanced ZPL emission of the NV in the diamond membrane and can be applied to realise scalable construction the QIP network based on single NV centres in diamond membranes.

6.2 Future work

Diamonds are a great platform for novel research and applications in frontiers of both fundamental physics and cutting-edge technology nowadays. With the advance of the diamond synthesis, researches based on this great material have attracted a broader interest in photonics and other areas such as electronics and mechanics etc.

The fabrication techniques developed in this thesis work are capable to make diamond micro/nano-structures with controllable shape and dimensions. Based on these techniques, new diamond devices such as diamond micro-toroids, diamond

aspherical lenses, concave or dual-focal lenses can be realised. These new diamond devices will underpin various applications. For example, with a high Q and a low volume, the diamond micro-toroid can be applied to the nanoparticle detection in a harsh environment or in water [1].

Monolithic diamond Raman laser with output wavelength at the infrared range can be developed using alternative coatings [2]. The infrared wavelength can be used for communication etc. Moreover, diamond Raman ring or disk resonators can be achieved using the techniques developed in this thesis work, which can be used as on-chip optical sources [3].

In addition, if combined diamond structure fabrication with other techniques such as transfer printing [4], assembling of integrated diamond photonic devices, e.g. diamond circuits and diamond waveguides, on a fully diamond based platform is possible [5].

The ultrathin diamond membrane developed in this work is a great platform for many important applications including the ultrathin X-Ray windows, radiation detection for heavy ions [6] and enhanced NV emissions in both monolithic diamond cavities [7] and in hybrid systems [8]. The scalable construction of networked QIP and quantum computation can benefit from the development of the large size freestanding high-quality single crystal diamond membranes. Cavity-coupled NV centres from the diamond membrane can be individual nodes for the networked QIP.

Additionally, the diamond membrane hosting NV centres beneath the surface are desired for many other novel applications in areas such as the bio-imaging, neuron-science, quantum imaging, quantum metrology and magnetometry.

It is expected that the techniques developed in this thesis work will pave the way to realizing the new diamond devices and applications.

6.3 Final remark

Diamond photonics is a broad research topic, currently undergoing explosive development on many fronts. Throughout this PhD study and thesis writing, I have been constantly amazed by the progress of diamond based photonics in diamond optics, lasers and the advanced quantum photonics. It is my

fortune and pleasure to witness such rapid development in this area and I am excited to be able to contribute to this development for the future technology.

Reference

- [1] A.M. Armani, K.J. Vahala, Heavy water detection using ultra-high-Q microcavities, *Optics Letters*, **31**, 1896 (2006).
- [2] S. Reilly, V.G. Savitski, H. Liu, E. Gu, M.D. Dawson, A.J. Kemp, Monolithic diamond Raman laser, *Optics Letters*, **40**, 930 (2015).
- [3] P. Latawiec, V. Venkataraman, M.J. Burek, B.J.M. Hausmann, I. Bulu, M. Lončar, On-chip diamond Raman laser, *Optica*, **2**, 924 (2015).
- [4] A.J. Trindade, B. Guilhabert, D. Massoubre, D. Zhu, N. Laurand, E. Gu, I.M. Watson, C.J. Humphreys, M.D. Dawson, Nanoscale-accuracy transfer printing of ultra-thin AlInGaN light-emitting diodes onto mechanically flexible substrates, *Applied Physics Letters*, **103**, 253302 (2013).
- [5] T. Schröder, S.L. Mouradian, J. Zheng, M.E. Trusheim, M. Walsh, E.H. Chen, L. Li, I. Bayn, D. Englund, Quantum nanophotonics in diamond [Invited], *Journal of the Optical Society of America B*, **33**, B65 (2016).
- [6] B. Dischler, C. Wild, *Low-Pressure Synthetic Diamond: Manufacturing and Applications*, Springer Berlin Heidelberg, (2013).
- [7] L. Li, T. Schröder, E.H. Chen, M. Walsh, I. Bayn, J. Goldstein, O. Gaathon, M.E. Trusheim, M. Lu, J. Mower, M. Cotlet, M.L. Markham, D.J. Twitchen, D. Englund, Coherent spin control of a nanocavity-enhanced qubit in diamond, *Nature Communications*, **6**, 1 (2015).
- [8] P. Rath, O. Kahl, S. Ferrari, F. Sproll, G. Lewes-Malandrakis, D. Brink, K. Ilin, M. Siegel, C. Nebel, W. Pernice, Superconducting single-photon detectors integrated with diamond nanophotonic circuits, *Light: Science & Applications*, **4**, e338 (2015).

Appendix I: Table of diamond sample specifications

Diamond sample used in chapters	Sample specifications
Chapter 3	Single crystal diamond, type II Ia-optical, Low absorption; Diameter: 4.0×4.0±0.1mm; Thickness: 1.0 ± 0.05mm; Orientation: [110] Top and bottom plane, [100] side faces; Flatness: <0.1 Roughness: < 5 nm Ra, measured on 1 mm; Birefringence: < 1.10 ⁻⁶ ; Absorption coefficient: 0.005 cm ⁻¹
Chapter 4	Single crystal diamond, type II Ia-optical, Low absorption; Diameter: 4.0×4.0±0.1mm; Thickness: 2.0 ± 0.05mm; Orientation: [110] Top and bottom plane, [100] side faces; Flatness: <0.1 Roughness: < 5 nm Ra, measured on 1 mm; Birefringence: < 1.10 ⁻⁶ ; Absorption coefficient: 0.005 cm ⁻¹
Chapter 5	Electronic grade single crystal membrane; Diameter: Φ= 3 mm; Thickness: 30 μm; [001] orientation

Appendix II: Publication list

Journal

- (1) **H. Liu**, S. Reilly, J. Herrnsdorf, E. Xie, V. G Savitski, A. J. Kemp, E. Gu, M. D. Dawson, "[*Large radius of curvature micro-lenses on single crystal diamond for application in monolithic diamond Raman lasers*](#)," Diamond and Related Materials, 65: 37-41, 2016.
- (2) **H. Liu**, J. Herrnsdorf, E. Gu, M. D. Dawson, "[*Control of edge bulge evolution during photoresist reflow and its application to diamond micro-lens fabrication*](#)," Journal of Vacuum Science and Technology B, 34(2): 021602, 2016
- (3) S. Reilly, V. G. Savitski, **H. Liu**, E. Gu, M. D. Dawson, A. J. Kemp, "[*Monolithic Diamond Raman Laser*](#)," Optics Letters, 40(6): 930-933, 2015.
- (4) **H. Liu**, E. Gu, M. D. Dawson, "*Ultrathin freestanding large-sized single crystal diamond membrane*" (Drafted)

Conference

- (1) S. Reilly, V. Savitski, **H. Liu**, S. Reid, D. Gibson, H. Dhillon, S.O. Robbie, E. Gu, M. D. Dawson, A. Bennett, A. Kemp, "Laser Induced Damage Threshold of CVD-Grown Single Crystal Diamond Surfaces with Various Surface Finishes," Advanced Solid State Lasers, 2015.
- (2) **H. Liu**, S. Reilly, E. Xie, J. Herrnsdorf, A. J. Kemp, E. Gu, M. D. Dawson, "Large radius of curvature micro-lenses on single crystal diamond and their application in monolithic diamond Raman lasers," International Conference on Diamond and Carbon Materials, Bad Homburg, 2015. (**Young Scholar Gold Award**)
- (3) S. Reilly, V. G Savitski, **H. Liu**, E. Gu, M. D. Dawson, and A. J. Kemp, "Monolithic diamond Raman lasers," De Beers Diamond Conference, Warwick, 2015.
- (4) S. Reilly, V. G. Savitski, **H. Liu**, S. Reid, D. Gibson, H. Dhillon, S. Olsson Robbie, E. Gu, M. D. Dawson, A. Bennett, and A. J. Kemp, "Laser Induced Damage of Diamond with Different Surface Finishes," De Beers Diamond Conference, Warwick, 2015.

- (5) S. Reilly, V. G. Savitski, **H. Liu**, E. Gu, M. D. Dawson, and A. J. Kemp, “Monolithic Diamond Raman Laser Operating at 573nm Utilising Microlens Structures to Form a Stable Resonator,” CA-1.3 (853), Conference on Lasers and Electro-Optics, Europe, Munich, 2015.
- (6) **H. Liu**, S. Reilly, E. Xie, A. J. Kemp, E. Gu, M. D. Dawson, “Large radius of curvature micro-lenses on single crystal diamond and their application in monolithic diamond Raman lasers,” presented at Semiconductor and Integrated OptoElectronics, Cardiff, 2015
- (7) E. Gu, **H. Liu**, J. E. Hastie, A. J. Kemp, and M. D. Dawson, “ICP-etched diamond microstructures for photonics and lasers (Invited)”, 8994-18, presented at Photonics West, San Francisco, 2014.